# Development of a Hot Gas Formable AA7XXX Alloy & Hybrid SPF/Warm Forming Technology for Light-Weight Automotive Structures in Niche Vehicle Manufacturing

**by**

**Scott Taylor**

Innovation Report

September 2016

This work is submitted in partial fulfilment of the requirements for the degree of Doctor of Engineering (International)

**Abstract**

This work looked to develop a new hybrid superplastic forming process in combination with a high strength aluminium alloy. A combination of physical testing, elevated temperature tensile testing, cone gas bulge and custom designed tool gas bulge tests were used to assess material formabilities to define the optimum forming conditions and establish an industrially suitable forming process. Testing established the suitability of a forming cycle within the industrial five minute target time, with the alloys undergoing recrystallization during preheat stages, forming at higher than typical strain rates and achieving full solutionization during the forming cycle. A two stage aging treatment (90°C for 8 hours and 130°C for 18 hours) achieved a high strength T5 temper meeting the industrial target of 300 MPa.

AA7020 alloy was capable of achieving strains in excess of 400% in the 5 minute forming cycle under optimal forming conditions provided the alloy had experienced a minimum 100% strain before contact with male tooling. After aging treatment the alloy was seen to achieve a yield strength of 305 MPa, slightly in excess of the industrial target.

A 1.6wt% nickel addition to AA7020 labelled alloy V3C initially showed increased performance in terms of formability and strength. The scale up of this alloy in the form V3CN showed decreased performance when compared to the V3C but was capable of strains in the region of 120% in the five minute forming cycle, a significant reduction compared to AA7020 but with no minimum strain requirement before contact with male radii. After aging treatment the alloy achieved a yield strength of 342 MPa, suggesting use as a higher strength alternative to AA7020 in applications with less extreme geometries.

## Declaration

This innovation report is submitted to the University of Warwick in support of my application for the degree of Engineering Doctorate. It has been composed by myself and has not been submitted in any previous application for any degree. The work presented (including data generated and data analysis) was carried out by the author.

## Engineering Doctorate Mentors

Academic Mentors: Professor Richard Dashwood, Dr Vit Janik

Industrial Mentor: Dave Edwards

**Acknowledgements**

I would like to give special thanks to Professor Roger Grimes, whose help has been invaluable during these past four years and who can now enjoy some well-deserved peace and quiet having so kindly delayed this until the completion of this project.

I would like to express my deepest thanks to my supervisors Professor Richard Dashwood and Dr. Vit Janik for their guidance and the trips abroad throughout this project, I would also like to thank my mentors at Superform Dave Edwards and Andy Hares as well as the rest of the staff there who helped on this project. I would like to thank the EPSRC, Warwick University and Superform for kindly funding this doctorate.

I'd like to thank my fellow students, Craig Carnegie, Elspeth Keating, Hamzah Alharthi, Sanjeev Sharma, Richard Beaumont, Neill Raath and Mario Carandente for basically being in the same place at the same time and also thanks to the rest of the Materials and

Manufacturing Group and the workshop staff.

Thanks to my parents and friends who have put up with my complaining throughout these past four years, especially the guys at the climbing wall who have helped me keep my sanity more than they know.

## Table of Contents

**Glossary of Terms**

BSE – Back Scattered Electron

EBSD – Electron Back Scattered Diffraction

EDS – Energy Dispersive Spectroscopy

EDX – Energy Dispersive X-ray Spectroscopy

EngD – Engineering Doctorate

FSD – Forward Scatter Detector

PSN – Particle Stimulated Nucleation

QPF – Quick Plastic Forming

RE – Rare Earth

SE – Secondary Electron

SEM – Scanning Electron Microscope

SPF – Super Plastic Forming

SUSA – Superform USA

WMG – Formally Warwick Manufacturing Group, where the Engineering Doctorate was based.

## List of Figures

## List of Tables

# 1. Introduction

## *1.1. Project Introduction*

This Engineering Doctorate (EngD) was sponsored by Superform Aluminium, part of the Luxfer group of companies. Superform specialises in Superplastic (SPF), Quick Plastic (QPF) and Warm forming of light alloys (aluminium, magnesium and titanium) with operations in the UK (Worcester) and USA (Riverside, California). The aim of this EngD was to increase the knowledge base of current superplastic forming processes and materials and to evaluate in which direction the field is moving. With this knowledge the goal was to develop a modified forming process and complementary aluminium alloy which would allow Superform to maintain a technological edge over their competitors and open up new avenues of business.

Due to the added flexibility within an EngD the focus of the research within this project shifted throughout, driven by the real world industrial needs of the sponsor company. Initially the project was intended to be focussed on the use of magnesium sheet within niche vehicle manufacturing. Due to the lower modulus of magnesium compared to aluminium the material was deemed unsuitable for the applications Superform looked to target within this project as part geometries would be too large, as such the research focus shifted to aluminium in particular 7000 series alloys.

An industrial requirement of 300 MPa in service yield strength was established, below this 6000 series alloys would be deemed acceptable. AA7475 is a commonly used superplastic alloy, but its requirement for low strain rates, leading to long forming cycles in combination with its high price make it unsuitable for most automotive applications. As such AA7020 was identified as a possible alternative due to its lower cost, solutionization temperature around that of an SPF forming process and its negligible

quench rate sensitive coupled with its T5 yield strength achievable with a relatively low temperature post forming heat treatment. Alongside the assessment of AA7020 as a suitable alloy, additions of various alloying elements were investigated to see if the formability and post forming properties of the alloy could be improved.

This aim was achieved strategically through the submissions of the EngD portfolio. Firstly an extensive literature review around vehicle light weighting and the driving forces behind new technologies for vehicle emissions reduction was conducted. The findings from this review were then used to guide further submissions which focussed on studies of the formability and post forming properties of several AA7000 series alloys, the work in each submission guiding later testing to help develop a process and alloy that could meet the formability requirements of customers as well as a strength target of 300 MPa yield strength. Work was conducted at WMG as well as on a more industrial scale at Superform UK, and Superform USA (SUSA) and also in conjunction with Hydro Aluminium who supplied all of the materials within the project as well as helping with alloy development throughout.

### *1.2. EngD Introduction*

The EngD Int. is a research degree with added taught modules and an international industrial placement that is portfolio based. The purpose of the EngD is to innovate on an industrial scale based around current industrial issues, and to "develop engineers who are capable of demonstrating innovation in the application of knowledge to the global engineering business". The doctorate develops a wide range of competencies which are demonstrated within the various portfolio submissions, the personal profile and various

taught modules, finally the innovation report ties together all of the submissions and presents the “story” of the doctorate and development throughout the programme.

This doctorate comprises of the innovation report, a series of six portfolio submissions alongside a personal profile and six taught MSc modules; the submissions being as follows:

1) Vehicle lightweighing an Overview – A literature review around the subject and driving forces behind emission reductions and vehicle lightweighting technologies.

2) Formability Study of AA7020 and Various Alloys with Modified Chemistries Thereof – A technical report on the formability of various aluminium alloys.

3) Advanced Formability and Microstructural Study of AA7020 and a Nickel Containing Variant – A technical report continuing work from the first submission, focussing on the best performing alloys.

4) Comparison of Material Properties and Performance of a Nickel Containing AA7020 Alloy After Production Scale Up – A technical report detailing work carried out comparing the performance of the previously best performing “lab scale” alloy after production had been scaled up.

5) EngD International Placement Report – A report and diary on the work carried out at SUSA as part of the international placement.

6) Papers & Presentations – A collection of papers and slides from presentations given at international conferences during the project.

Taught modules were taken in six subjects: Lean principles, Technology management, Advanced materials and processes, Financial analysis and control systems, Legal aspects

of a global business, International joint ventures. Full details of these modules are given within the personal profile alongside details of the competencies demonstrated during the Doctorate. The innovation report focusses on the technical aspects of the doctorate only.

### *1.3. Contribution to Innovation*

Unlike a traditional PhD which aims to achieve a contribution to knowledge, the EngD aims to achieve a contribution to innovation. Within this project that innovation lies in the adaptation of a low-cost commercial alloy without expensive SPF-specific thermomechanical processing used in combination with a modified SPF forming process to offer a new option for automotive manufacturers looking for vehicle light weighting opportunities. Contrary to conventional SPF forming processes, which involve long cycle times, forming at elevated temperatures and low strain rates, this project innovated the SPF process by introducing a modified AA7020 alloy that allows forming at higher strains resulting in significantly reduced cycle time.

To achieve and understand the underlying mechanisms of microstructural evolution during the SPF process physical testing of various modified AA7020 alloys using different techniques such as elevated temperature tensile testing, gas bulge testing and also industrial scale SPF testing were employed. This physical characterisation was used to identify the optimal forming conditions to achieve industrially useful formability (circa 150% linear elongation) and to meet a 300 MPa yield strength requirement.

Advanced microscopy techniques including in-situ fore-scattered detection (FSD) which gives information regarding sample topography and electron back scattered diffraction (EBSD) which encompasses phase analysis, grain size and grain orientation, were used to establish the microstructural evolution of the materials during various stages of the

forming cycle. The results from these tests were used to inform the industrial process and modify current SPF forming cycles to establish a forming cycle suitable for the material.

The industrial goals for this project were to deliver a material and process that could achieve an in service yield strength of 300 MPa with a forming cycle time of five minutes. A secondary requirement from Superform was that this yield strength was achieved without the use of any high temperature post forming processes (such as solution heat treatment) which can cause distortion within parts which have been formed to fine tolerances. The use of in situ SEM/EBSD techniques were employed to help understand the processes at work which allowed for a more robust forming process to be developed with better understanding of the underlying mechanisms responsible.

The outcome from this work has been a modified SPF process which uses pre-deformation by means of hot stamping followed by gas pressure forming at strain rates higher than a typical SPF process. High strain rate forming used in combination with a commercially cold rolled AA7020 alloy (not specially processed for SPF) delivers a material capable of forming parts in a five minute cycle and with a final strength greater than 300 MPa yield, without the need for a high temperature post forming heat treatment. The development of a modified alloy designated V3CN based on AA7020 with a 1.6wt% addition of nickel offered an alternative to the AA7020 in applications where higher strength is required and lower levels of formability are acceptable. The material and process have also achieved commercial success, the material having passed through the prototyping and testing phases and parts scheduled to go into production in January 2017 for use within door crash structures of a high end niche vehicle manufacturer.

### *1.4. Thesis Structure*

This thesis brings together work conducted throughout the various portfolio submissions, Chapter 1 provides an introduction to the project and the EngD, Chapter 2 then gives an overview of background and literature review conducted throughout the project. Experimental work carried out across all submissions is detailed in Chapter 3 with the relevant portfolio submission in the title, work is grouped together by testing, with individual methodology, results, discussion and conclusions for each. Chapters 4 and 5 then present an overall discussion of the whole project tying together the various experimental chapters, finally Chapter 6 gives suggestions for future work which have arisen from this research, and possible areas for industrialisation of both alloy and process.

## 2. Background/Literature Review (Submissions 1-6)

This doctoral research project was based around developing a hybrid SPF forming process and an aluminium alloy suitable for use within that process. The aims of the project were to reduce cycle times and to provide a formable high strength alloy, the main driving force behind these aims is vehicle lightweighting. The use of higher strength, lightweight alloys allows for less material to be used to bring down the overall weight of the vehicle whilst retaining strength levels in critical regions. This chapter details the reasons behind lightweighting and associated processes, as well as presenting a literature review around hybrid SPF processes and the use of novel alloys.

### *2.1. Automotive Lightweighting*

Vehicle lightweighting is an old principle which has been around since the inception of mass produced vehicles, Henry Ford, one of the pioneers of vehicle mass production stated *"Excess weight kills any self-propelled vehicle"* in 1923. Over time the motivation for weight reduction within the automotive industry has changed, initially it was to increase, or at least not inhibit performance, at this time relatively low powered engines could not cope with vehicles with any excess weight.

Whilst performance is still an important factor in vehicle design and lightweighting, the current main driving force for the industry is meeting stricter and more stringent emission regulations. To help reduce emissions and increase efficiency new innovative processes and materials are constantly being developed and put into production. During the late 1970s and early 1980s there was a radical change within automotive technologies that led to a swift significant reduction in vehicle curb weights [1].

The main changes during this time were in the move from rear wheel drive to front wheel drive which in combination with a move from larger eight cylinder engines to smaller more efficient four or six cylinder engines led to a significant reduction in powertrain weights [2]. The other being the move from body on frame construction to a unibody construction where body and chassis components are manufactured together to produce an integrated load bearing structure [3].

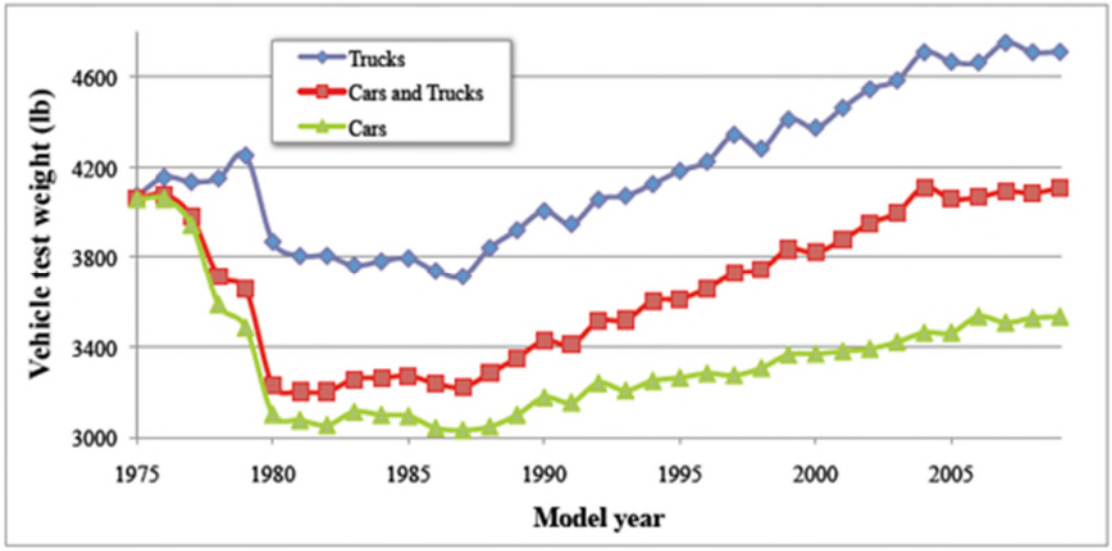


Fig.1. Trend of increasing average vehicle weights 1975-2005 [4].

Since this rapid drop in vehicle weights, there has been a steady year on year increase in average weights, this is firstly due to an increase in average vehicle sizes, with cars across all classes getting larger. Secondly there has been an increase in standard equipment within vehicles, items which were previously seen as optional extras such as climate control, built in sat-nav etc. are becoming more standard equipment, alongside increased safety features such as multiple airbags, which all increase vehicle weight [5]. The increase in weight due to “extras” is illustrated in fig.2 from a study by Zoepf on vehicle weight trends [6].

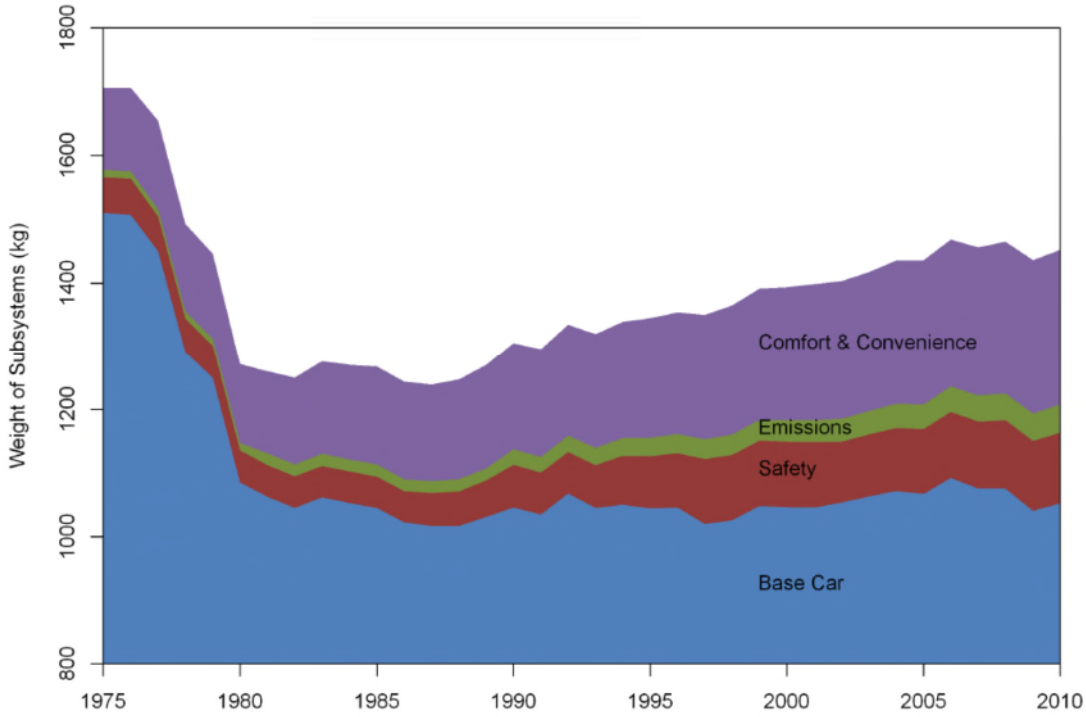


Fig.2. Breakdown of increase in vehicle weights 1975-2010 [6].

Whilst there has been a constant increase in vehicle weight there has also been an increase in efficiency, which shows that whilst weight has increased, average fuel consumption has also decreased [1]. To meet new emissions targets motor companies have invested heavily in designing and producing more efficient engines and drivetrains, engines such as the new Ford Ecoboost range which utilise turbochargers and direct fuel injection to achieve very high performance and economy from small displacement engines [7]. Alongside increasing efficiency of current well established technologies, the use of alternative fuels such as hydrogen (generated via fuel cells), electric vehicles and hybrids have all received significant attention with cars such as the all-electric Nissan Leaf becoming a more common sight [8]. The use of hybridisation and electrics motors has also started to move into the more exotic niche vehicles with cars such as the BMW i8, McLaren P1 and Porsche 918 Spyder using hybrid internal combustion engines and electric motors [9-10].

### *2.1.1. Legislation*

Ever increasing evidence of the harmful effects of greenhouse gas emissions (GHG) and the resultant impact on the environment have led to the implementation and adoption of ever more stringent regulations on the levels of emissions allowed from vehicles. There have been global agreements on emissions reduction from all sectors, such as the Kyoto agreement, with an overall agreement and target for reductions but with all signatories producing their own regulations to achieve this. Looking at the G20 nations, where 90.8% of all vehicle sales worldwide take place most countries have their own legislation, or revert to using EURO standards which are in place across all European member states, the reduction targets for these standards are shown in fig.3.

Japan has the most stringent legislation (followed by European standards), whose “Top runner” energy efficiency plan was first introduced in 1999. This programme has been superseded several times due to the fact that by 2002 the vast majority of vehicles had already reached 2010 emission standards [11]. European regulations came into place in the mid-90s and were initially voluntary; designed to achieve a 90% reduction in $CO_2$ emissions by 2008, trends in 2006 showed that this would not be achieved and new compulsory regulation was introduced [12]. European regulations have been through several revisions and are now at Euro 6 which was implemented in 2014, earlier “Euro” standards are being adopted worldwide [13].

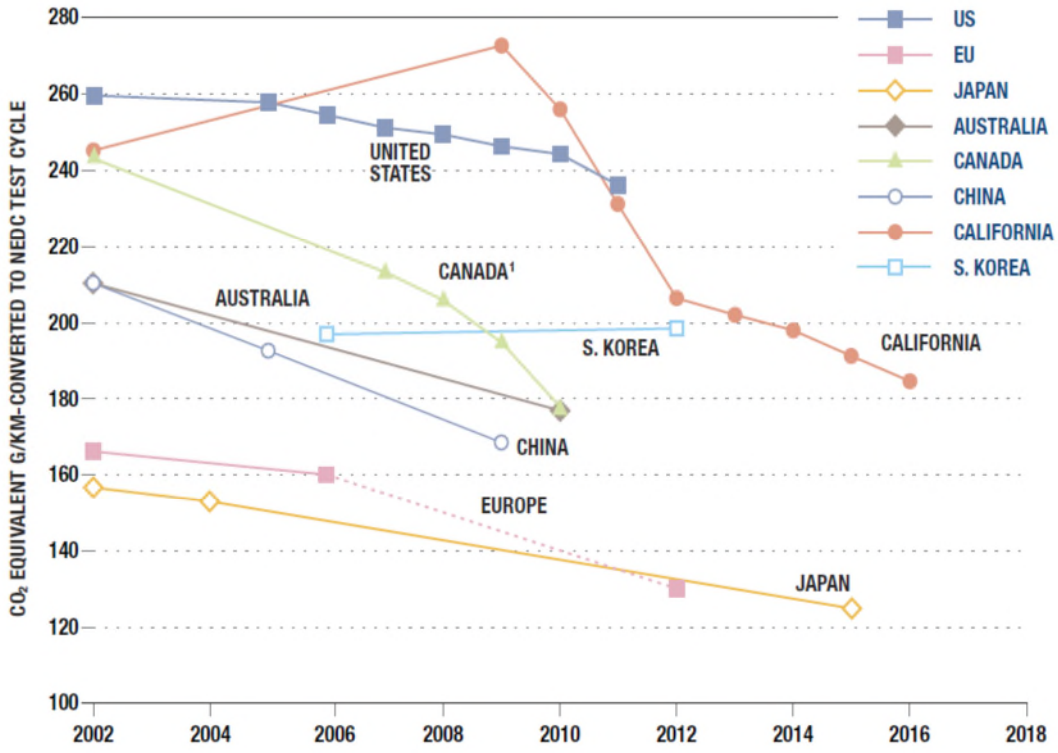


Fig.3. Actual and projected GHG emissions for new passenger vehicles by country 2002-2018 [12].

American regulations are governed by the US CAFE (Corporate Average Fuel Economy) regulations which first came into place in 1975 as a response to the oil crisis at the time. These are some of the least stringent regulations of any of the G20 nations and are focussed on increasing efficiency of vehicles over a manufacturer's whole range [14]. Californian regulations are separate to CAFE and target reduction of vehicle emissions individually rather than over a whole range, the standards have increased in stringency annually aimed at a 30% GHG emission reduction by 2016. Since their introduction in California a further 11 states have adopted the Californian regulations [15]. Further details on these regulations alongside those elsewhere in the world are expanded in Portfolio Submission one.

### *2.1.2. Materials for Lightweighting*

As mentioned earlier, there was a shift in vehicle architecture moving to unibody construction, this has helped to reduce weight. With traditional materials however there is a limit to the possible weight reduction. As such vehicle manufacturers have looked at various materials in order to aid lightweighting. The obvious requirements being increased strength for the same density, the same strength but with decreased density or ideally increased strength with decreased density.

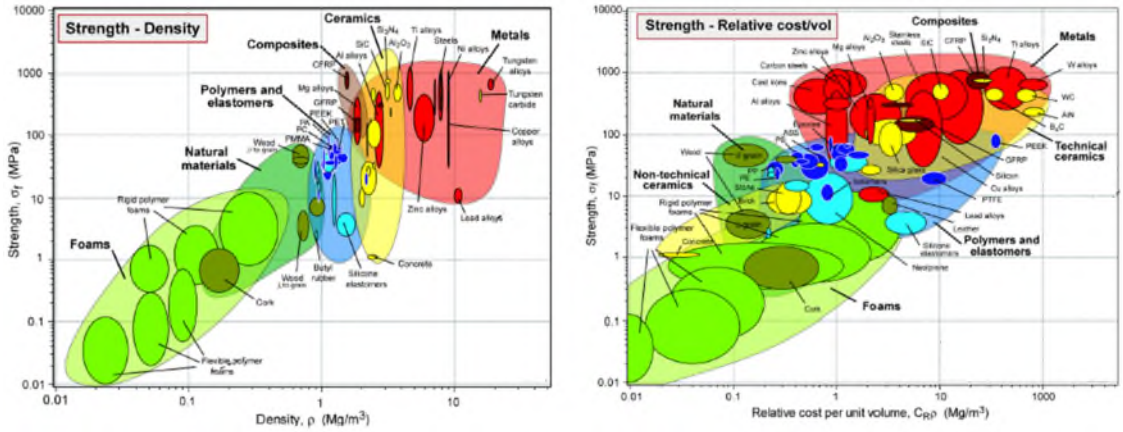


Fig.4. Strength vs density & strength vs cost for various engineering materials [16].

Titanium alloys offer the ideal properties for the automotive industry with high strength and low density illustrated in fig.4, however currently the costs associated with titanium make it economically unviable within the automotive industry [17]. Magnesium is another light metal with a density less than a quarter of steel, it has limited applications within the automotive industry due to several factors. Although Mg has very poor corrosion and oxidation resistance, it has been adopted in limited and typically higher performance applications such as engine blocks and transmission housings where significant weight reductions are possible in comparison to cast iron blocks [18]. Magnesium also suffers from low room temperature formability and as such needs to be formed at elevated temperatures in sheet form by processes such as superplastic forming.

Mg in sheet form is starting to see limited use in high end vehicles such as the Porsche GT3 RS whose roof was formed in POSCO magnesium alloy [19] however its adoption to higher volume manufacture is unlikely at present.

Steels have traditionally been the primary material used for vehicle construction. This is still true today, with significant advances in steel technology allowing vehicle lightweighting through techniques such as down gauging or tailored blanks. The adoption of AHSS (advanced high strength steels) and UHSS (ultra-high strength steels) steels which have a much higher strength to weight ratio have helped to reduce vehicle weights [20]. The increased strength of these steels means that for a specific application less material will be required for the same strength than with low carbon steels. A good example of the use of high strength steels was the BMW 7 series which achieved a 35% weight reduction in structural components compared to regular steels [21].

Composites offer an extremely high strength to weight ratio and as such are of great interest to the automotive industry. They can be split into two different groups, CRFP (carbon fibre reinforced polymer) and GRFP (glass fibre reinforced polymer). GRFP products are typically cheaper, using fibreglass sheets layered with epoxy resin they are used extensively in the kit and replica car market where a GFRP body shell can be used to substitute an expensive original part and reduce the overall weight of the vehicle, the disadvantage being brittle failures in crash situations; however, repairs are cheaper than with metals.

CRFP products have been widely used within racing teams and high end automotive manufacturers such as Ferrari Lamborghini and McLaren. The high sales price of these vehicles offsets the expense of the CRFP materials, an example being the Ferrari Enzo which cost $659,330 in 2002 [22]. CRFP panels are manufactured in the same manner

as GRFP, generally being hand laid and as such are used in more niche vehicles. The move towards a more industrial process resin transfer moulding (RTM) in place of hand laying means that CRFP production can be significantly scaled up. BMW are the first vehicle manufacturer to use CRFP produced using RTM in mass produced vehicles in its i3 model [23], to manufacture panels from recovered carbon fibres in collaboration with Boeing [24]. This helped to significantly reduce material costs making CRFP a much more attractive option for use within more mass production.

Aluminium alloys currently offer one of the best options for vehicle lightweighting, having good formability (especially at elevated temperatures) high strength to weight ratios, being relatively low cost and readily recyclable (dependent upon alloy and alloying elements) [25]. Aluminium has historically been used only within high end automotive applications due to its increased cost in comparison to steel, although advances in automotive aluminium sheet production leading to cost reductions are making aluminium a more viable material for use in more mass produced vehicles [26].

Aluminium alloys are becoming more widely used within the automotive industry for varied applications. The aluminium being used being dependent on the desired properties of the alloy, shown in fig.5. Typically 5XXX series alloys are used in body panel applications where aluminium sheet has been processed for increased formability and surface finish, whereas higher strength 6XXX or 7XXX series are used in extrusion applications where final strength is the most important factor [26]. As these alloys have limited formability at room temperature, more advanced elevated temperature forming processes such as SPF are required in combination with the alloys, the various alloys and processes are discussed in more detail in the next two sections of this report.

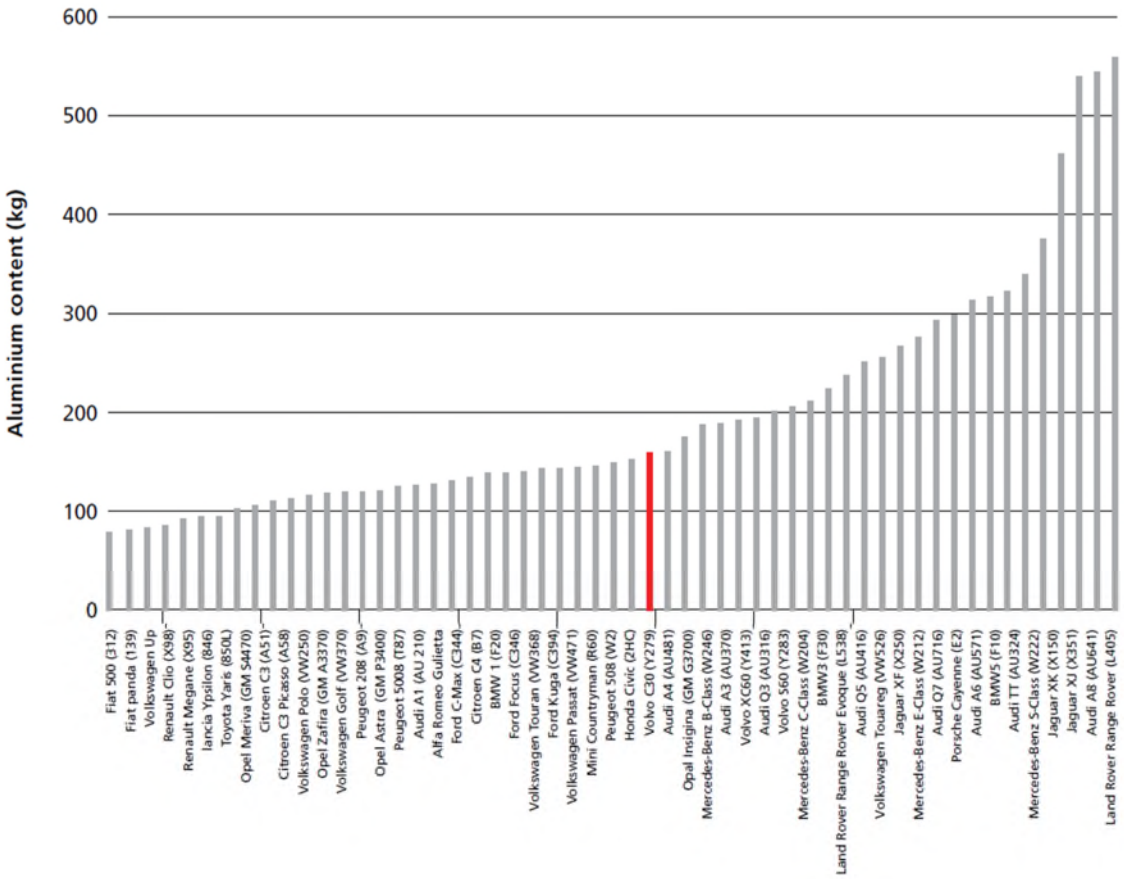


Fig.5. Aluminium content in various cars in the E.U. market in 2012 [25].

### *2.2. Aluminium Alloys*

Aluminium is the third most abundant element and the most abundant metallic element found on Earth; it is also the fourth lightest metal. It has a close packed face centred cubic structure, with atoms arranged in planes along which slip can occur easily during deformation allowing excellent formability exceeding all lighter metals (Li, Be, Mg) [27]. As a pure metal it has very limited applications due to its relatively low strength, it can however be alloyed with various elements to yield very high strength materials with relatively low densities which can be used in higher strength applications to rival materials such as steel and carbon fibre [28].

Wrought alloys of aluminium are grouped together by the major alloying element and given a four figure code number with the first digit designating the major alloying element

within the series, the second designates whether it is an original alloy “0” or any other digit indicates a modification to the alloy [29]. The Aluminium Association series designations are detailed in table 1.

Table.1. Wrought aluminium alloy series designations [29].

| Designation | Major Alloying Element | Age Hardenable |
|---|---|---|
| 1XXX | None Min 99% Aluminium | Not Age Hardenable |
| 2XXX | Copper | Age Hardenable |
| 3XXX | Manganese | Not Age Hardenable |
| 4XXX | Silicon | Age Hardenable if Mg Present |
| 5XXX | Magnesium | Not Age Hardenable |
| 6XXX | Magnesium & Silicon | Age Hardenable |
| 7XXX | Zinc | Age Hardenable |
| 8XXX | Miscellaneous | Some Age Hardenable |
| 9XXX | Experimental | - |

To improve the mechanical properties of aluminium there are many alloying elements added for varying purposes, such as increasing formability or to increase strength. A list of alloying elements commonly added to aluminium alloys and their uses are listed in table 2. This list is not exhaustive as other elements are found in aluminium alloys, however these are some of the most frequently used.

Table.2. Common alloying elements of Aluminium [29].

| Alloying Element | Purpose |
|---|---|
| Chromium | Added usually up to 0.35%, and is used to control grain structure, forms fine dispersed phases which inhibit grain growth and nucleation and prevent recrystallization during hot working and heat treatments |
| Copper | Increases strength and hardness, facilitates precipitation hardening but impacts negatively on ductility and also corrosion resistance. |
| Lithium | Increases strength and Young’s Modulus and decreases density. |

| | |
|---|---|
| Magnesium | Increases strength without negative impact on ductility or corrosion. Often alloyed in combination with Silicon or Manganese for greater strength. |
| Manganese | Increases strength either in solid solution or as a fine intermetallic phase. |
| Nickel | Improves strength and hardness but impacts upon ductility. Forms large secondary particles $Al_3Ni$ which lead to a rise in particle stimulated nucleation during forming. |
| Silicon | Reduces melting temperature and increases fluidity. When alloyed with Magnesium forms $Mg_2Si$ to make a heat treatable alloy. Silicon is the major addition to low grade aluminium cast alloys which make use of recycled aluminium. |
| Zinc | Increases strength, and allows for precipitation hardening. Commonly alloyed with Magnesium to form $MgZn_2$ particles. |
| Zirconium | Forms a fine intermetallic precipitate that inhibits recrystallization and plays a significant role in grain refinement of cast material. |

Further detailed discussions of the various aluminium alloy series alloying elements and applications are included in portfolio submissions one, two and three. The main series of interest for this research is the 7XXX series which is discussed further in section 2.3.3 of this report in relation to its uses within SPF processes.

## *2.3. Superplastic Forming*

### *2.3.1. Superplasticity*

Superplasticity is the ability of certain polycrystalline materials to undergo significant elongations well in excess of their plastic limit before failure under very specific conditions. The material should be processed to attain a fine equi-axed microstructure around 5-15μm before SPF such as AA5083, or capable of developing this grain structure during the early stages of the SPF process such as AA2004 [30]. A high concentration of high angle grain boundaries (lattice misorientation >15°) is considered important due to the mechanism of grain boundary sliding responsible for the large elongations observed

in superplastic materials [31]. Superplastic forming processes are then typified by forming at low strain rates $10^{-4}s^{-1}$ $10^{-2}s^{-1}$ and at elevated temperatures typically greater than 80% of the materials melting temperature [32].

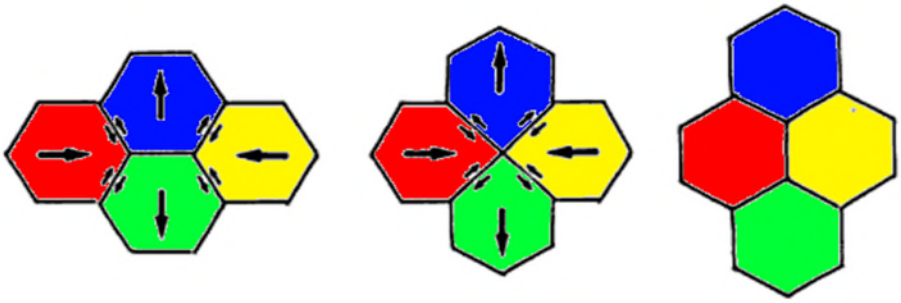

Fig.6. Neighbour switching event to accommodate grain boundary sliding [33].

Superplastic materials typically have a high strain rate sensitivity coefficient (m value) which describes a materials ability to resist necking during forming, a typical metal would have an m value 0.2≤ whereas a superplastic material would be ≥0.5 [32]. The m value is related to the flow stress of the material during deformation by the following equation;

$$\sigma = \frac{F}{A} = K\dot{\varepsilon}^{m}$$

where $\sigma$ is flow stress, $F$ is the applied force, $A$ is the cross-sectional area, $K$ is the material hardening constant, $\dot{\varepsilon}$. is the true strain rate and $m$ is the strain rate sensitivity coefficient [34].

Typically for a material to be considered superplastic extensions of at least 200-400% should be achievable within uniaxial tensile testing [35]. Extensions of over 8000% have been reported for an aluminium brass alloy [36] and extensions up to 2500% have been reported [37] within a heavily processed 1xxx series alloy with scandium additions. There is an academic shift championed by particular academics and universities to define superplasticity as a minimum of 400% linear elongation and an ‘m’ value greater than

0.5 [38]. The logic behind this is that as grain boundary sliding is the primary deformation mechanism in superplasticity the minimum ‘m’ value should be at the point where GBS is the dominant deformation mechanism, this being 0.5 [39]. This is suitable as an academic definition however has very little relevance within real world industrial forming where elongations of 400% would rarely if ever be designed or experienced within parts.

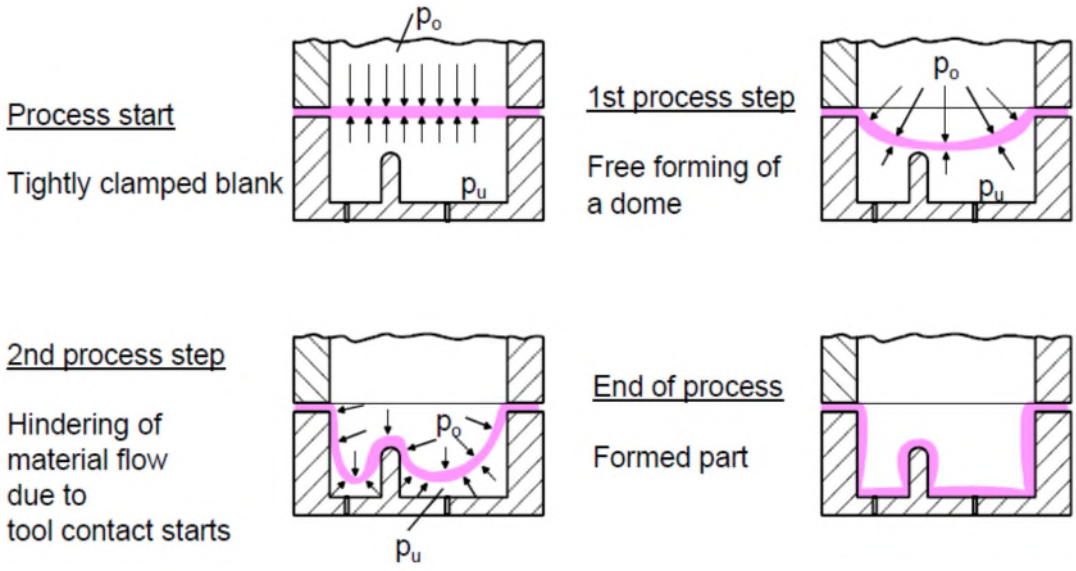


Fig.7. Schematic of a typical superplastic forming process [40].

A typical superplastic forming process is shown in Fig.7. Material is loaded into a tool where it is then clamped and preheated, gas pressure is then used to form the part, the clamping hindering any flow of material into the die. Cycle times of SPF processes are much higher than standard forming processes such as stamping due to the low strain rates used. Superplastic forming has the advantage of producing parts with no spring back, no residual stress and being a near net shape process [41]. Superplastic forming typically takes place using single sided dies, the lack of matched dies and the low stress experienced during means that tool life is much greater than in standard forming processes and lower value materials can be used to produce tools.

### *2.3.2. Mechanisms of Superplasticity*

There are many mechanisms responsible for materials superplasticity, grain boundary sliding as shown in fig.6 being the primary mechanism in a typical purely superplastic process. Typically the materials m value will dictate the mechanism by which the material deforms as can be seen in fig.8, plotting log stress vs. log strain rate, leads to a sigmoidal curve whose gradient will give the materials m value. The graph can be split into three different regions, firstly region I with materials exhibiting low m values ≈0.2 with and at low strain rates, diffusion creep is the controlling mechanism. Along with the low m value of the material the deformation will be typified by grain elongation during the process, with diffusion of the atoms and vacancies across the grains towards grain boundaries acting as a deformation rate controlling mechanism.

Region II or the superplastic region is where the materials m value is 0.5 or higher, this indicates deformation by means of grain boundary sliding. The prevalence of high angle grain boundaries which enable neighbour switching events to take place allows for the accommodation of external stresses on the grain boundaries. Groups of grains move relative to each other by means of sliding and prevent nucleation and coalescence of cavitation that would happen in the region with lower m value. Within grain boundary sliding, grains move over each other parallel to the grain boundary interface and controls the plastic flow of polycrystalline materials [39]. The way in which these mechanisms act leads to a final microstructure that shows minimal grain elongation, but a higher level of grain rotation.

Region III again is typified by lower m values ≈0.2, however strain rates in this region are significantly higher, and deformation is dominated by power law or dislocation creep rather than diffusion creep. This deformation is enabled by the glide of dislocations

through the crystal lattice structure and is indicated after forming by grain elongation which is also observed in diffusion creep but also by an increase in the microstructural texture. Cavitation usually occurs in Region III and depending on the strain rate is the dominant failure mechanism.

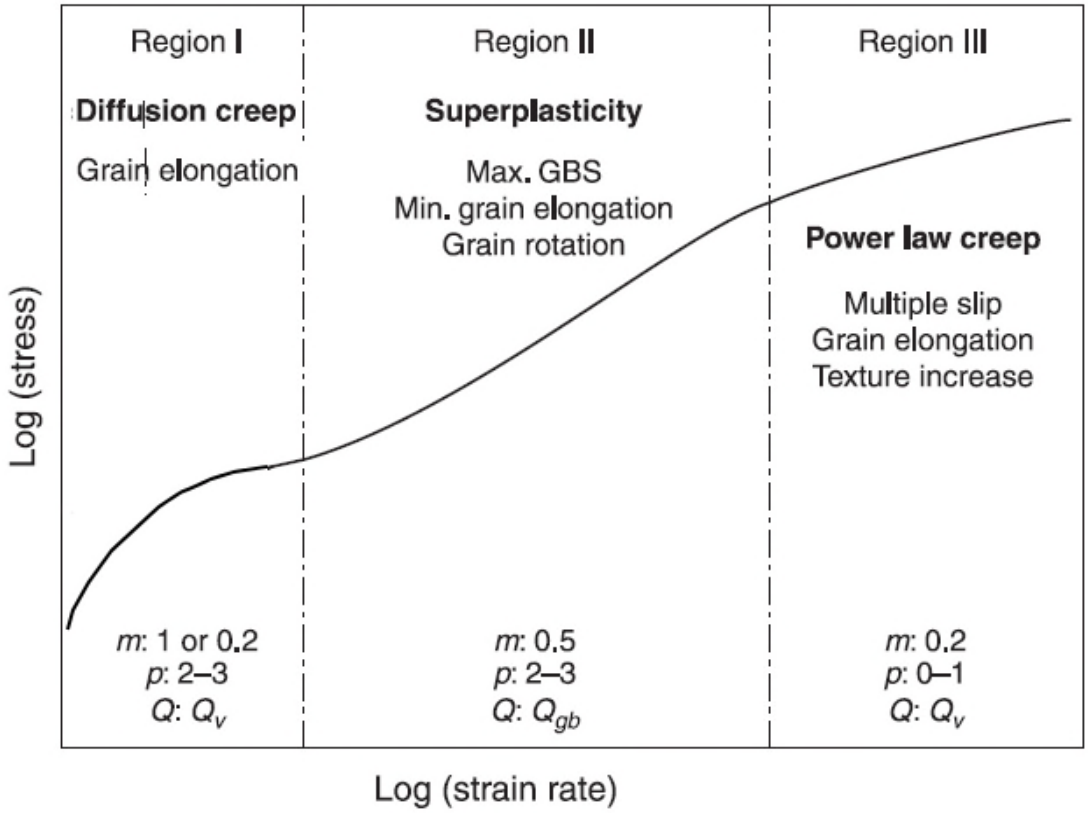


Fig.8. Log strain vs. log stress plot for a typical SPF alloy showing different regions and dominant deformation mechanism [30].

Whilst in pure super plastic forming grain boundary sliding is the primary deformation mechanism, the higher strain rates observed within the dislocation creep region are more typical of those within hybrid SPF forming processes. Hybrid SPF processes either use higher strain rates, or make use of a mechanical preforming step to reduce overall cycle times, with the dominant deformation being dislocation creep.

Dislocation creep is the movement of dislocations through the materials crystal lattice structure as shown in fig.9. which lead to plastic deformation and unlike grain boundary

sliding is independent of grain size which should mean the ability to use cheaper alloys which have not been processed for SPF forming. An increase in strain rate within the forming process will lead to an increase in the stresses experienced, this in turn leads to a shift from grain boundary sliding to dislocation creep as the primary deformation mechanism [42].

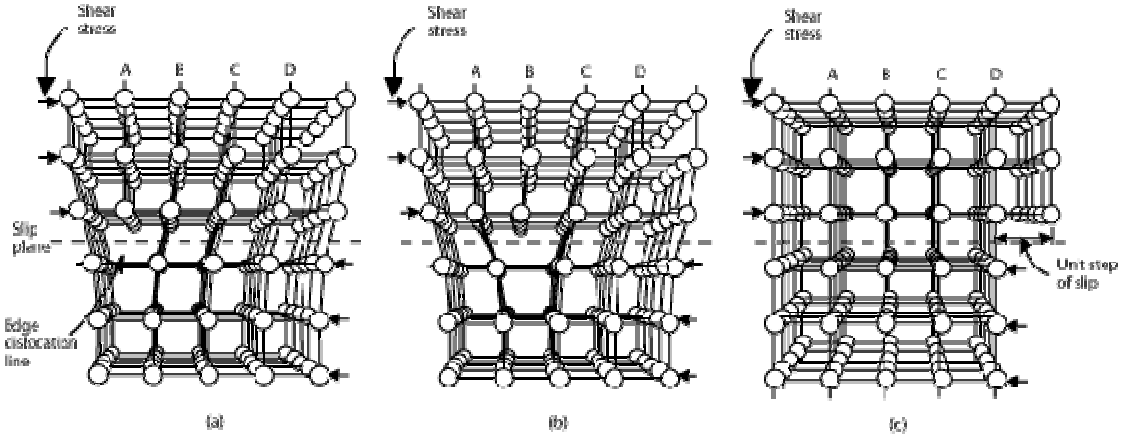

Fig.9. Dislocation movement through crystal lattice [33].

### *2.3.3. Materials for Superplastic Forming*

Materials for use within SPF processes are highly processed by rolling to achieve a fine equiaxed grain structure, this high level of processing leads to a higher cost in the material price but this is typically offset by the higher added value of parts formed. Current commercial alloys which are widely used are 2004, 6061, 7475 and 5083 with applications found typically within the automotive and aerospace fields [43].

Most of these alloys have a fine initial grain structure. AA2004 or Supral 100 initially developed in 1969 [44] was the first aluminium alloy to show high levels of superplasticity (1200% linear elongation) starting from a heavily cold worked, completely uncrystallised material. This alloy demonstrates some limited recovery and grain refinement during the preheating stages, but requires the application of strain to

allow for recrystallization to occur and achieve a finer grain structure. This occurs during the early stages of deformation where below 0.4 strain a fine structure with equiaxed grains of an average diameter of 0.5μm and high fraction of high angle grain boundaries evolves [45]. This dynamic recrystallization is the primary mechanism responsible for the alloys formability, which demonstrates that an initial fine grain structure is not necessarily required if grain refinement occurs during the deformation process, and indicates the possibility of the use of more coarse grained lower cost materials within a hybrid SPF forming process.

The elevated temperature of SPF processes is promising for the use of coarser grained alloys as during the preheating stage static recrystallization of the material can occur. Harmful grain growth that may occur in later stages of static recrystallization within aluminium alloys, this is controlled by Zener-Hollomon pinning of grains by means of finely dispersed intermetallic particles which is well documented [46]. Zirconium is added to aluminium alloys for this purpose, as well as chromium which inhibits grain growth [47]. Large secondary particles of sizes greater than 2μm can help to act as areas of particle stimulated nucleation during static recrystallization [48]. These large particles act as areas where there is a large concentration of stored energy during rolling, leading to large misorientations across short distances and fine sub grains. These in turn lead to large numbers of high angle grain boundaries via polygonization [49] as illustrated in fig.10.

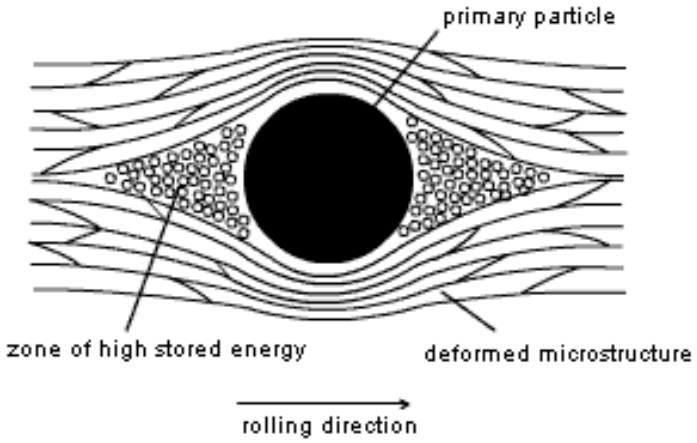

Fig.10. Illustration of particle stimulated nucleation site [49].

These high angle grain boundaries lead to a recrystallization nucleus which helps to aid the recrystallization of the material, these in turn lead to a more randomised finer grain structure [50]. Recent studies in Russia have shown that nickel additions to 7XXX series have led to significantly improved elongations and particularly fine grain structures after preheating due to PSN which has been driven by the presence of $Al_3Ni$ particles [51]. These nickel additions have led to elongations of over 660% under optimal forming conditions [52].

Nickel additions to 7XXX series alloys in previous studies were observed to increase the efficacy of static recrystallization by means of PSN [53]. The use of AA7020 within this report in combination with nickel was influenced by these studies with the aim being to increase rate of recrystallization through the presence of $Al_3Ni$ particles. Whilst no studies have been conducted on the SPF abilities of this alloy, studies on friction stir welding of it have shown dynamic recrystallization occurring in areas of welds [54].

Whilst not of interest industrially due to massive costs of rare earth (RE) containing master alloys, there is a large academic interest in the addition of RE elements to aluminium alloys to increase formability, scandium additions have been shown to achieve significantly increased elongations [55]. These additions are typically employed

alongside extreme mechanical processing routes such as Equal Channel Angular Extrusion which lead to extremely fine grain structures within alloys and subsequently very impressive elongations [56]. These processes are not viable industrially due to impracticality of processing sufficient material and also due to increased costs, scandium additions in particular are totally impractical financially with scandium currently costing $15,000/kg at the time of publishing [57].

### *2.3.4. Hybrid Processes*

Hybrid SPF processes are forming processes that aim to take advantage of certain aspects of SPF forming such as low residual stress and zero springback but try to overcome the main disadvantage which is cycle times to form parts. Hybrid SPF forming processes reduce the cycle times by means of either increased strain rates or use of both low strain rate forming combined with a physical deformation stage (mechanical pre-drawing) usually before a final gas forming stage. This reduction in cycle time and increase in strain rate is said to lead to shift from grain boundary sliding to dislocation creep as the primary deformation mechanism [42].

To reduce cycle times a “Quick Plastic Forming” or QPF system was developed by GM motors which was used with a 5083 alloy to produce a one piece boot lid for the 2004 Chevy Malibu Maxx which had previously been a two piece construction [58]. The QPF process employed forming at greater strain rates made possible by higher temperature forming. Effective material heating was identified as a critical component of the forming process and significant work was carried out in the design of the heating and control systems [58].

The QPF process was suitable for panels with less complex geometry than those that would be formed in an SPF process however still more complex than by conventional stamping. The investment between a QPF and SPF process is also loaded differently, SPF requires lower initial investment with cheaper tooling however with higher material and running costs. QPF requires higher investment in machinery, but reduced cycle times and increased production volume lead to an overall reduction in final part cost [59].

The other option for hybridisation of SPF is the use of a mechanical pre-forming stage within the process which has been investigated at several universities and extensively by the Ford motor company [60]. This process comprises a first stage where the material is heated and then deformed by means of hot stamping, after this point gas pressure is applied which completes the final and more complex stage of the forming [60]. This process is shown in fig.11.

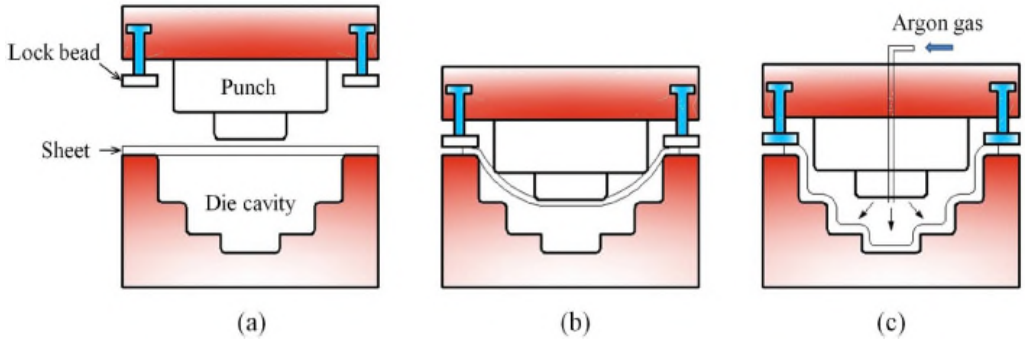

Fig.11. Schematic of a hybrid forming process [60].

Trials of this forming method termed HDMP "hot draw mechanical pre-forming" showed the capability to produce a part in 140 seconds using a strain rate of $10^{-3}$ $s^{-1}$ for the final gas blowing stage when compared to 20 minutes for a pure SPF forming of the same part with the same $10^{-3}s^{-1}$ strain rate [61]. The formed parts were also seen to have less cavitation than those produced using a purely SPF process [62], this is attributed to the material draw in during the initial stamping stage, something which does not occur during SPF forming due to the clamp forces required to form as a gas tight seal [63].

### *2.3.5. High Temperature Lubrication*

Methods and materials for lubrication and part release are an important area, particularly within hybrid SPF processes where materials will contact male radii's during the physical stage of forming. The standard lubrication used within industry is a colloidal graphite "dag" which provides a good level of lubricity with a coefficient of friction around 0.1 which works well in a traditional SPF process, colloidal graphite acts as a release agent as well. There has been significant research which has shown that lubrication needs to be tailored across certain areas of the die in particular the entry radius to allow for successful forming of parts [64-66].

Studies have looked at the impact of lubrication during SPF forming both experimentally and by means of FEM simulation. Various Al alloys including 5083[65], 8090 [66], 7475 [64] and magnesium alloy AZ31 [67] have been investigated. All the studies agree on the principle that localised thinning occurs at the die entry radius forming into a region of plane strain, the reason for this is due to the lubrication used the material "slips" in this region which allows for localised material flow and consequent thinning (illustrated in fig.12). To counteract this issue, lubricants with lower lubricity than graphite dag are employed, generally boron nitride or magnesium hydroxide (milk of magnesia) and combinations thereof [68].

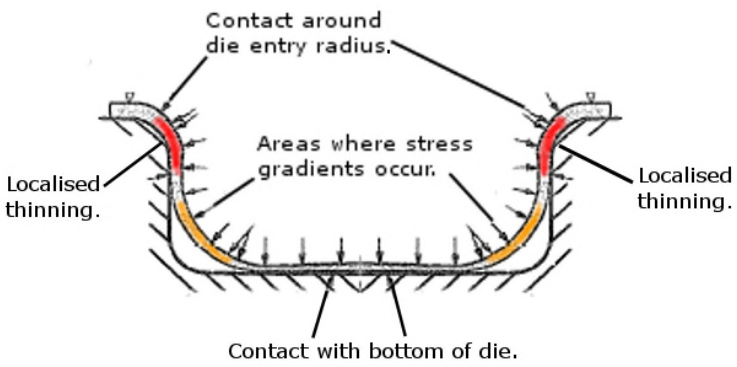


Fig.12. Areas of stress gradient occurrence during an SPF forming process.

Taleff et. al. used gas bulge testing combined with FEM analysis to look at the thinning of 5083 material at the die entry, which showed that slipping of the material in contact before the die entry leads to greater localised thinning. Simulation and testing was used to establish the use of milk of magnesia in the areas near to die entry which has a coefficient of friction of 0.4 compared to 0.1 for standard graphite dag, this lead to significant improvements in uniformity of material thinning [69]. US Patent #5,819,572 presents a lubrication system for hot forming. Testing was carried out using 5083 alloy in an SPF forming process and mixtures of boron nitride and milk of magnesia were proposed and tested. The patent states that the use of milk of magnesia helps to reduce cycle times and failures due to thinning, and highlights the use of boron nitride milk of magnesia mixtures in regions of plane strain where higher lubricity is required [68].

Further studies on 5083 within a QPF process used to produce Cadillac trunk lids by experimentation and FEM using two different models looked at using different lubricants with coefficients of friction from 0-0.5. The work showed that for lower values of μ premature thinning and failure was observed, whereas increasing the value to 0.5 totally eliminated thinning. A value of 0.12 in areas of plane strain was proposed which gives a good correlation with graphite and milk of magnesia [70]. A review paper on tribological issues during QPF [71], gives an overview of current state of the art and potential research areas in terms of QPF forming and its tribological issues which can be applied to SPF forming and are applicable for the hybrid forming being developed in this project. The paper again highlights the need for targeted lubrication. In areas where there is a die entry radius then a high μ is required to decrease localised thinning, whereas for the rest of the tool a low value is better to allow for more material flow which decreases thinning elsewhere in the part [71].

## 3. Experimental Programme

### *3.1. Experimental Materials*

Throughout this study work has been conducted on a commercially available AA7020 alloy. Submissions two and three investigated a series of twelve alloys based around AA7020 with differing alloying elements to assess the influence of said elements on formability and strength, with AA7020 being used as a performance benchmark. Varying amounts of nickel and mischmetall MM (which is a mixture of rare Earth elements Ce, La, Pr and Nd which are within set limits but can vary significantly) were added to AA7020 in combination with various homogenisation treatments.

Alloy compositions are listed in table 3 and homogenisation treatments in table 4. Additions to alloys were chosen based on previous work which had shown improved formability of 7000 series alloys with the addition of nickel in various wt% [51-53]. Two levels of nickel addition 1 wt% and 1.6 wt% were chosen by Hydro Aluminum based on this research.

Table.3. Compositions of experimental alloys.

| | **Composition (wt%) Remainder Al** | | | | | | | | | | |
|---|---|---|---|---|---|---|---|---|---|---|---|
| **Variant** | **Zn** | **Mg** | **Ni** | **MM** | **Mn** | **Zr** | **Cr** | **Ti** | **Si** | **Fe** | **Cu** |
| **AA7020** | 4.5 | 1.6 | 0 | - | 0.22 | 0.1 | 0.2 | 0.02 | 0.05 | 0.1 | 0.002 |
| **V0A** | 4.6 | 1.26 | 0.01 | - | 0.22 | 0.104 | 0.19 | 0.019 | 0.054 | 0.097 | 0.004 |
| **V0B** | 4.6 | 1.26 | 0.01 | - | 0.22 | 0.104 | 0.19 | 0.019 | 0.054 | 0.097 | 0.004 |
| **V1A** | 4.63 | 1.49 | 0.01 | - | 0.22 | 0.091 | 0.2 | 0.024 | 0.047 | 0.101 | 0.002 |
| **V1B** | 4.63 | 1.49 | 0.01 | - | 0.22 | 0.091 | 0.2 | 0.024 | 0.047 | 0.101 | 0.002 |
| **V2B** | 4.49 | 1.23 | 1.01 | - | 0.23 | 0.087 | 0.19 | 0.016 | 0.049 | 0.094 | 0.002 |
| **V2C** | 4.49 | 1.23 | 1.01 | - | 0.23 | 0.087 | 0.19 | 0.016 | 0.049 | 0.094 | 0.002 |
| **V3B** | 4.57 | 1.25 | 1.61 | - | 0.22 | 0.101 | 0.2 | 0.022 | 0.05 | 0.098 | 0.002 |
| **V3C** | 4.57 | 1.25 | 1.61 | - | 0.22 | 0.101 | 0.2 | 0.022 | 0.05 | 0.098 | 0.002 |
| **V4A** | 4.44 | 1.21 | 0.02 | 0.95 | 0.23 | 0.099 | 0 | 0.017 | 0.047 | 0.096 | 0.001 |
| **V4B** | 4.44 | 1.21 | 0.02 | 0.95 | 0.23 | 0.099 | 0 | 0.017 | 0.047 | 0.096 | 0.001 |
| **V5A** | 4.47 | 1.22 | 0.01 | 1.47 | 0.23 | 0.097 | 0 | 0.018 | 0.05 | 0.098 | 0.001 |
| **V5B** | 4.47 | 1.22 | 0.01 | 1.47 | 0.23 | 0.097 | 0 | 0.018 | 0.05 | 0.098 | 0.001 |

All experimental alloys were cast as 10 kg book casts and were hot rolled to 8 mm, annealed at 350°C for 2 hours, then finally cold rolled to 1.6 mm thickness. Four sheets of 200 mm x 200 mm size were available from each alloy, while AA7020 used was commercial 1.6 mm sheet.

Table.4. Homogenisation treatment temperature and duration for all alloys.

| | **Homogenisation Treatment** | | |
|---|---|---|---|
| **Variant** | **A (480°C 24hrs + 550°C 2hrs)** | **B (550°C 24hrs)** | **C (520°C 24hrs + 550°C 2hrs)** |
| **AA7020** | ✓ | - | - |
| **V0A** | ✓ | - | - |
| **V0B** | - | ✓ | - |
| **V1A** | ✓ | - | - |
| **V1B** | - | ✓ | - |
| **V2B** | - | ✓ | - |
| **V2C** | - | - | ✓ |
| **V3B** | - | ✓ | - |
| **V3C** | - | - | ✓ |
| **V4A** | ✓ | - | - |
| **V4B** | - | ✓ | - |
| **V5A** | ✓ | - | - |
| **V5B** | - | ✓ | - |

Following initial testing to assess material formability and suitability within an industrial forming process the alloy V3C showed the best formability across all test conditions and so was selected alongside the AA7020 for further investigation within submissions four and five. To allow for this a new larger batch of the material was cast and rolled by Hydro Aluminium. The compositions, homogenisation treatments and cast sizes are listed in tables five, six and seven respectively.

Table.5. Compositions of selected alloys V3C and larger cast V3CN.

| | Composition (wt%) Remainder Al | | | | | | | | | |
|---|---|---|---|---|---|---|---|---|---|---|
| **Variant** | **Zn** | **Mg** | **Ni** | **Mn** | **Zr** | **Cr** | **Ti** | **Si** | **Fe** | **Cu** |
| **AA7020** | 4.5 | 1.6 | 0 | 0.22 | 0.1 | 0.2 | 0.02 | 0.05 | 0.1 | 0.002 |
| **V3C** | 4.57 | 1.25 | 1.61 | 0.22 | 0.1 | 0.2 | 0.022 | 0.05 | 0.098 | 0.002 |
| **V3CN - 43080** | 4.67 | 1.21 | 1.68 | 0.22 | 0.147 | 0.16 | 0.017 | 0.057 | 0.089 | 0.001 |
| **V3CN - 43084** | 4.62 | 1.27 | 1.58 | 0.2 | 0.153 | 0.16 | 0.009 | 0.046 | 0.078 | 0.009 |

Table.6. Homogenisation treatments temperature and duration of alloys V3C and V3CN.

| Variant | Homogenisation Treatment |
|---|---|
| **V3C** | **520°C 24hrs + 550°C 2hrs** |
| **V3CN - 43080** | **550°C 24hrs** |
| **V3CN - 43084** | **550°C 24hrs** |

Table.7. Weight and dimension of castings of alloys V3C and V3CN.

| Variant | Weight (Kg) | Dimensions (mm) |
|---|---|---|
| **V3C** | 10 | Unknown |
| **V3CN - 43080** | 65 | 350 x 126 (Scalped to 106 before rolling) |
| **V3CN - 43084** | 70 | 350 x 126 (Scalped to 106 before rolling) |

Both batches followed the same processing route, after casting they were homogenised, then directly hot rolled to 8 mm +/- 0.1 mm hot strip. They then underwent a simulated coil annealing (2 hours at 350 °C with slow heat up and cool down). After annealing they were then cold rolled to a final gauge of 1.6 mm +/- 0.1 mm.

### *3.2. Uniaxial Tensile Testing (Submissions 2,3,4)*

#### *3.2.1. Methodology*

Uniaxial elevated temperature tensile testing was conducted using an Instron 5742 load frame with an integrated furnace to assess material formability. Tests were controlled using Instron Wave Matrix V.2.35 software operating in strain rate control to achieve constant strain rates throughout testing. Dog bone shaped coupons were prepared as shown in fig.13 using a Daytron CNC machine, having a 15 mm gauge length. No lubrication was used during testing as the area of deformation was not in contact with the sample grips

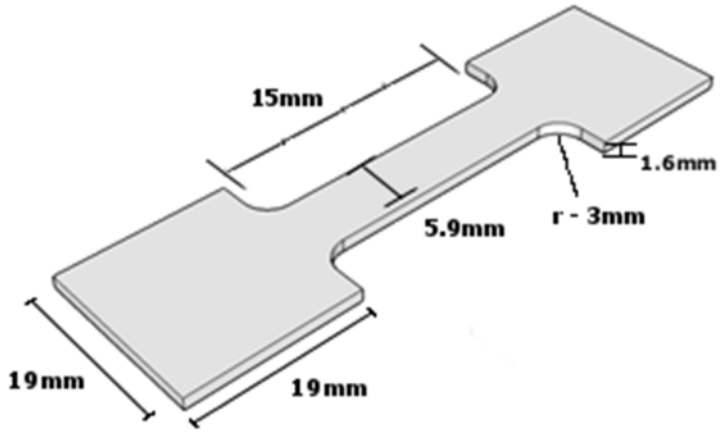


Fig.13. Elevated temperature tensile test dogbone sample geometry.

Initial tests (detailed in portfolio submission two) were carried out over a wide range of temperatures and strain rates to identify which alloy performed best across all conditions and also the maximum elongation achievable for each alloy. All samples were subjected to a five minute preheat stage to ensure they were fully solutionized and recrystallized before commencing testing, the matrix of tests is listed in table 8. Values for true stress were taken at 0.1, 0.3, 0.5 and 0.7 strain and the log values plotted vs. the log of the strain rate, the slope of this graph yielding the “m” value for the alloys.

Table.8. Uniaxial testing matrix, temperature and strain rates for all alloys.

| | | Strain Rate ($s^{-1}$) | | | | | |
|---|---|---|---|---|---|---|---|
| **Preheat Time(Mins)** | **Temperature (°C)** | **$1x10^{-1}$** | **$5x10^{-2}$** | **$1x10^{-2}$** | **$5x10^{-3}$** | **$1x10^{-3}$** | **$5x10^{-4}$** |
| **5** | **450** | ✓ | ✓ | ✓ | ✓ | ✓ | ✓ |
| | **475** | ✓ | ✓ | ✓ | ✓ | ✓ | ✓ |
| | **500** | ✓ | ✓ | ✓ | ✓ | ✓ | ✓ |

Following initial trials, further tests were conducted on AA7020 and the best performing alloy (V3C) to establish the effect of preheat time on the material formability. This testing was detailed fully in portfolio submission three. The V3CN material was then subjected to the same matrix of testing detailed in portfolio submission four and shown in table 9.

Table.9. Uniaxial testing matrix, temperature and strain rates for alloys AA7020, V3C and V3CN.

| | | Strain Rate ($s^{-1}$) | | |
|---|---|---|---|---|
| **Preheat Time(Mins)** | **Temperature (°C)** | **$1x10^{-1}$** | **$1x10^{-2}$** | **$1x10^{-3}$** |
| **1** | **480/500** | ✓ | ✓ | ✓ |
| **2** | **480/500** | ✓ | ✓ | ✓ |
| **5** | **480/500** | ✓ | ✓ | ✓ |

### *3.2.2. Results*

Results from the initial trials of all alloys are shown for 475°C in fig.14 and for 500°C in fig.15. Alloys AA7020 and V3C have been highlighted on both plots for ease of identification. m values for all alloys, including the V3CN, are listed in table 10 the m value being the strain rate sensitivity which for a superplastic material would typically be around 0.5.

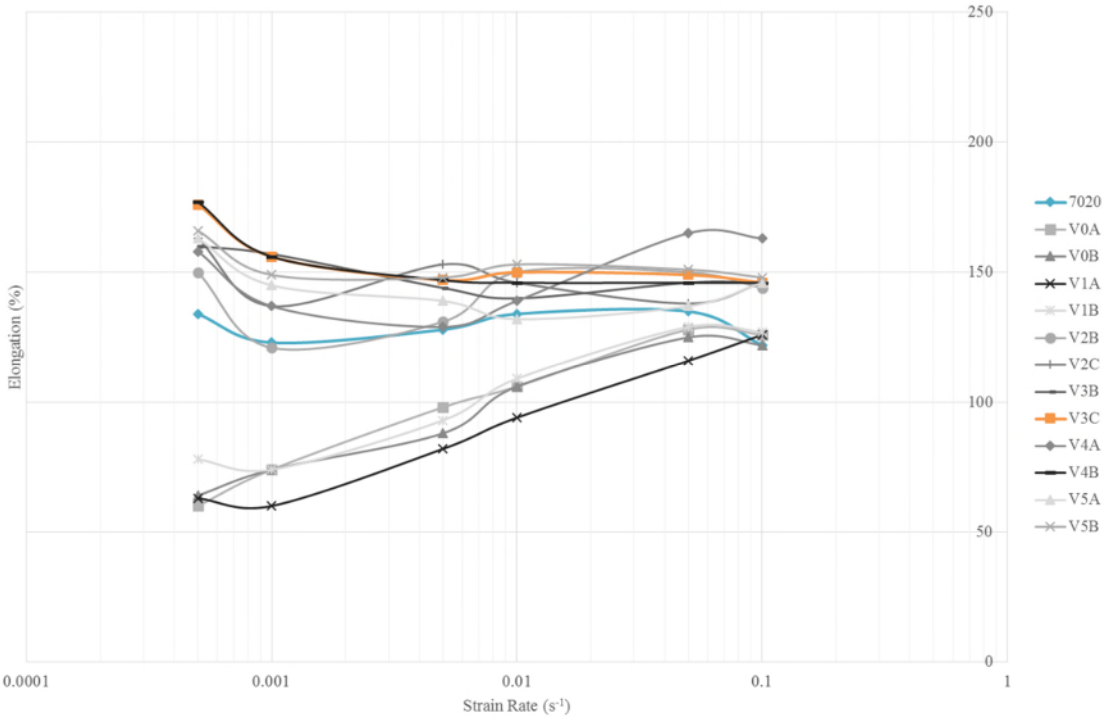


Fig.14. Elongation to failure vs strain rate for all alloys at 475°C, AA7020 and V3C highlighted.

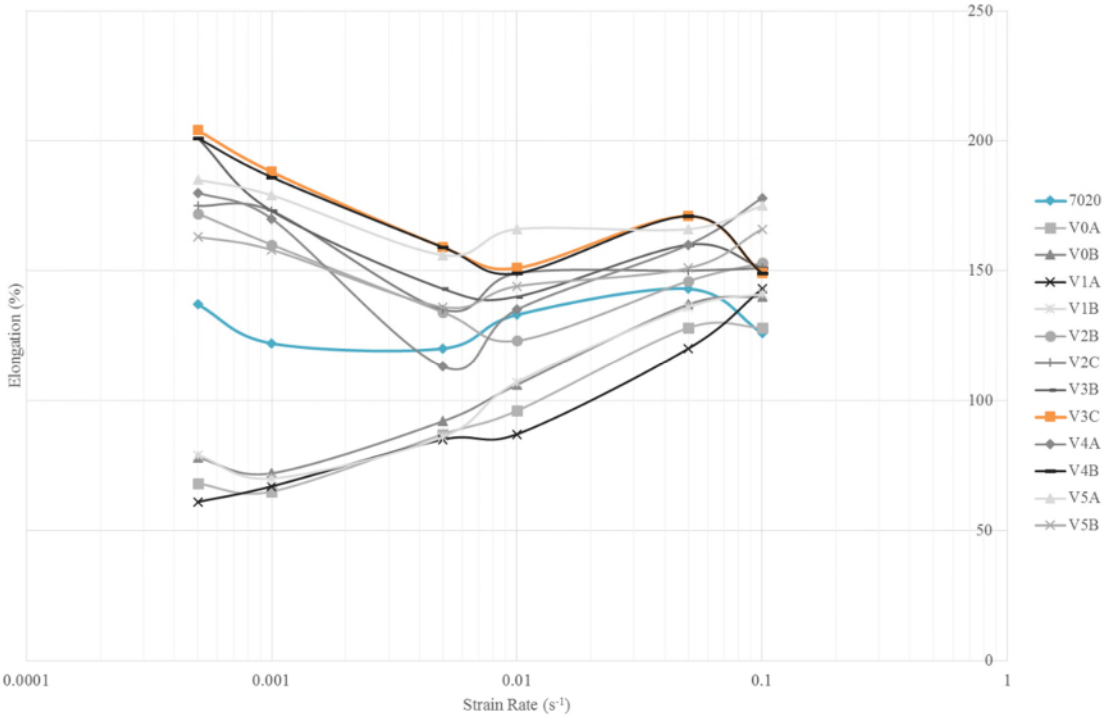


Fig.15. Elongation to failure vs strain rate for all alloys at 500°C, AA7020 and V3C highlighted.

Table.10. Calculated m values from tensile testing for all alloys.

| | m-Value for Various Temperatures | | | |
|---|---|---|---|---|
| **Material** | **450°C** | **475°C** | **500°C** | **Avg.** |
| **AA7020** | 0.17 | 0.18 | 0.18 | 0.18 |
| **V0A** | 0.16 | 0.17 | 0.15 | 0.16 |
| **V0B** | 0.17 | 0.19 | 0.18 | 0.18 |
| **V1A** | 0.18 | 0.20 | 0.18 | 0.19 |
| **V1B** | 0.19 | 0.20 | 0.18 | 0.19 |
| **V2B** | 0.19 | 0.21 | 0.21 | 0.20 |
| **V2C** | 0.20 | 0.21 | 0.20 | 0.20 |
| **V3B** | 0.21 | 0.24 | 0.23 | 0.23 |
| **V3C** | 0.21 | 0.25 | 0.26 | 0.24 |
| **V4A** | 0.21 | 0.22 | 0.23 | 0.22 |
| **V4B** | 0.20 | 0.24 | 0.22 | 0.22 |
| **V5A** | 0.20 | 0.22 | 0.22 | 0.21 |
| **V5B** | 0.22 | 0.22 | 0.21 | 0.22 |

All samples were tested to failure, following testing values for true stress were taken at 0.1, 0.3, 0.5 and 0.7 strain and the log values plotted vs. the log of the strain rate, the slope of this graph yielding the m value for the material. These results allowed the maximum elongation of the material to be found, and the average strain rate sensitivity m values of the materials to be established across a wide range of strain rates and temperatures. These results are detailed in table.10.

Results from testing with varied preheat times for AA7020 at 480°C are shown in fig.17 and 500°C in fig.18. The results for V3C at 480°C are shown in fig.16. Due to a lack of material the V3C was tested only at 480°C and due to lower formability at 450°C this temperature was dropped from further investigation. Results for V3CN at 480°C and shown in fig.19 and at 500°C in fig.20. Error bars show standard deviation for all tests other than V3C which due to a lack of experimental material were only single tests.

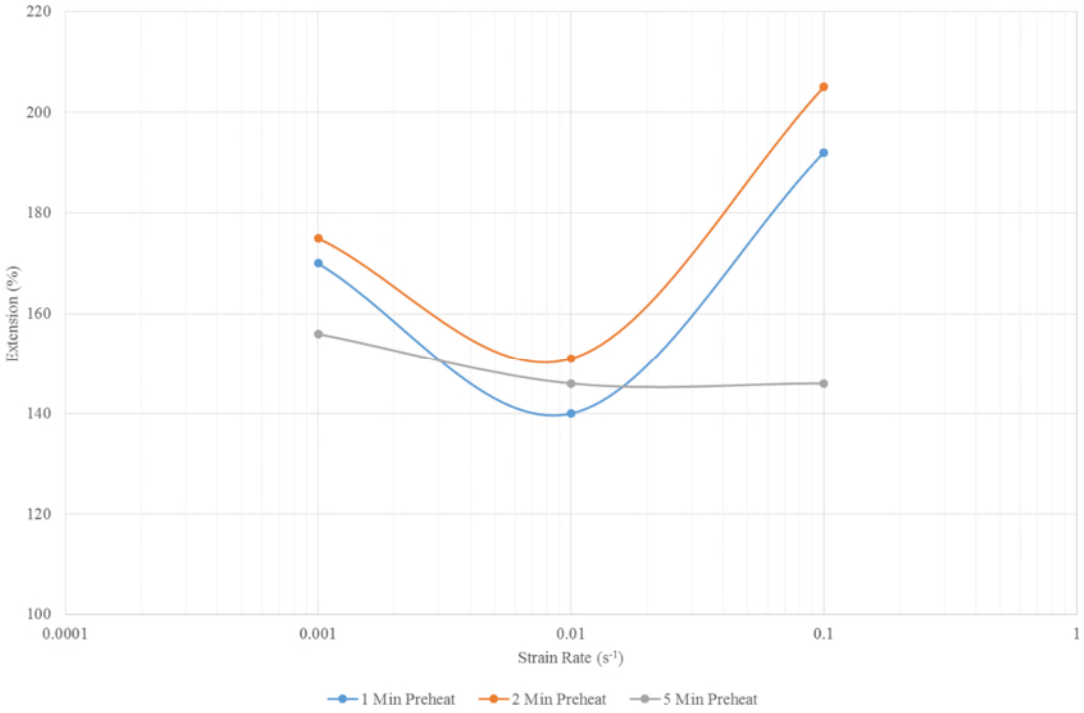


Fig.16. V3C Elongation to failure vs strain rate for various preheats at 480°C.

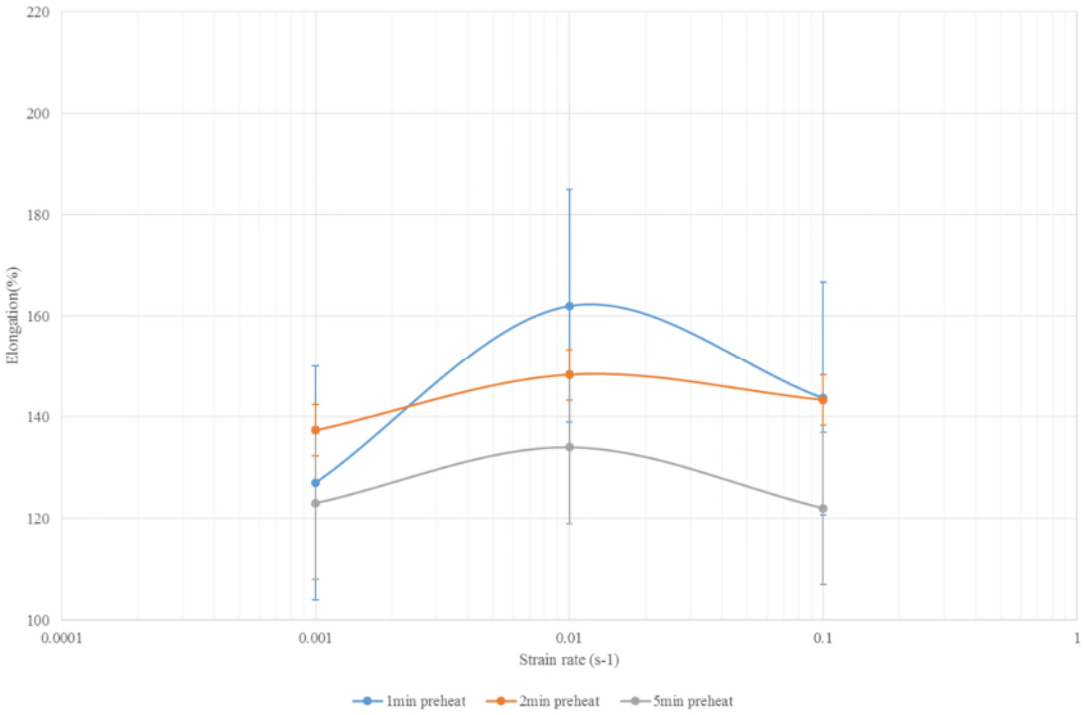


Fig.17. AA7020 Elongation to failure vs strain rate for various preheats at 480°C.

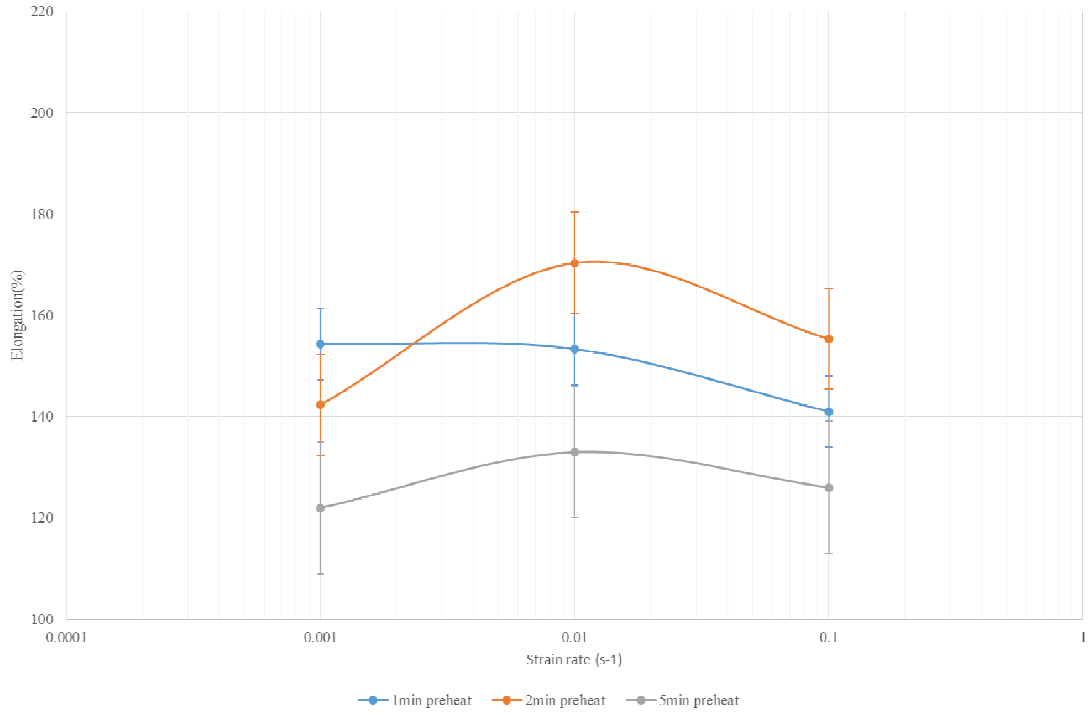


Fig.18. AA7020 Elongation to failure vs strain rate for various preheats at 500°C.

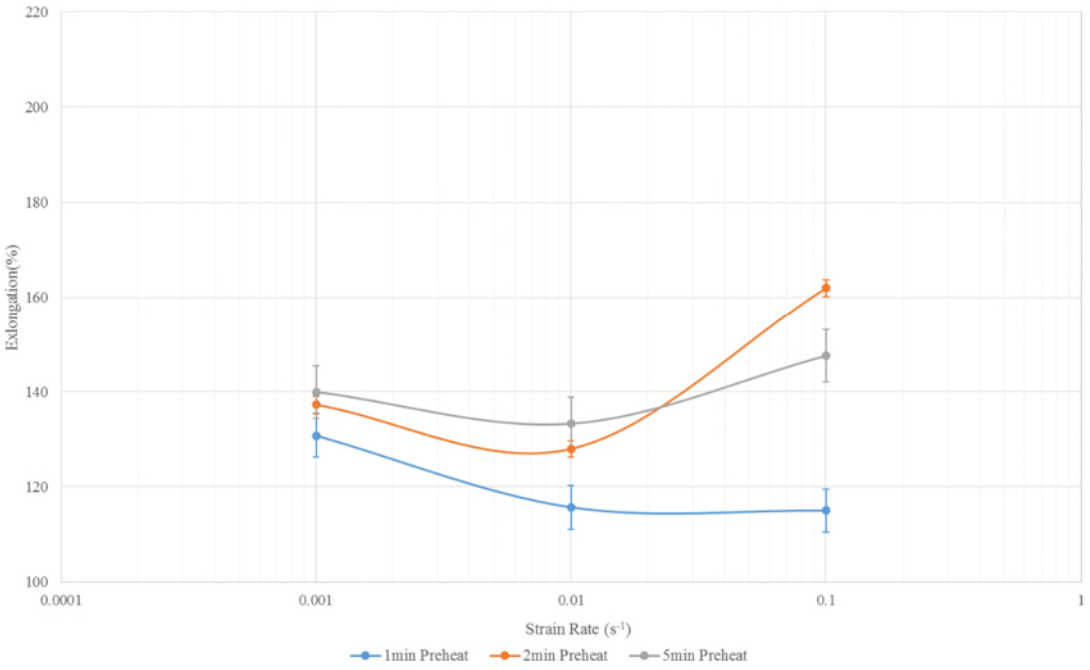


Fig.19. V3CN Elongation to failure vs strain rate for various preheats at 480°C.

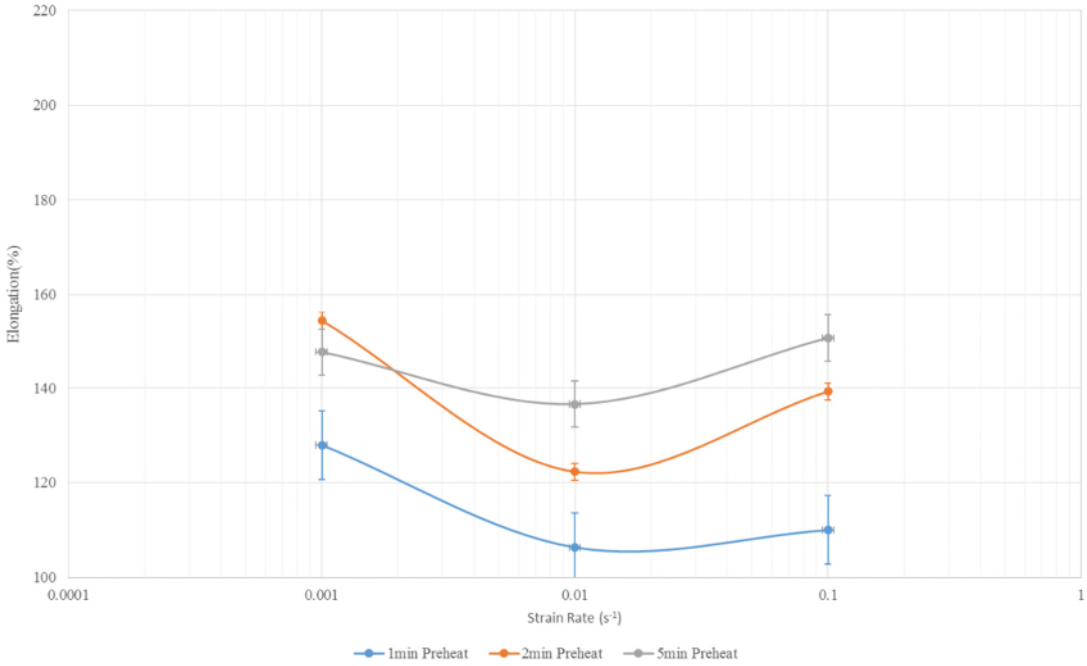


Fig.20. V3CN Elongation to failure vs strain rate for various preheats at 500°C.

### *3.2.3. Discussion*

Initial testing showed the poor performance of the V0A, V0B, V1A, V1B alloys which all showed lesser formability compared to the other AA7020 variants, particularly at lower strain rates. The alloys all showed a preference for forming at higher strain rates and at $1x10^{-1}s^{-1}$ the formability was comparable to the AA7020.

All other alloys which contained either mischmetall or nickel additions showed varying amounts of increased formability compared to the AA7020, there was also a slight trend particularly at 500°C towards forming at lower strain rates. The V3C material highlighted in orange in the fig.14 and 15 achieved the maximum elongation of all alloys tested at 204%. The V3C when compared across all test conditions was observed to be the most formable. These results combined with the materials impressive formability in cone

testing as detailed in section 3.3.3 of this report led to its selection for further investigation and casting on a larger scale.

The reason for increased formability of the alloys with mischmetall or nickel additions was attributed to increased static recrystallization driven by particle stimulated nucleation (PSN) due to the additional Ni and MM containing secondary particles in these alloys. From this testing the combination of 1.6wt% nickel and the two stage homogenisation treatment of 520°C for 24 hours and 550°C for 2 hours within the V3C showed the best overall performance.

Varied preheats applied to the V3C showed a preference towards forming at higher strain rates and with shorter preheats, achieving a maximum elongation of 206% at $1x10^{-1}s^{-1}$ with a two minute preheat. The results suggest some instability within the material structure with a short preheat which is aiding formability, after a five minute preheat this increase in formability at higher strain rates is lost indicating a more fully recrystallized stable structure before forming.

AA7020 at both temperatures showed a slight preference towards forming at $1x10^{-2}s^{-1}$ strain rate, again with a preference to shorter preheat times with the five minutes preheat leading to the lowest elongations at both temperatures. This is suggesting some grain coarsening after five minutes which would have a negative impact on the materials formability. The alloy also showed better performance at 500°C achieving a peak 170% elongation at $1x10^{-2}s^{-1}$ with a two minute preheat.

The V3CN showed a significant decrease in formability when compared to the original V3C alloy and was seen to be less formable than the AA7020. There was still some evidence of the preference for forming at higher strain rates and shorter preheats as exhibited by the original V3C but the elongations were reduced from a peak of 206% at

$1x10^{-1}s^{-1}$ with a two minute preheat to a peak of 160% under the same conditions. Unlike AA7020 the material showed worse performance during testing at the higher temperature of 500°C, suggesting different mechanisms responsible for the deformation.

The decreased formability of the V3CN in relation to the V3C is attributed to the same $Al_3Ni$ particles which are responsible for the V3Cs increased formability in relation to the AA7020. These particles aid recrystallization by means of PSN leading to a finer grain structure and better formability, however due to the differences in processing and different homogenisation treatment between the V3C and V3CN it is likely both the size and distribution of these particles has been altered. The different size and distribution of the $Al_3Ni$ within the V3CN leads to a finer grain structure than the AA7020, but these particles then go on to act as nucleation sites for cavitation which lead to premature failure of the alloy. The size and distribution of these particles are detailed in section 3.6.2 of this report.

### *3.2.4. Conclusion*

Elongations of AA7020 are below that of what would be termed a superplastic material, but the alloy does offer industrially useful levels of formability for hybrid SPF forming processes as discussed in section 2.3.4. The alloy was capable of achieving 170% linear elongation at a medium strain rate of $1x10^{-1}s^{-1}$ when tested at 500°C with a two minute preheat.

Additions of 1.6wt% nickel in combination with a two stage homogenisation, 520°C 24hrs + 550°C 2hrs lead to significant improvements in terms of formability in the 10 kg cast V3C alloy. V3C was capable of achieving peak elongations of 206% under optimum forming conditions for the alloy.

Differences in processing route and homogenisation treatment of V3CN material have had a severely detrimental effect on material formability reducing peak elongation from 206% to 160%. Further investigation of alternative processing routes (casting, homogenisation and rolling regime) is required to establish whether the formability of the V3C could be replicated on a larger industrial scale.

### *3.3. Gas Bulge Testing (Submissions 2,4,5)*

#### *3.3.1. Methodology*

Gas bulge testing was conducted on two different cone testing rigs which apply pressure in different ways, this allowed for a better understanding of the material behaviour within a gas forming process. Firstly, an SPF biaxial cone test press with internal heated platens that uses ramp rates to build pressure over time was used to investigate formability of all 13 alloys. This work was covered in submissions two and four of the portfolio.

Secondly, to further investigate the formability of the AA7020 and V3CN as well as the influence of lubrication systems when forming over a male radius, testing was carried out on a heated cone tester which builds pressure behind a valve, and then releases the full test pressure instantly to the sample. This test rig utilised stepped inserts to form truncated cones with a sharp central male radius. Testing was conducted as part of the EngD international placement and is fully detailed in submission five.

Samples of all materials were cut to 200 mm x 200 mm blanks and lubricated using graphite lubrication during initial tests, and by graphite, a lower lubricity lubricant or a combination of both during further testing. The cone tester was set to the required temperature for testing and then allowed to stabilise before testing. Samples were then

loaded and allowed to preheat for the desired length of time before gas pressure was applied.

Initial testing used a Druck Pace 1000 pressure indicator to establish the time at which failure had occurred (indicated by a pressure drop in the system). The cone tester used in conjunction with the truncated cones used an internal sensor to detect a pressure drop within the system. Cone height after forming vs time to form said cone was used as the metric to evaluate material formability in the first instance. Testing using truncated cones was used to establish the limits of the materials formability in this instance, and to investigate the influence of lubrication.

### *3.3.2. Results*

### *3.3.3. Initial Trials (Submissions 2,4)*

Full results from the initial tests are detailed in portfolio submission two and the most important results are shown in fig.21 and fig.22. Fig.21 shows the results from testing at 45 Psi which was used to compare all materials. These tests highlighted the nickel containing variant V3C as the best performing alloy. Tests were then conducted on the best performing alloys at the lower pressure of 35 Psi to see if forming at a lower strain rate would yield greater cone heights. The results as shown in fig.22 show a slight increase in cone height for the AA7020 material and no difference in the V3C cone height, suggesting that the material could be successfully formed at higher strain rates.

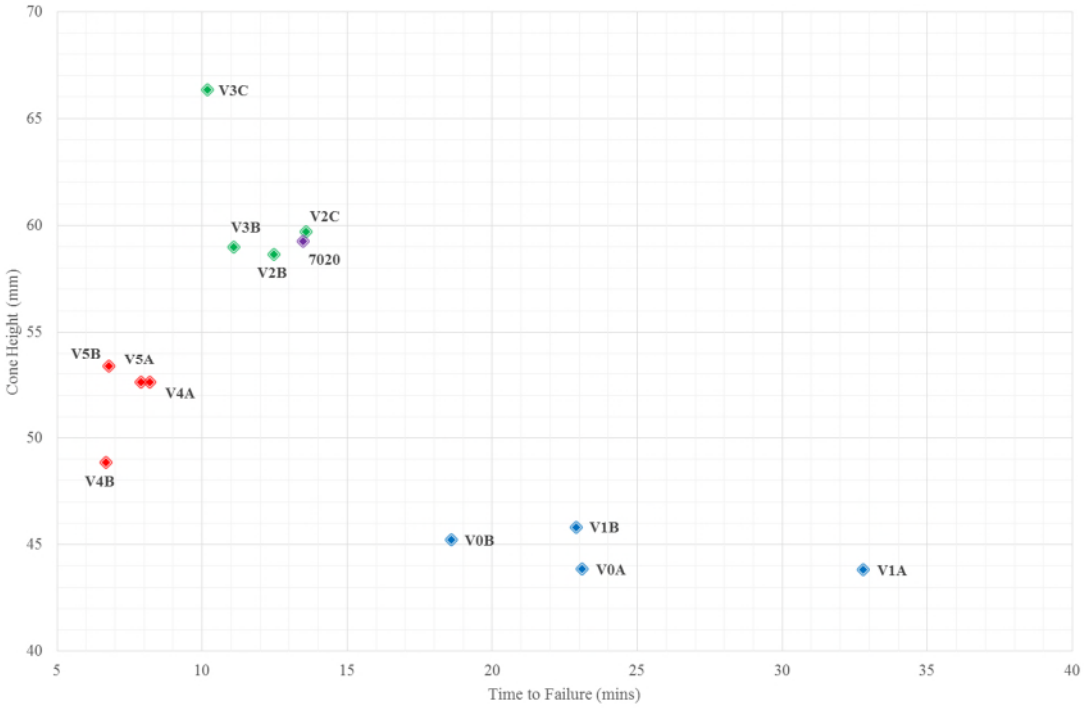


Fig.21. Cone height to failure vs. failure time for all materials at 45 Psi.

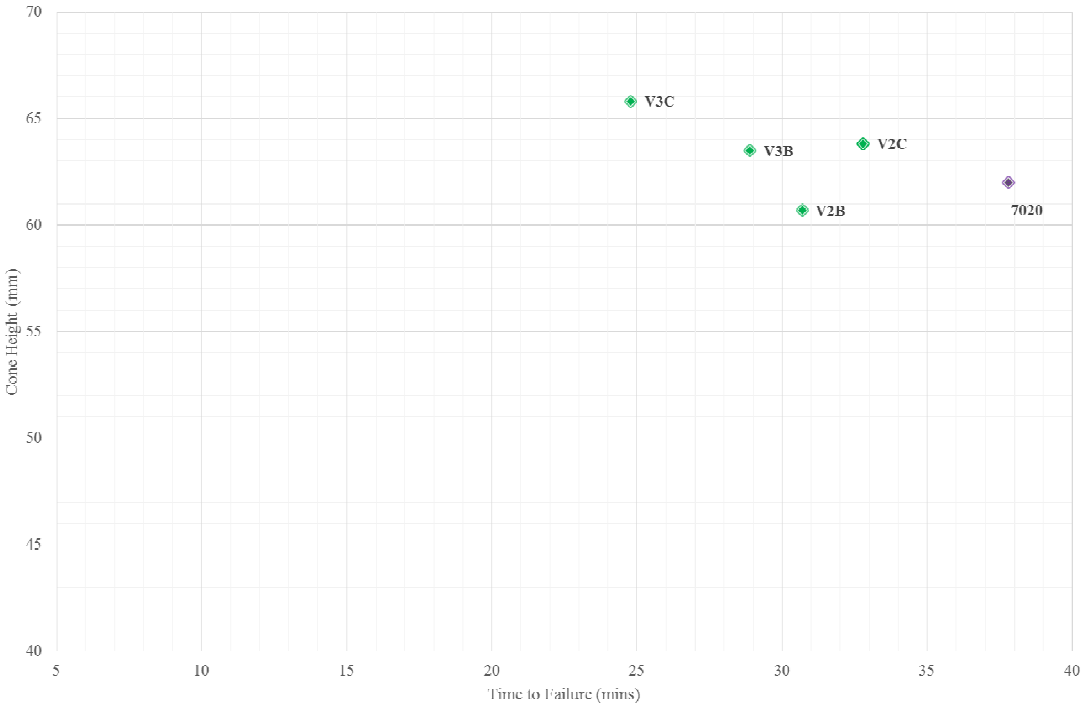


Fig.22. Cone height to failure vs. failure time for V3C and AA7020 materials at 35 Psi.

The results from this testing, in combination with tensile testing showed the increased formability of the V3C material along with increased post forming strength. These factors

led to the selection of the V3C material for further investigation alongside the AA7020 material. To facilitate this further investigation a 2nd batch of V3C was cast in a larger scale and rolled to 1.6 mm thickness. This new batch was termed V3CN to distinguish it from the original V3C material.

Testing of the V3CN and AA7020 was then conducted at 44 Psi, 75 Psi and 135 Psi, with the average strain rate calculated after testing from the equivalent strain at the cone peak. The equivalent strain was calculated from material thinning which was measured by an ultrasonic tester after forming. Samples were preheated for one, two or five minutes to investigate the influence of preheat on formability in gas bulging tests. The results of this testing for the AA7020 are shown in fig.23 and V3CN in fig.24.

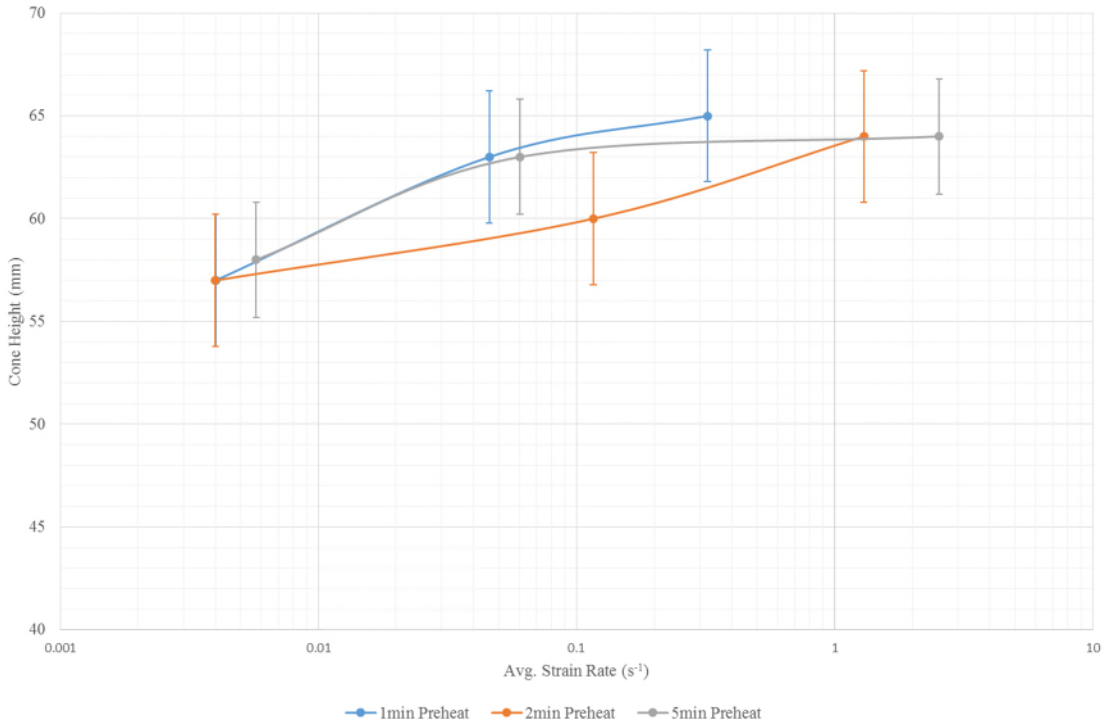


Fig.23. AA7020 Cone heights to failure vs strain rate for various preheat times at 480°C.

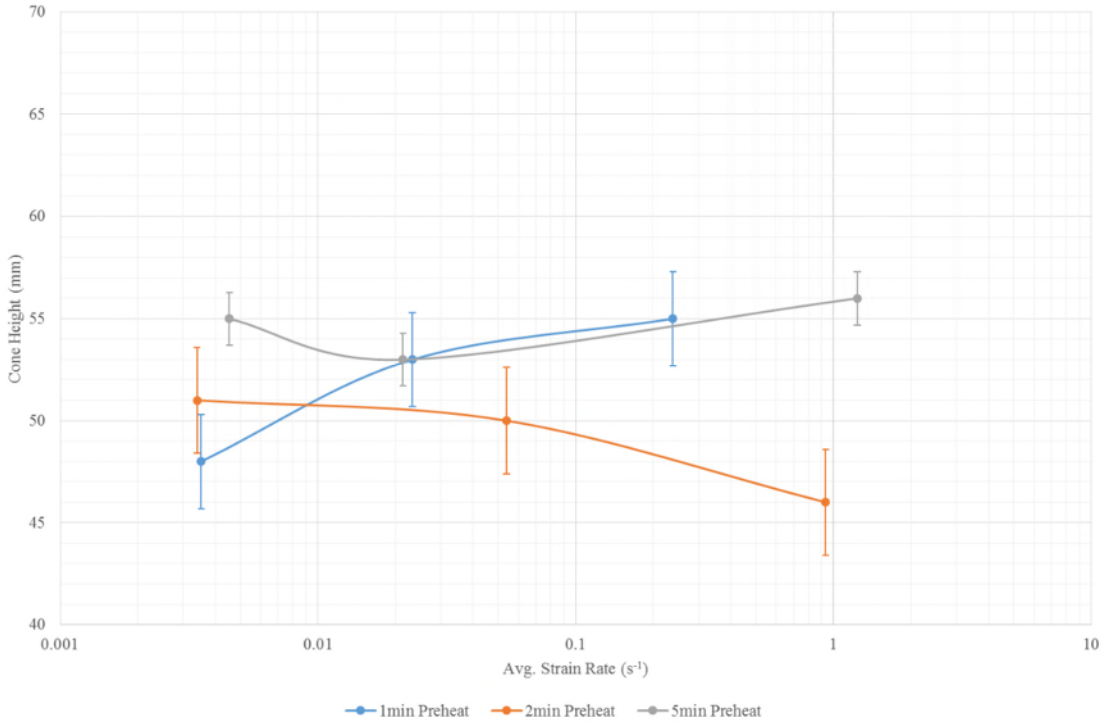


Fig.24. V3CN Cone heights to failure vs strain rate for various preheat times at 480°C.

### *3.3.4. Truncated Cones With Male Radius ( Submission 5)*

Previous testing at SUSA had identified a three minute preheat as the optimum time for the test rig and all tests were carried out with this preheat. The geometries of the stepped inserts are shown in fig.25 and were chosen to assess the limits of material formability across male radii, an area where premature failures had been experienced in both industrial testing and at WMG. Both V3CN and AA7020 were tested at 135 Psi at both 495°C and 530°C with either graphite lubrication only or graphite and selected areas with lower lubricity lubrication shown in fig.26a and b alongside the SUSA cone tester. Selected tests were also carried out at the higher pressure of 200 Psi. A matrix of testing is shown in table.11 which summarises all tests on a failure/non failure basis.

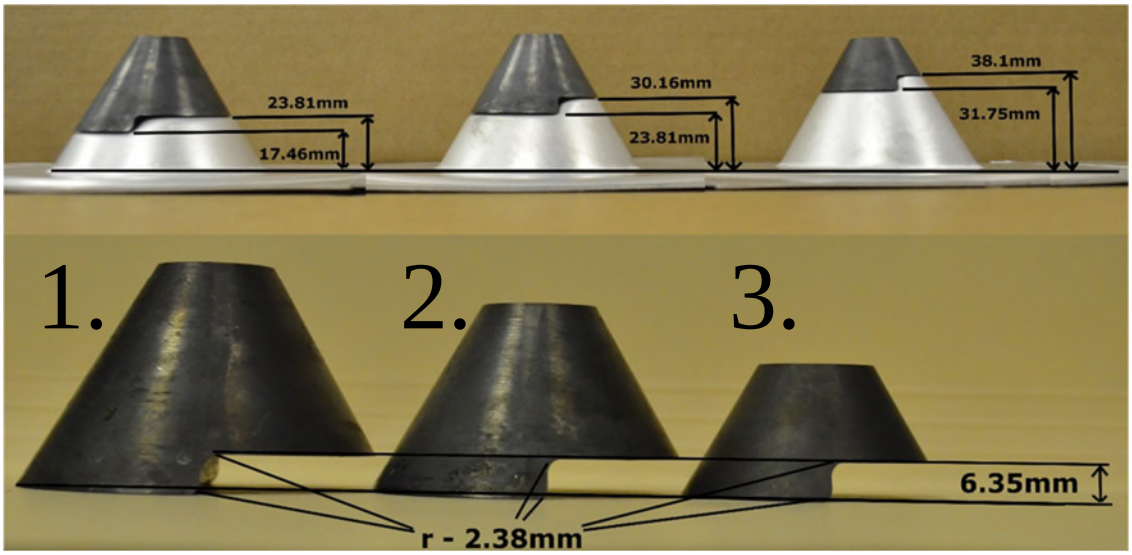

Fig.25. SUSA cone tester insert geometries.

Table.11. Failure matrix from testing at SUSA of AA7020 and V3CN.

| 135Psi 8.5 mins hold | | 7020 | | V3CN | | 200Psi 2.5mins hold | | 7020 | | V3CN | |
|---|---|---|---|---|---|---|---|---|---|---|---|
| | | G | G+M | G | G+M | | | G | G+M | G | G+M |
| 495°C | Insert 1 | ✘ | ✘ | ✓ | ✓ | 495°C | Insert 1 | .. | .. | .. | .. |
| | Insert 2 | ✘ | ✘ | ✘ | ✓ | | Insert 2 | .. | .. | ✘ | ✘ |
| | Insert 3 | ✘ | ✘ | ✘ | ✘ | | Insert 3 | ✘ | ✘ | .. | .. |
| 530°C | Insert 1 | ✘ | ✘ | ✓ | ✓ | 530°C | Insert 1 | .. | .. | .. | .. |
| | Insert 2 | ✘ | ✓ | ✘ | ✘ | | Insert 2 | .. | .. | .. | .. |
| | Insert 3 | ✘ | ✓ | ✘ | ✘ | | Insert 3 | ✓ | ✘ | .. | .. |

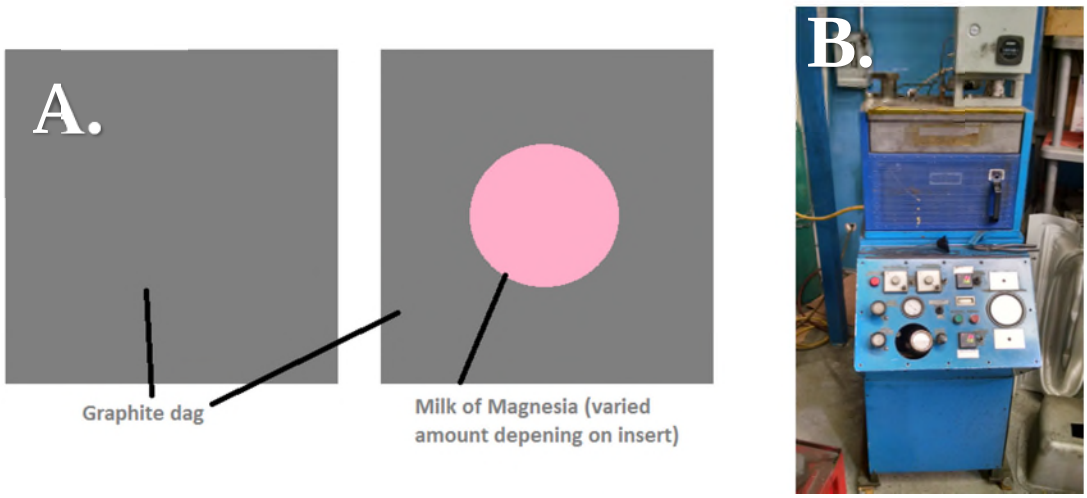

Fig.26. a) Showing areas of varied lubrication applied to samples, b) SUSA cone tester

The influence of rolling direction on AA7020 anisotropy was investigated by aligning the straight radius of the cone insert parallel, 45° and 90° to the material rolling direction. A previously successful forming test was selected; 530°C, 135 Psi, with mixed

lubrication. Samples were prepared as such and then loaded into the cone tester with the desired alignment and the pressure profile applied. The results of which are shown in fig.27. From this testing it appears that there is no influence on forming with all trials successfully forming the truncated cone. Earlier portfolio submissions have shown that after two minutes the material is fully recrystallized with an isotropic structure showing no evidence of rolling direction.

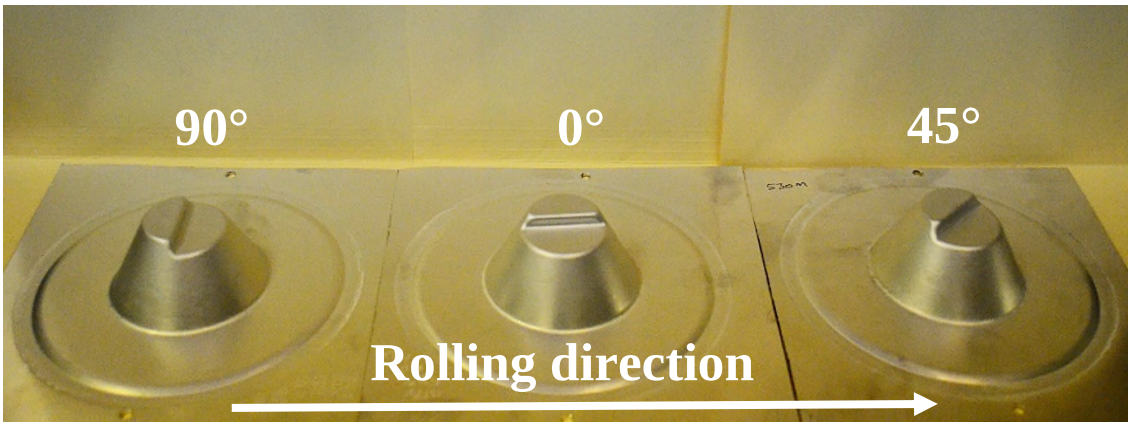

Fig.27. AA7020 Samples after testing at 135Psi and 530°C with varying alignment to tool edge.

### *3.3.5. Discussion*

Testing of the initial set of alloys confirmed results from tensile testing, showing that the V0A, V0B, V1A and V0B alloys with no additions had reduced formability compared to AA7020 despite the near identical chemistries. This was attributed to the smaller scale casts of the materials having undergone different processing to the industrial scale AA7020, alongside the difference in thermal treatment during cooling of the alloys which will have affected the grain structure and properties of the materials.

Tensile testing of V4A, V4B, V5A and V5B which contain mischmetall had been promising but within gas bulge tests these alloys were seen to underperform. This poor formability combined with the nature of mischmetall not having a totally controlled

composition and the difficulties in getting a commercial rolling mill to produce a full scale alloy containing mischmetall meant these alloys were excluded from further testing

The nickel containing V2B, V2C, V3B and V3C alloys offered equal or greater performance forming cones of similar or greater heights in a shorter time than AA7020. The V3C alloy in particular was outstanding in achieving the greatest cone height at both pressures in less time than AA7020. As with tensile testing detailed in section 3.2.3 the V3CN showed a significant decrease in formability compared to the smaller scale V3C alloy.

Both Ni containing alloys showed slightly increased formability at higher strain rates and showed no detrimental effects when using the shortest one minute preheat. This was promising in terms of the industrial process as shorter preheats and faster strain rates should allow for reduction in forming cycle times. As discussed previously the materials both have low m values which are well below those typical of a superplastic material and the elongations are below superplastic. This preference to faster forming at higher strain rates indicates conventional dislocation slip as the dominate deformation mechanism rather than grain boundary sliding which is dominant at lower strain rates.

Testing at SUSA showed that when tested with truncated cone geometries the AA7020 material was unable to successfully form any cones at 495°C. This was unexpected as cones and industrial parts had been successfully formed at this temperature previously. This showed the unsuitability of forming at this temperature in combination with truncated cone geometries which has aided tool design at Superform.

At the higher temperature of 530°C the AA7020 was able to successfully form cones using inserts two and three, which subject the material to greater strain than insert one, achieving strains of over 400%. Portfolio submissions three and four have shown the

AA7020 to have a coarser grain structure after static recrystallization than the V3CN. This increased formability at higher strains suggests possibly some dynamic recrystallization taking place during the forming, suggesting the need to experience sufficient strain before contact with the die to allow for recrystallization to occur, similar to the way in which AA2004 requires applied strain to achieve a recrystallized structure [44].

The V3CN material was capable of forming cones using inserts one and two at 495°C (mixed lubrication was required to form insert two) and insert one at 530°C the material showing some preference to forming at the lower temperature. These cones subject the material to lower levels of strain and the material exhibits a limit of around 80% strain with just graphite and around 105% strain in combination with mixed lubrication before failure. These results combined with testing carried out previously suggest a finer starting microstructure due to the $Al_3Ni$ particles present which later go on to detrimentally effect formality by inducing cavitation.

Based on the work at SUSA, a working hypothesis was formulated that both alloys undergo static recrystallization during the preheat stage. The V3CN undergoing more recrystallization due to greater levels of PSN due to the coarse $Al_3Ni$ particles leading to a finer initial grain structure. The coarser structure of the AA7020 then undergoes further grain refinement possibly due to dynamic recrystallization under applied strain during testing, whereas the V3CN fails prematurely due to the $Al_3Ni$ particles present causing cavitation and cracking around the particle/matrix interface.

With applied strain the difference in size and distribution of $Al_3Ni$ within the V3CN compared to the V3C leads to premature failure by means of increased cavitation which nucleates at the $Al_3Ni$ particles. This phenomenon was investigated by means of EBSD

and by heated stage EBSD/FSD analysis both in submission four and in section 3.6 and 3.7 of this report.

As reported in portfolio submission five, to enable successful forming of parts over male radii the use of lower lubricity magnesium hydroxide lubrication was required. This has the effect of significantly increasing the coefficient of friction to 0.4 in comparison to 0.1 in areas lubricated with graphite dag. Localised thinning of material occurs across male radii with higher lubricity, as it allows the material to “slip” in this region which leads to localised material flow and subsequent necking. The use of magnesium hydroxide to increase friction in these areas has the effect of stopping this slow and localised flow, reducing material thinning in these critical areas.

### *3.3.6. Conclusion*

V3C which has a 1.6wt% nickel in combination with a two stage homogenisation treatment of 520°C for 24 hours and 550°C for 2 hours showed a significant improvement in material formability compared to AA7020. The alloy achieved a maximum cone height of 66 mm in ten minutes compared to 61 mm in 38 minutes for the commercial AA7020 alloy. This was true of the small 10 kg lab scale cast.

The scale up of the V3C material (V3CN) lead to a significant decrease in formability, with the V3CN achieving a maximum cone height of only 55 mm compared to 66 mm for the lab scale material. The decrease in performance was due to the slightly different processing routes, the difference in solidification rates of the two casts, and to a lesser extent the single stage homogenisation treatment applied to the V3CN compared to the

two stage treatment of the V3C. The difference in $Al_3Ni$ particles arising from this varied processing is quantified in section 3.6.2.

AA7020 exhibited the ability to form around tight male radii under specific conditions and has highlighted the need to strain the material in order to achieve this. With insufficient strain the material will fail, either due to an insufficiently refined grain structure or due to the sheet thickness compared to the male radii. Under the correct conditions the material can achieve strains in excess of 400%.

The as-supplied V3CN also exhibited the ability to form around tight male radii, but the material has a limit of around 100% strain before failure. Without improvement this lower formability will limit the V3CNs suitability for use in applications requiring high levels of strain.

Targeted lubrication by means of graphite with coefficient of friction 0.1 in free flowing areas and magnesium hydroxide with coefficient of friction 0.4 in areas of die contact was required to form parts where the material contacts male radii. This targeted lubrication alters the coefficient of friction and limits localised flow in critical areas.

### *3.4. Interlaken Press Hot Gas Form Testing*

#### *3.4.1. Methodology*

Material formability within a process and forming cycle similar to those in industry were assessed using customised tooling designed for use on an Interlaken hydraulic press. The tool was designed to allow for some initial deformation by means of mechanical hot stamping of the material and then a final gas forming stage to achieve fine detail within the part. This forming concept was used to help take advantage of the materials warm

formability and counteract its low ‘m’ value which hinders the materials performance in a traditional SPF forming process.

This mechanical preforming stage takes place as the tooling is closed into what would be the “clamp” and “preheat” position during a traditional SPF forming cycle. This reduces the time required for a separate warm forming process stage and allows for less complex and cheaper tooling to be used. Should a separate moving punch be used to carry out the mechanical preform there would be the need for another stage in the forming cycle as well as requiring more expensive tooling. This would counteract one of the major selling points of SPF and SPF like forming processes within niche applications which is the low tooling costs.

The tool was designed to be modular, with future modifications possible depending upon application. The tool comprises a top hat central section with varying radii along its length. As shown in fig.28 the varying radii were used to assess material formability limits across male radii’s which will inform tool design within an industrial process. The tooling was designed with threaded holes on either side of the top hat section, allowing for further parts to be attached to alter the part geometry in the future for different applications; to mimic certain car parts such as B pillars, A pillars etc. Initially two blocks (shown in grey in fig.28) were designed to further complicate the geometry, the blocks again have varying radii at all points to assess the materials radii forming limits and where failure would occur during an actual forming process.

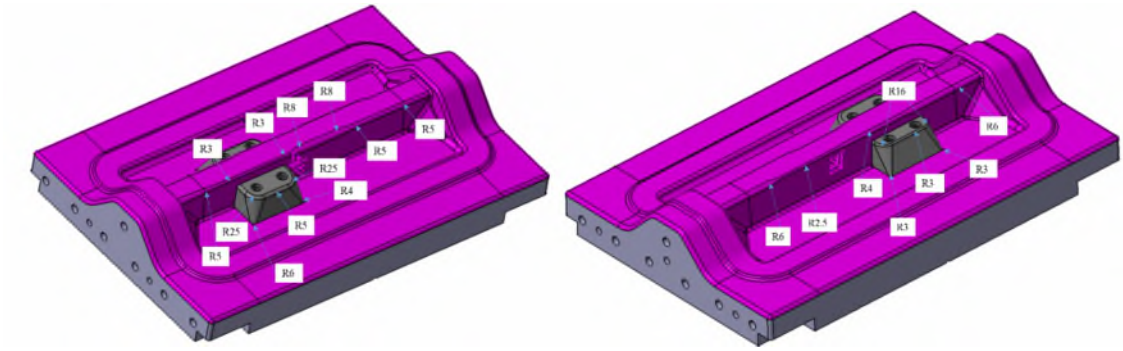

Fig.28. Tooling design with modular blocks shown in grey, all radii detailed in mm.

Testing was conducted on both AA7020 and V3CN 1.6 mm sheet as well as AA7020 2.0 mm and 1.2 mm sheet to give further ratios between male radius and sheet thickness to better assess material formability. Samples were lubricated with graphite dag lubricant, or with mixed lubrication as in cone testing in areas of contact with male radii and allowed to fully dry before testing. Heating of the tooling was controlled by a separate heater controller powering 14 heaters (seven in the upper platen and seven in the lower shown in fig.29b running lengthways within the tool, heaters were grouped together into 6 channels and K type thermocouples were used to monitor each heater throughout testing.

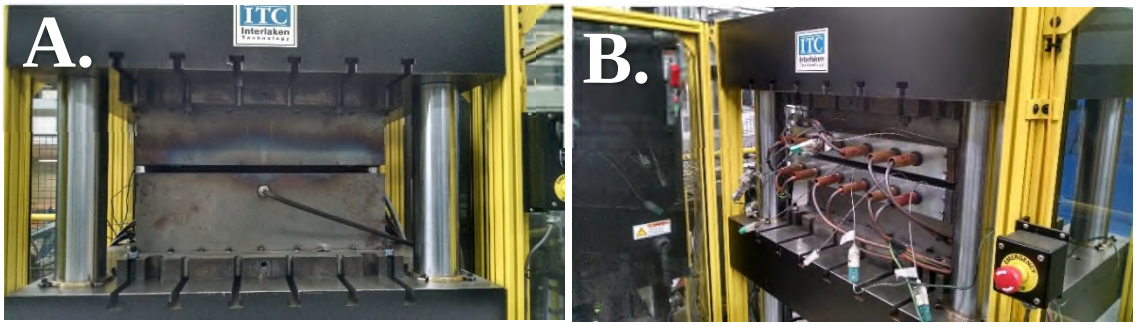

Fig.29. a) Tool loaded in press, b) reverse of tool showing heaters and thermocouples.

The tool was loaded into the press, clamping pressure on the tool, and application of gas pressure were controlled by unitest software, operating in gas pressure control rather than strain rate control. The tool was heated to the desired test temperature and allowed to stabilise fully before testing, samples were then loaded into the tool and the tool closed causing some warm deformation of the sample sheet. Sheets were allowed to preheat for

the required time, at which point the set pressure of the test was applied by building up pressure behind a valve and subjected the samples to an “instant” pressure rather than a ramped build up. A constant pressure was then maintained and tests were run with a total cycle time of five minutes inclusive of preheat to assess the industrial suitability. After five minutes the pressure was released, the tool unclamped and the samples air cooled.

### *3.4.2. Results*

Initial tests were conducted with heating and pressure profiles established during previous testing detailed in submissions four and five. These profiles were then varied depending upon the result of the test based on knowledge gained during previous tests. Tests on 1.2 mm and 2.0 mm AA7020 were conducted using the best forming conditions established for the 1.6 mm sheet. Details of all test conditions and outcome of tests are summarised in table.12.

Table.12. Matrix of testing conducted on Interlaken press.

| Sample | Material | Preheat (mins) | Pressure (Mpa) | Ramp (Mpa/s) | Temperature (°C) | Hold (mins) | Clamp (kn) | Lubrication | Blocks | Outcome |
|---|---|---|---|---|---|---|---|---|---|---|
| 1 | 7020 | 3 | 0.9 | 0.1 | 530 | 2 | 200 | Graphite | Both | Failure |
| 2 | 7020 | 3 | 0.45 | 0.1 | 530 | 2 | 200 | Graphite | Both | Failure |
| 3 | 7020 | 3 | 0.45 | 0.1 | 500 | 2 | 200 | Graphite | Both | Failure |
| 4 | 7020 | 3 | 0.45 | 0.1 | 500 | 2 | 200 | Magnesia | Both | Failure |
| 5 | 7020 | 3 | 0.9 | 0.1 | 500 | 2 | 200 | Magnesia | Both | Failure |
| 6 | 7020 | 3 | 0.9 | 0.1 | 500 | 2 | 200 | Magnesia | Both | Failure |
| 7 | V3CN | 3 | 0.9 | 0.1 | 500 | 2 | 200 | Magnesia | Both | Failure |
| 8 | V3CN | 3 | 0.6 | 0.1 | 500 | 2 | 200 | Magnesia | Both | Failure |
| 9 | V3CN | 3 | 0.9 | 0.1 | 500 | 2 | 200 | Magnesia | Both | Failure |
| 10 | V3CN | 3 | 0.9 | 0.1 | 500 | 2 | 150 | Magnesia | Both | Failure |
| 11 | V3CN | 3 | 0.9 | 0.1 | 500 | 2 | 120 | Magnesia | Both | Failure |
| 12 | V3CN | 3 | 0.9 | 0.1 | 500 | 2 | 140 | Magnesia | Both | Failure |
| 13 | 7020 | 3 | 0.9 | 0.1 | 500 | 2 | 150 | Magnesia | Smaller | Failure |
| 14 | V3CN | 3 | 0.9 | 0.1 | 500 | 2 | 150 | Magnesia | Smaller | Failure |
| 15 | 7020 | 3 | 1.1 | 0.1 | 500 | 3 | 150 | Magnesia | Smaller | Failure |
| 16 | 7020 | 3 | 1.1 | 0.1 | 500 | 2 | 150 | Magnesia | Smaller | Failure |
| 17 | 7020 | 3 | 0.9 | 0.1 | 500 | 3 | 170 | Magnesia | Smaller | Failure |
| 18 | V3CN | 3 | 0.9 | 0.1 | 500 | 3 | 170 | Magnesia | Smaller | Failure |
| 19 | 7020 | 3 | 0.9 | 0.1 | 500 | 3 | 170 | Magnesia | Smaller | Failure |
| 20 | V3CN | 3 | 0.9 | 0.1 | 500 | 3 | 150 | Magnesia | Smaller | Failure |
| 21 | 5083 | 3 | 0.9 | 0.1 | 500 | 3 | 150 | Magnesia | Smaller | Failure |
| 22 | 7020 | 3 | 0.9 | 0.1 | 500 | 3 | 150 | Magnesia | None | Failure |
| 23 | V3CN | 3 | 0.9 | 0.1 | 500 | 3 | 150 | Magnesia | None | **Formed** |
| 24 | 7020 | 3 | 0.9 | 0.1 | 500 | 3 | 150 | Magnesia | None | Failure |
| 25 | 7020 | 3 | 0.9 | 0.1 | 500 | 3 | 150 | Magnesia | Both | Failure |
| 26 | 7020 | 3 | 0.9 | 0.3 | 500 | 3 | 150 | Magnesia | Both | Failure |
| 27 | V3CN | 3 | 0.9 | 0.3 | 500 | 3 | 150 | Magnesia | Both | Failure |
| 28 | 7020 1.2 | 3 | 0.9 | 0.1 | 500 | 3 | 150 | Magnesia | Both | Failure |
| 29 | 7020 2.0 | 3 | 0.9 | 0.1 | 500 | 3 | 150 | Magnesia | Both | Failure |
| 30 | 7020 1.2 | 3 | 0.9 | 0.1 | 500 | 3 | 150 | Magnesia | Smaller | Failure |
| 31 | 7020 2.0 | 3 | 0.9 | 0.1 | 500 | 3 | 150 | Magnesia | Smaller | No Failure - Unformed |
| 32 | V3CN | 0.5 | 0.9 | 0.1 | 500 | 3 | 150 | Magnesia | Smaller | Failure |
| 33 | 7020 | 0.5 | 0.9 | 0.1 | 500 | 3 | 150 | Magnesia | Smaller | Failure |
| 34 | 7020 1.2 | 3 | 1.1 | 0.1 | 500 | 3 | 150 | Magnesia | Smaller | Failure |
| 35 | 7020 2.0 | 3 | 1.4 | 0.1 | 500 | 3 | 200 | Magnesia | Smaller | Failure |
| 36 | 7020 1.2 | 3 | 0.9 | 0.1 | 500 | 3 | 150 | Magnesia | None | Failure |
| 37 | 7020 2.0 | 3 | 0.9 | 0.1 | 500 | 3 | 150 | Magnesia | None | No Failure - Unformed |
| 38 | 7020 | 0.5 | 0.9 | 0.1 | 500 | 3 | 150 | Magnesia | None | No Failure - Unformed |
| 39 | V3CN | 0.5 | 0.9 | 0.1 | 500 | 3 | 150 | Magnesia | None | No Failure - Unformed |

The best performing samples were selected alongside samples of other materials in the same condition for direct comparison. A minitest FH4100 Hall Effect ultrasonic tester was used to measure material thinning in selected areas of interest, detailed in fig.30. Average values were taken from each area.

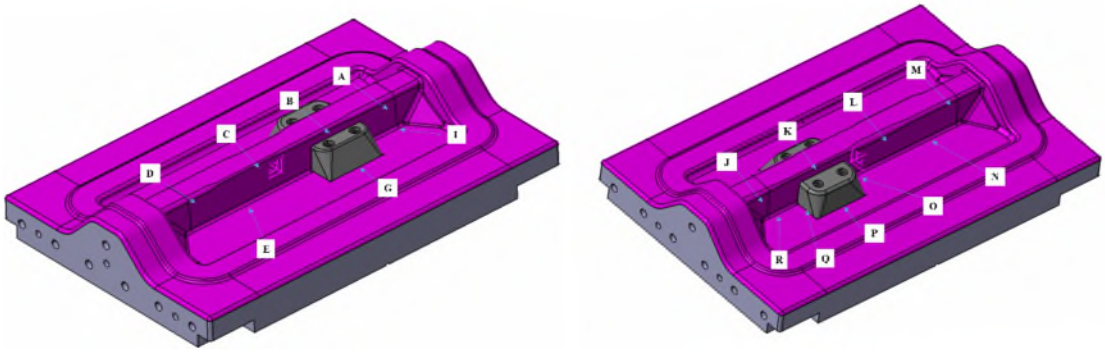


Fig.30. Tooling showing labelled areas for measurement of thinning.

The measured thinning of parts was used to calculate the equivalent strain in the parts resulting from forming. This was the same metric which was used to asses parts formed during testing at SUSA. Results are shown in fig.33, 34 and 35 showing equivalent strains for geometries with both blocks, one smaller block and with no blocks respectively. All strains shown in fig.33 and 34 are of failed parts, with fig.35 showing strains from both fully formed and partially formed parts.

Examples of the different failures mechanisms between the two materials are shown in fig.31 a and b. The area of material flow around the clamp line necessary to successfully form parts is shown in fig.32 a and b.

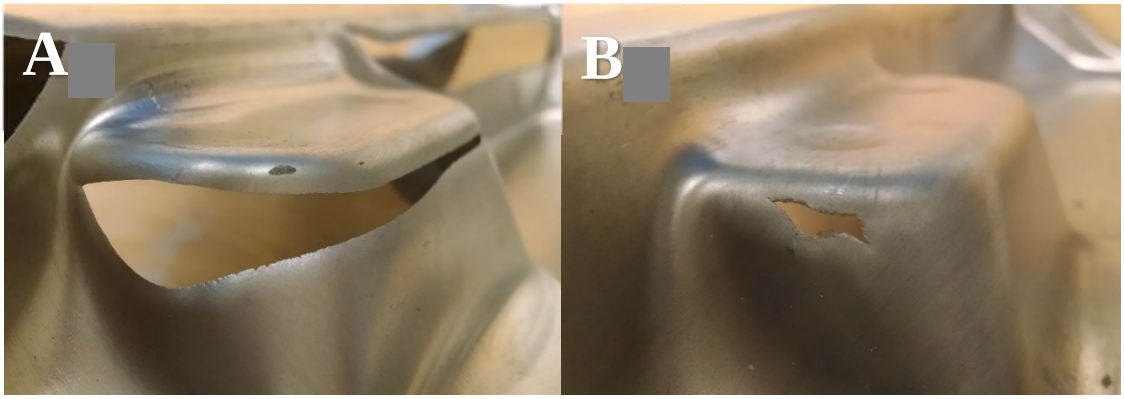

Fig.31.a) Thinning failure seen in AA7020, b) Tearing failure seen in V3CN, tested at 500°C.

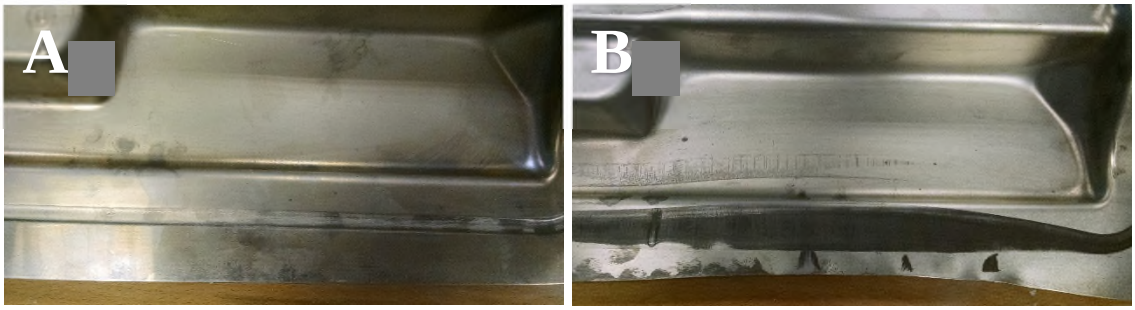

Fig.32. V3CN around clamp line showing a) no draw in, b) material draw in from clamp area.

Fig.33 shows the resulting parts from two tests conducted with the simple tophat section without additional blocks. The failed AA7020 part is shown in fig.33a and the fully formed V3CN part shown in fig.33b. The AA7020 part failed along its full length, as

with cone testing showing the materials inability to form around male radii's without undergoing a level of strain before contact.


Fig.33.a) AA7020 failed part, b) successful forming in V3CN, formed at 500°C and 0.9 MPa.

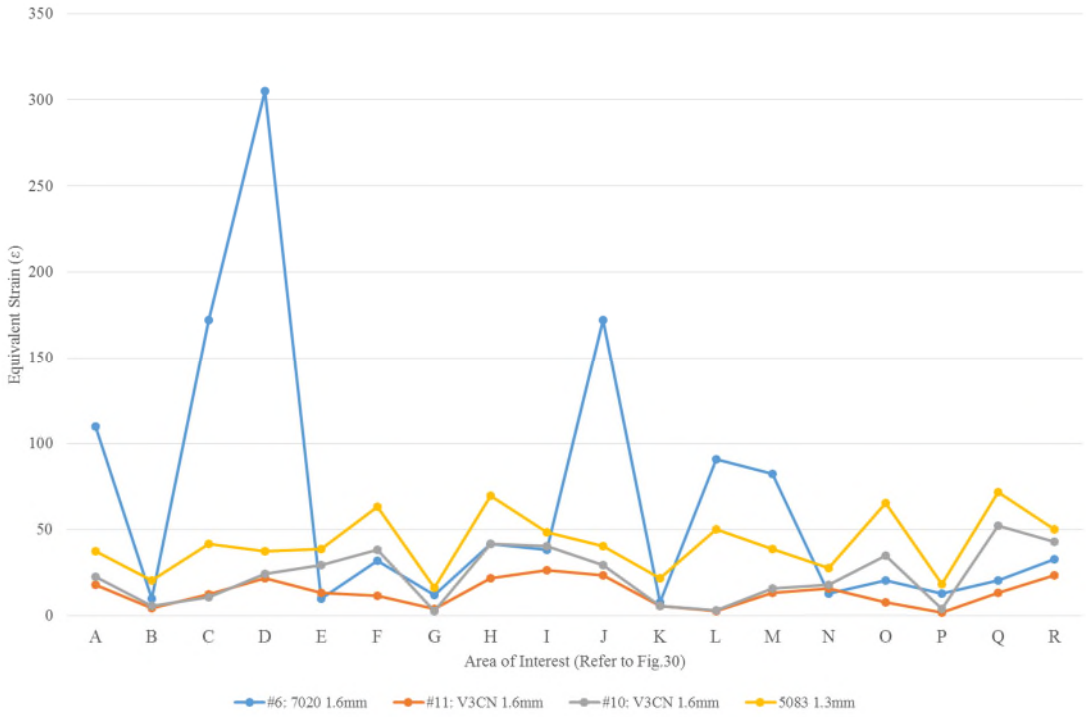


Fig.34. Equivalent strain in areas of interest with both block geometry at 500°C and 0.9 MPa.

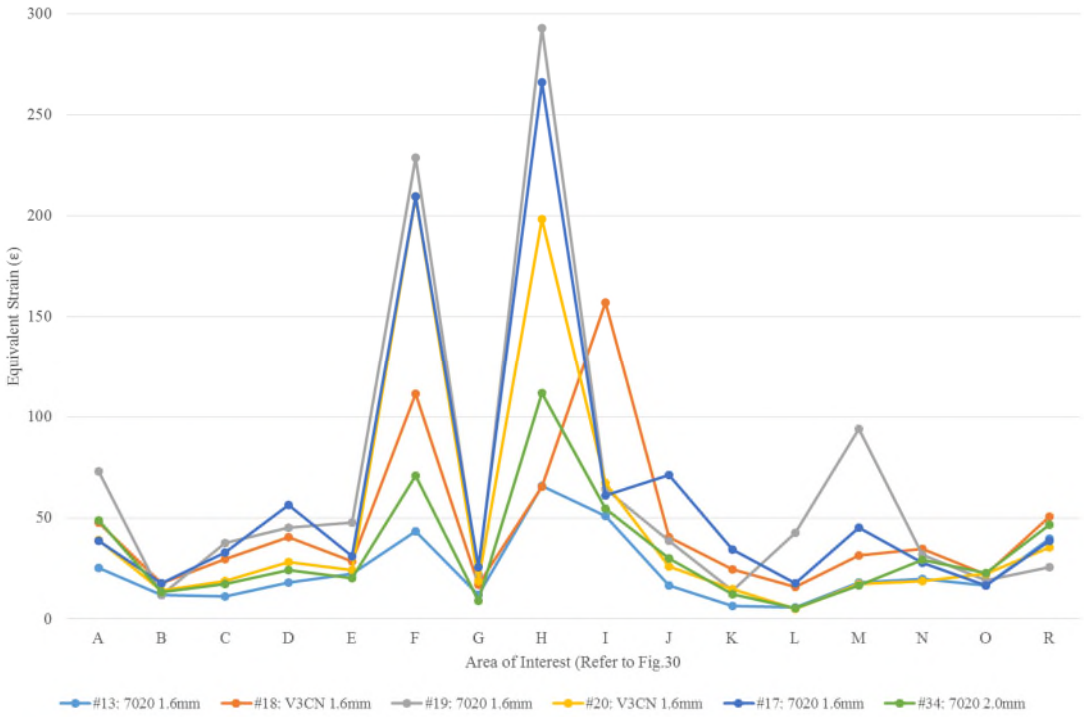


Fig.35. Equivalent strain in areas of interest with one block geometry at 500°C and 0.9 MPa.

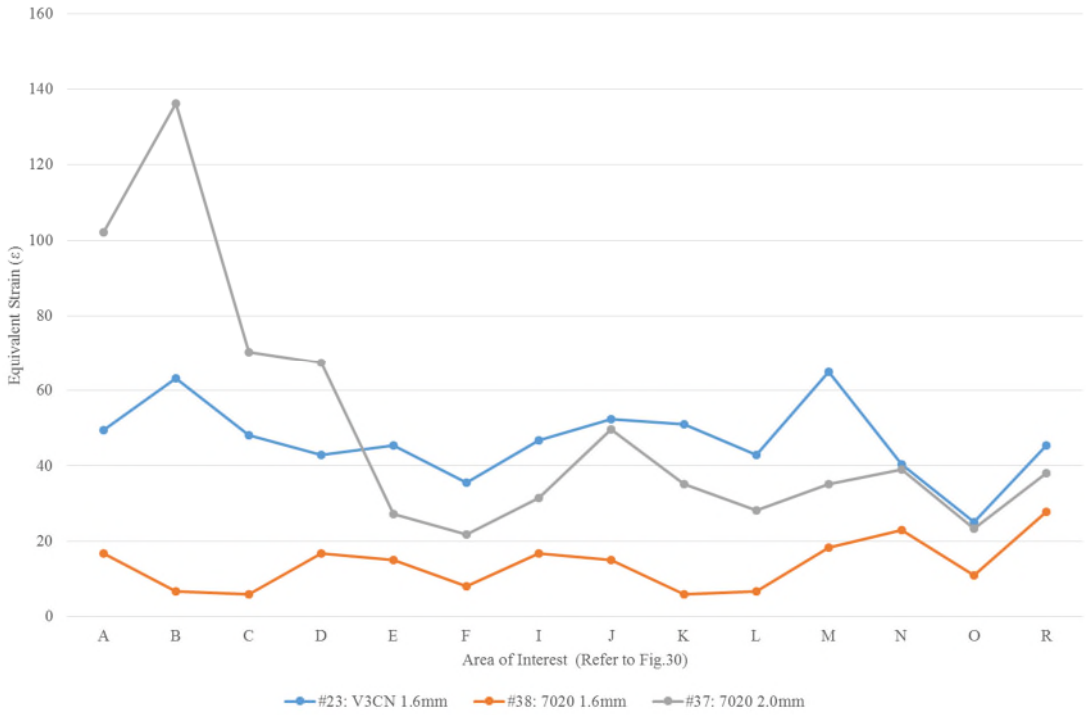


Fig.36. Equivalent strain in areas of interest with no block geometry at 500°C and 0.9 MPa.

### *3.4.3. Discussion*

A control sample was formed using AA5083 processed for SPF forming. This alloy was used to assess to how a true SPF alloy would perform with this geometry compared to the non SPF alloys AA7020 and V3CN. The AA5083 formed the part without failure, however the tight radii's at the bottom of the part were not well formed suggesting that the sample needed more time or forming at a higher pressure. The part was formed using 200 kN of clamping force which did not allow for any material to flow in from around the clamp line, as is typical of an SPF forming process. Graphite only was used as the lubricant for this sample.

Initial tests of the V3CN and AA7020 both used these same conditions which led to failed parts. As with testing at SUSA the lubrication was then modified to include magnesium hydroxide in areas of contact with male radii. This still led to failed parts, as did a

reduction in forming pressure. To counteract the thinning within the samples the clamping force was reduced to allow for some material to draw in from the clamp area as show in fig.32. This is not typical of a true SPF process but it is employed industrially to form complex geometries where excess thinning is an issue. This was critical to successfully forming parts as without this extra material draw in parts were seen to fail early during the forming process.

Forming with a combination of 500°C temperature, 130 Psi forming pressure, 150 kN clamping force and combination of graphite and magnesium hydroxide offered the best performance. Holding time at pressure was increased from two to three minutes to see whether parts could form a tighter radii, instead of using higher pressures which were seen to cause premature failures.

The equivalent strains for all samples with the geometry employing both blocks shown in fig.34 equivalent strains except in areas of material failure were under 100% showing less than 50% thinning in any area. The equivalent strains of both AA7020 and V3CN were lower than that of the AA5083, however the AA5083 was a more fully formed part with tighter radii compared to the other alloys, the lesser amount of actual forming would account for the lower values for equivalent strain. The 1.6 mm AA7020 material experienced significantly higher strains in excess of 300% in area “D”. This was in a failed region and so the forming had been unsuccessful despite the high strain.

Previous testing at SUSA had shown that the material requires strain in excess of 100% before contact with male radii to allow for grain refinement possibly by dynamic recrystallization. Measurement across the top section of the tool where the sheet first contacts showed equivalent strains of under 10% showing that the AA7020 has not had enough time to sufficiently refine the microstructure accounting for the failures. The

V3CN had previously shown a limit of 100% strain, and as such performed better in this geometry where lower strains were experienced.

With the larger block removed to simplify part geometry equivalent strains were again all observed to be under 100% other than in areas of material failure shown in fig.35. The possible reason for the AA7020 materials poor performance was the fact that the material does not undergo sufficient strain before contact with a male radius to allow for successful forming. The 2.0 mm thickness AA7020 performed better, not failing during forming, but due to the material thickness it was not fully formed at the forming pressure of 130 Psi, with an increase in forming pressure to 150 Psi samples were seen to fail.

Testing with no blocks in place to give a simpler "top-hat" section as shown in fig.36 again showed the AA7020s inability to form the part, with failures along the whole part not allowing for measurements of strain to be taken. When looking at fig.36 at the strains experienced within the successfully formed V3CN part, strain peaked at 68%, this again shows that the geometry is unsuitable for the AA7020 material.

When looking at failed areas of parts with the single block geometry in fig.32a and b there is a clear difference in the mechanism of failure between the two alloys. The AA7020 shows obvious localised necking within regions of failure which causes the material to fail at a critical point of thinning. The V3CN shows less evidence of this necking, instead suffering from "tearing" failures which are more typical of coalescence of cavities which are propagated by the $Al_3Ni$ particles present within the alloy, which cause faster recrystallization and explain the alloys better performance in regions of lower strain. AA7020 was again shown to fail when contacting male radii before experiencing a minimum of 100% strain.

### *3.4.4. Conclusions*

Testing corroborated results from previous testing at SUSA, showing that varied lubrication in the form of magnesium hydroxide is required for both alloys when forming across male radii. This alternative to graphite increased the coefficient of friction and halts material slip which leads to localised thinning.

AA7020 1.6 mm was again shown to fail when contacting male radii before experiencing a minimum of 100% strain, strengthening the hypothesis of possible dynamic recrystallization of the alloy during forming. Thicker 2.0 mm did not fail but experienced significant thinning, suggesting that thicker material could be used in applications where lower strains are experienced.

V3CN performed better across most test conditions, due to the lower strains experienced during the forming of the part. This was in agreement with testing at SUSA that had shown a limit of around 100% strain before failure of the alloy.

## *3.5. Post Forming Properties Hardness & Tensile Testing (Submissions 2,3,4)*

### *3.5.1. Methodology*

Submission two dealt with the comparison of AA7020 and V3C by means of Vickers hardness testing. Tests were conducted to establish a suitable aging treatment after forming to meet the 300 MPa yield strength target set for the project. Testing was conducted to establish if a short aging treatment at higher temperatures would be suitable but the alloys did not respond well to this. A two stage treatment based around previous work elsewhere [72] and talks with industrial partners [73] of 90°C and 130°C for 8 and

18 hours was established as the optimum treatment for the alloys to achieve peak strength and hardness.

Hardness testing in submission three looked at the influence of reducing solution treatment time, (which mimics the heating cycle during forming) on material strength after aging to establish the shortest cycle time that could be used to still achieve peak strength. The influence of nickel additions within the V3C on the quench rate sensitivity of the alloys was investigated by using both water and air quenches after solution treatment. Tensile testing was conducted on AA7020 to establish a conversion value from hardness to yield strength but this was not possible with V3C due to a lack of experimental material.

Vickers hardness and tensile testing was then conducted on AA7020 and V3CN to compare the two materials and to establish a conversion for the V3CN between the two values. The hardness values were used to compare the V3C to the V3CN to look at the difference in strength after scale up of production. Vickers hardness was then used to establish the influence of a customer's paint bake cycle on material strength, which was used to modify the aging treatment to ensure a final strength after paint bake of 300 MPa yield.

Samples of alloys were subjected to various solutionization temperatures to mimic the heating achieved during a forming cycle for various times, followed by various aging cycles and finally by a simulated paint bake cycle detailed in fig.36. The details of sample treatments are detailed with results in the next section of this report.

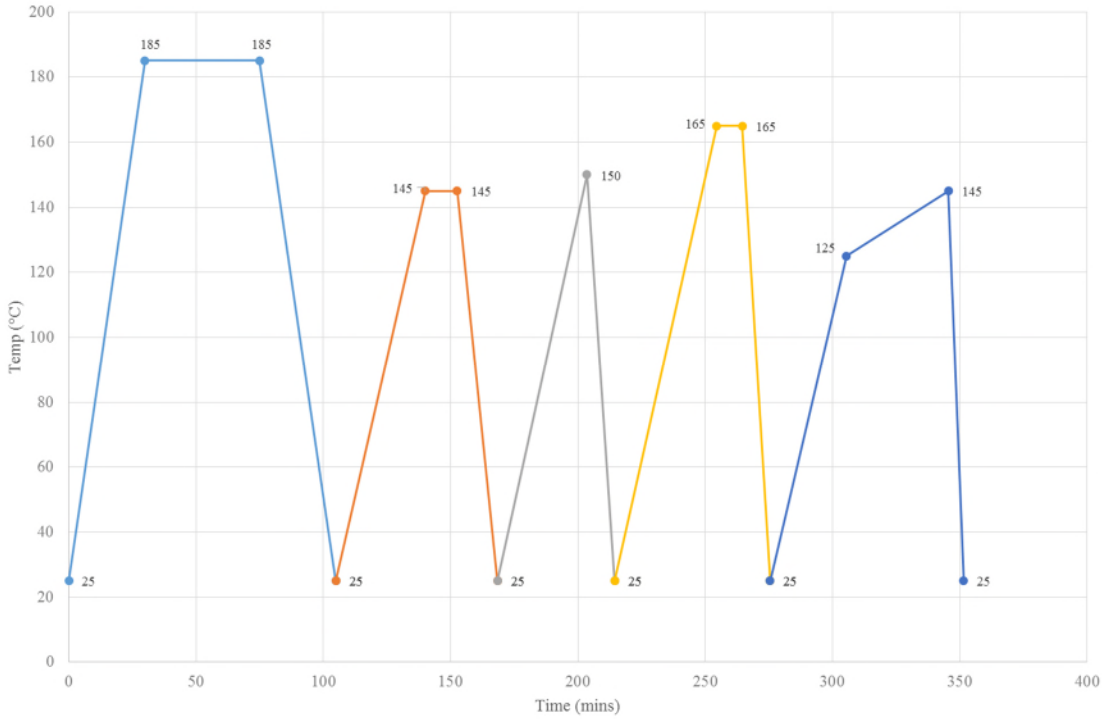


Fig.36. Simulated customer paint bake heat cycle temperatures in °C labelled.

After these heat treatments samples were prepared for hardness testing by sectioning, mounting in resin and then polished. Vickers hardness testing was conducted using a 10 kg mass with a ten second dwell time using a Buehler automatic hardness tester an average of nine indents of each sample was taken.

Samples for tensile testing were machined into tensile dogbones according to BSI standard ISO 6892-1 [74] the dimensions of which are shown in fig.37 all samples had a nominal thickness of 1.6 mm.

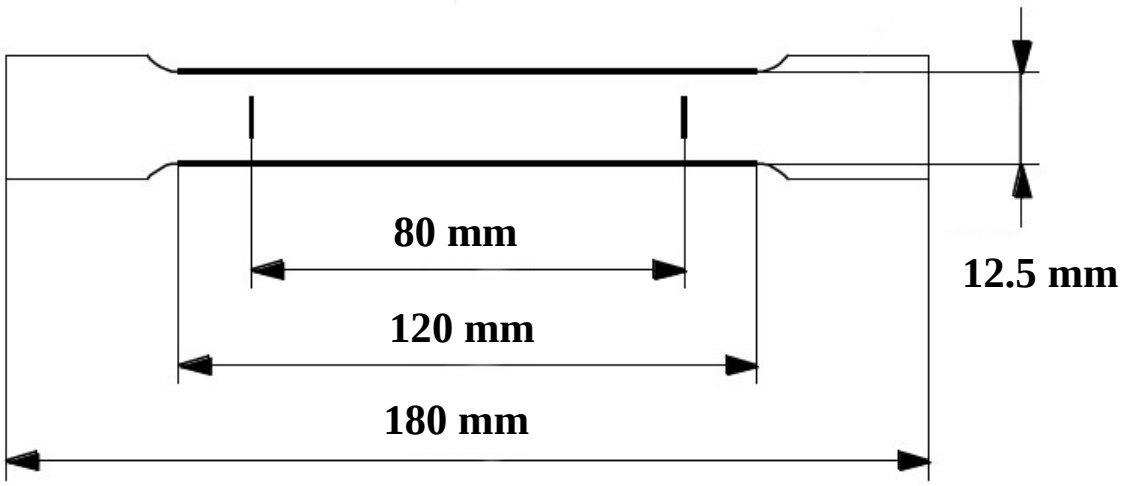


Fig.37. Tensile dogbone sample geometry.

Samples were then loaded into an INSTRON 6652 load frame equipped with a 100 kN load cell and 100 kN tensile grips, Instron Bluehill V.2.4 software was used to control the test profile. The frame was zeroed and the relevant test profile was run with a cross head speed of 13.5 mm/min. This was an established test profile used for yield strength testing and tests were repeated three times.

### *3.5.2. Results*

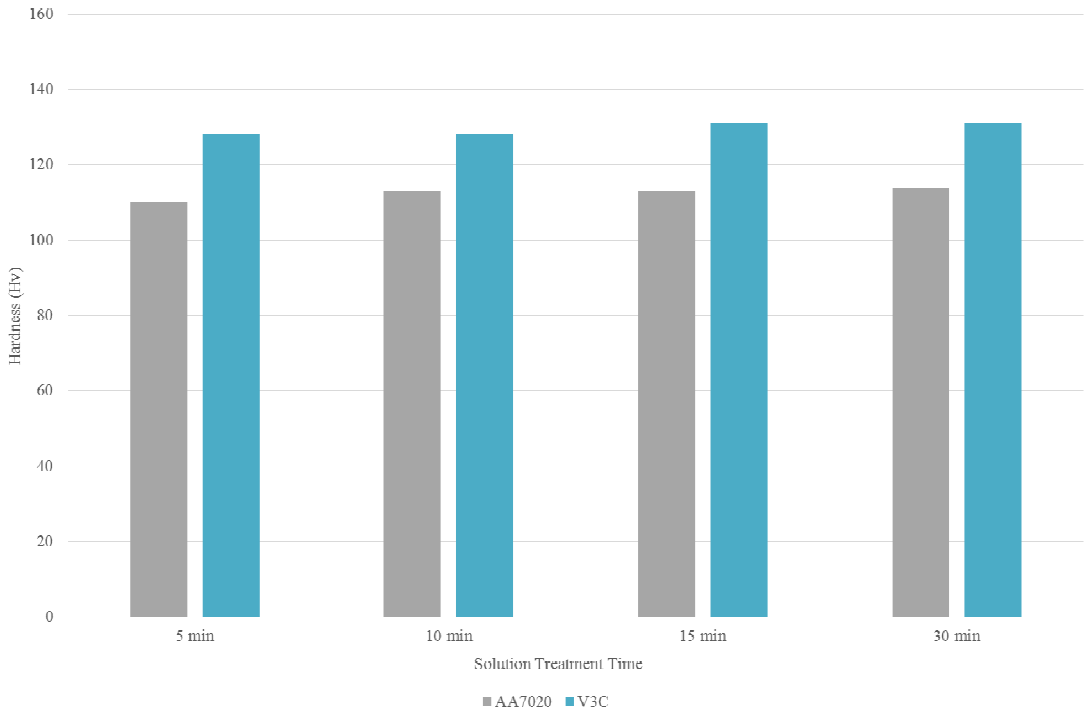


Fig.38. Hardness vs. solution treatment time at 500°C for AA7020 and V3C.

Initial tests to establish the shortest solutionization time to achieve peak hardness are shown in fig.38 with no difference observed between 30 minutes and 5 minutes solution treatment. Following this testing solution treatment times were further decreased to look at the influence of this decreased time, and to assess the feasibility of further reduced cycle times for an industrial process. The results of this testing are shown in fig.39.

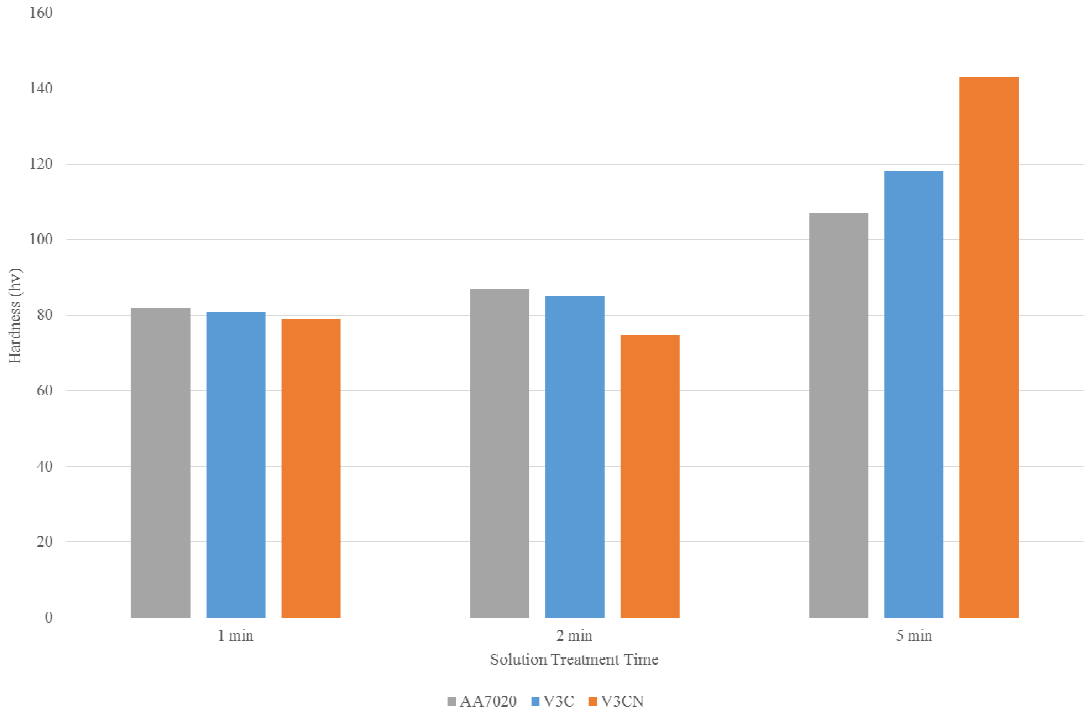


Fig.39. Hardness vs. solution treatment time at 500°C for AA7020, V3C and V3CN.

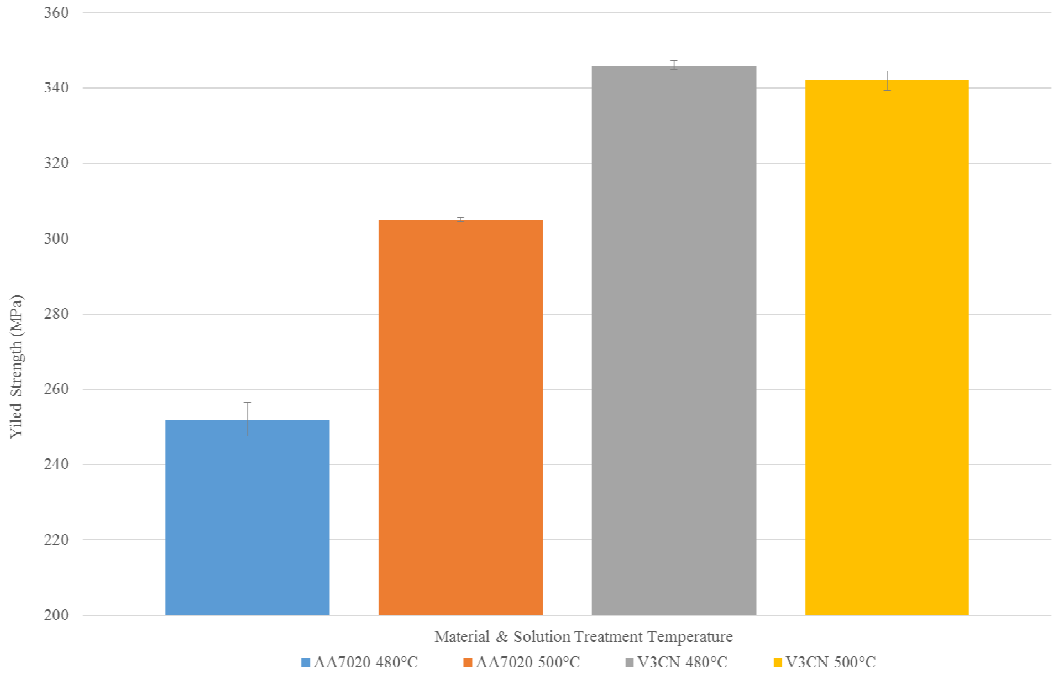


Fig.40. Yield strength vs five minute solution treatment temperature of AA7020 and V3CN.

The results of room temperature tensile testing to establish the material yield strength and the effect of solutionization temperature are shown in fig.40. The results of this testing

were compared with hardness testing under the same conditions to give a conversion value for later testing both at WMG and Superform.

A simulated customer paint bake cycle as detailed in fig.36 was applied to both alloys after the two stage aging treatment. The length of aging treatment was then varied as detailed in table 13 (customer age refers to the paint bake cycle) to look at the influence on final strength after the paint bake cycle, the results of which are shown in fig.41

Table.13. Heat treatment cycles after simulated paint bake before tensile testing.

| Sample | Solutionized | Pre-Age | Pre-Bake | Artifical Age | Customer Age |
|---|---|---|---|---|---|
| **A** | 15 min @ 500 °C (503°C) | 72 hrs @ RT | 24 hours @ 40 °C | 8 hours @ 90 °C + 18 hours @ 130 °C | None |
| **B** | 15 min @ 500 °C (503°C) | 72 hrs @ RT | 24 hours @ 40 °C | 8 hours @ 90 °C + 18 hours @ 130 °C | As detailed |
| **C** | 15 min @ 500 °C (503°C) | 72 hrs @ RT | 24 hours @ 40 °C | 8 hours @ 90 °C + 16 hours @ 130 °C | As detailed |
| **D** | 15 min @ 500 °C (503°C) | 72 hrs @ RT | 24 hours @ 40 °C | 8 hours @ 90 °C + 14 hours @ 130 °C | As detailed |
| **E** | 15 min @ 500 °C (503°C) | 72 hrs @ RT | 24 hours @ 40 °C | 8 hours @ 90 °C + 12 hours @ 130 °C | As detailed |
| **F** | 15 min @ 500 °C (503°C) | 72 hrs @ RT | 24 hours @ 40 °C | 8 hours @ 90 °C + 10 hours @ 130 °C | As detailed |

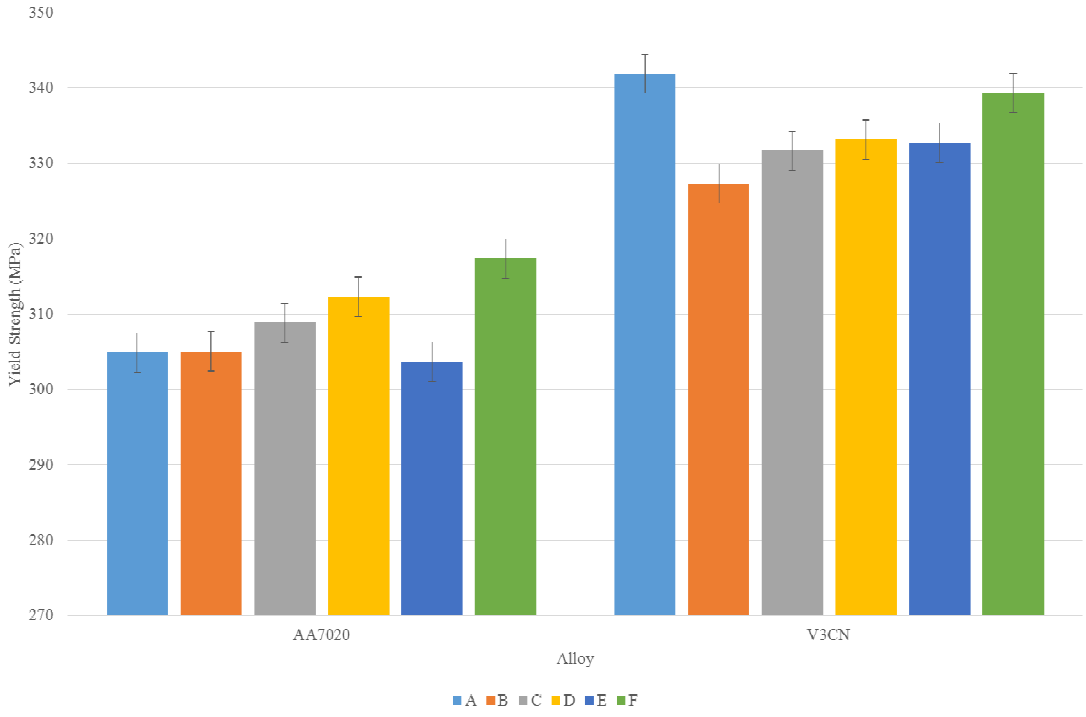


Fig.41. AA7020 and V3CN yield strength after paint bake and aging as detailed in table 13.

### *3.5.3. Discussion*

Initial testing identified the two stage 90°C for 8 hours and 130°C for 18 hours as the optimum artificial aging to achieve peak hardness in both alloys. Testing for varied amounts of solutionization time proved that both alloys could achieve peak hardness within the five minute target cycle time but if the solution treatment time was reduced further there was a detrimental effect on the final hardness values.

A peak yield strength of 305 MPa for the AA7020 alloy was observed after a 5 minute solution treatment at 500°C followed by the two stage aging treatment, whereas for the V3CN the peak yield strength of 346 MPa was achieved after 5 minutes at 480°C followed by the two stage treatment. The V3CN after solutionization at 500°C achieved a strength of 342 MPa yield, the alloy was observed to be stronger/harder than the AA7020 alloy under all conditions tested. Following testing conversion rates from hardness to yield strength were found to be 2.87:1 for AA7020 and 2.76: for V3CN.

Following simulated paint bake cycle tests the AA7020 showed slight improvement in strength with the shortest aging treatment of 8 hours at 90°C and 10 hours at 130°C achieving 317 MPa, suggesting that with the standard treatment and consequent paint bake the material is being slightly overaged leading to a slight reduction in strength. The alloy across all tests met the required 300 MPa yield target with the lowest strength being 303 MPa with the 8 hours at 90°C and 12 hours at 130°C aging treatment.

The V3CN saw a peak yield strength of 342 MPa following the standard two stage aging treatment with no paint bake cycle, all samples with the paint bake cycle applied showed decreased strength. This suggests over aging of the alloy with the paint bake cycle, this was substantiated by the recovery of yield strength with reduction of aging time, the alloy

achieving a yield strength of 339 MPa with the shortest 8 hours at 90°C and 10 hours at 130°C aging treatment and subsequent paint bake.

### *3.5.4. Conclusion*

Both AA7020 and V3CN alloys can achieve the required 300 MPa yield strength target after a 5 minute solutionization treatment to simulate the heating cycle during forming. This means that both alloys would meet the strength and cycle time criteria for the project, their commercial viability then depending upon the alloy formability.

A 1.6wt% nickel addition in V3C alloy was shown to significantly improve the strength and hardness of the alloy, with testing in all conditions offering greater strength than AA7020. Unlike the formability of the material the influence of scaling up production in the V3CN did not detrimentally effect the alloy strength, instead further increasing the strength.

The addition of nickel caused a slight increase in quench rate sensitivity from 3% to 5% in comparison with the AA7020 alloy. This increase would not be of consequence commercially as the V3CN alloy is well in excess of the 300 MPa yield strength requirement even when air quenched.

Both alloys achieve the required final 300 MPa yield strength target after a simulated customer paint bake heat treatment when a modified two stage aging treatment with a decreased duration of the second stage is employed. This reduction in aging duration helps to prevent over aging of the alloy during customer processing of the alloys.

### *3.6. SEM/EBSD Analysis (Submissions 2,3,4)*

#### *3.6.1. Methodology*

EBSD analysis to identify the grain structure evolution within AA7020, V3C and V3CN during forming was carried out using a Carl Zeiss Gemini FEGSEM with Nordilys EBSD and Oxford Aztec software. Settings were optimised for each test and scans were run for an average of 30 minutes with an average step size of 0.5µm. An aperture size of 240µm with an accelerating voltage of 20 kV and a stage tilt of 70° was used across all tests. For BSE and EDX analysis samples were not tilted and a 30µm aperture was used again with an accelerating voltage of 20 kV.

Samples of alloys were mounted in the as received condition or after being subjected to the relevant heat treatment and test conditions (detailed in results section). Samples were then sectioned, and mounted in Konductomet resin cured at 250°C for 3minutes at 10 bar pressure to produce a conductive sample. Following this samples were polished using a three step polishing regime which was established during this research and has proved suitable for various aluminium alloys, the polishing regime is detailed in table 14.

Table.14. EBSD sample preparation polishing regime.

| Step | Pad | Lubricant | Pressure (Psi) | Speed (Rpm) | Direction | Time |
|---|---|---|---|---|---|---|
| **1A** | 1200 Grit | Water | 18 | 250 | Complimentary | 1 minute |
| **1B** | 1200 Grit | Water | 18 | 250 | Complimentary | 10 seconds |
| **2** | Trident | 3µm Diamond Solution | 19 | 125 | Complimentary | 3.5 minutes |
| **3** | Chemomet | 0.05µm Mastermet Solution | 19 | 150 | Contra | 1.5 minutes (Final 30s with water) |

Samples were taken from various areas of deformed samples as well as from as received material with no processing. This allowed the initial grain structure to be compared to the

final grain structure in areas with and without deformation. BSE imaging was used to look at the distribution of secondary particles within the alloys, EDX was employed to verify chemical composition of the alloys and secondary particles, and EBSD was used to identify the various phases within the alloys as well as the alignment of the grain structure and any physical changes due to heating and or forming. This helped to assess the influence of the nickel additions in V3C and the effect of production differences in V3CN.

Samples of V3CN in the cast, homogenised, hot rolled and cold rolled conditions were imaged to help understand the difference in forming performance and strength between V3C and V3CN. Direct comparisons of the two alloys were made in the cold rolled condition, samples of V3CN were subjected to the same processing as V3C to help assess differences in microstructure due to the different processing route. GIMP open source image processing software was used to select and quantify cavitation across the surface of the materials [75]. ImageJ image processing and analysis software was used to convert image to a threshold black and white image and conduct particle size analysis [76].

### *3.6.2. Results*

EBSD scans were conducted on the AA7020 in the as received condition, then at the shoulder after forming where no deformation occurred shown in fig.43.a and b. The material after forming near to the point of failure, and the areas of cavitation within this region are shown in fig.44.a and b. These conditions allow the microstructural evolution to be evaluated and to observe any evidence of possible dynamic recrystallization within the material. The IPF legend for all images is shown in fig.42 showing the colours corresponding to the orientation of grains. Unless stated, rolling direction and direction of forming run across the page as images are presented.


Fig.42. IPF shading legend for all EBSD scans.

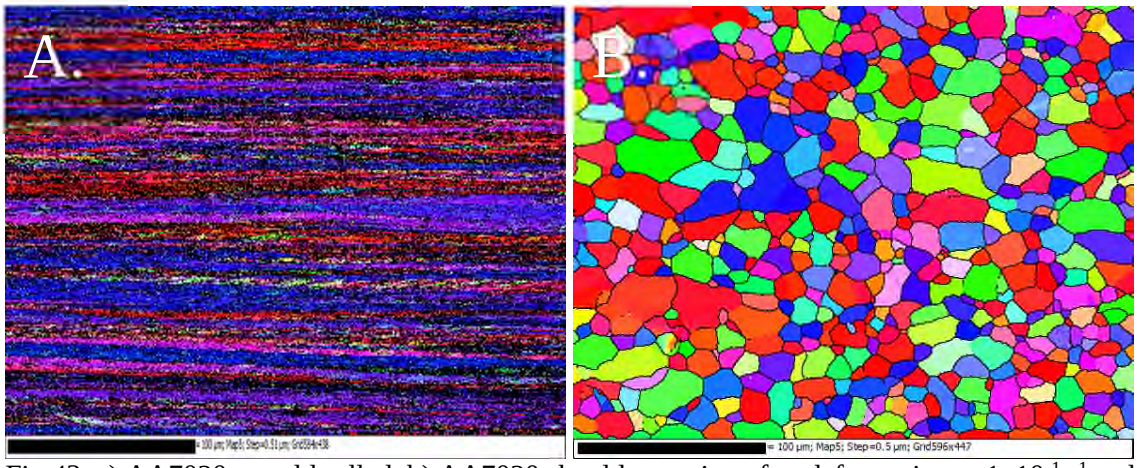


Fig.43. a) AA7020 as cold rolled, b) AA7020 shoulder section after deformation at $1x10^{-1}s^{-1}$ and 500°C.

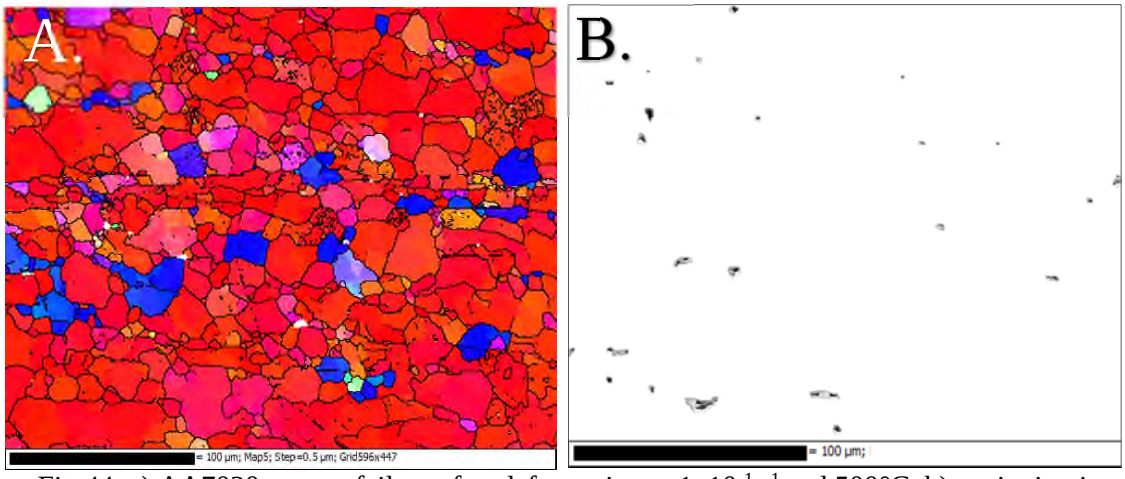


Fig.44. a) AA7020 near to failure after deformation at $1x10^{-1}s^{-1}$ and 500°C, b) cavitation in same region.

EBSD scans were conducted on the V3C alloy under identical conditions to the AA7020 to give a direct comparison between the two alloys. Fig.45.a and b show the alloy in in the as received condition, then at the shoulder after forming where no deformation has occurred. The alloy after forming near to the point of failure, and the areas of cavitation within this region are shown in fig.46.a and b.

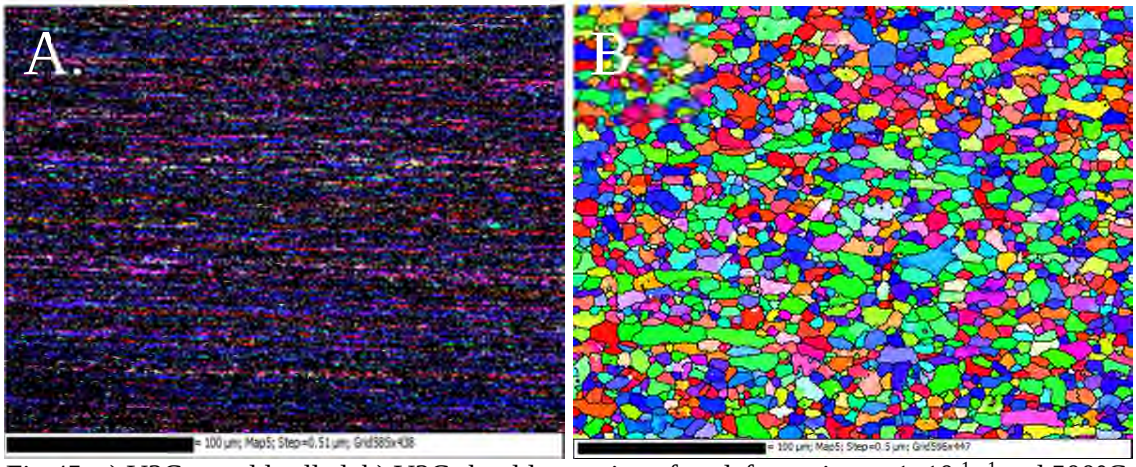

Fig.45. a) V3C as cold rolled, b) V3C shoulder section after deformation at $1x10^{-1}s^{-1}$ and 500°C.

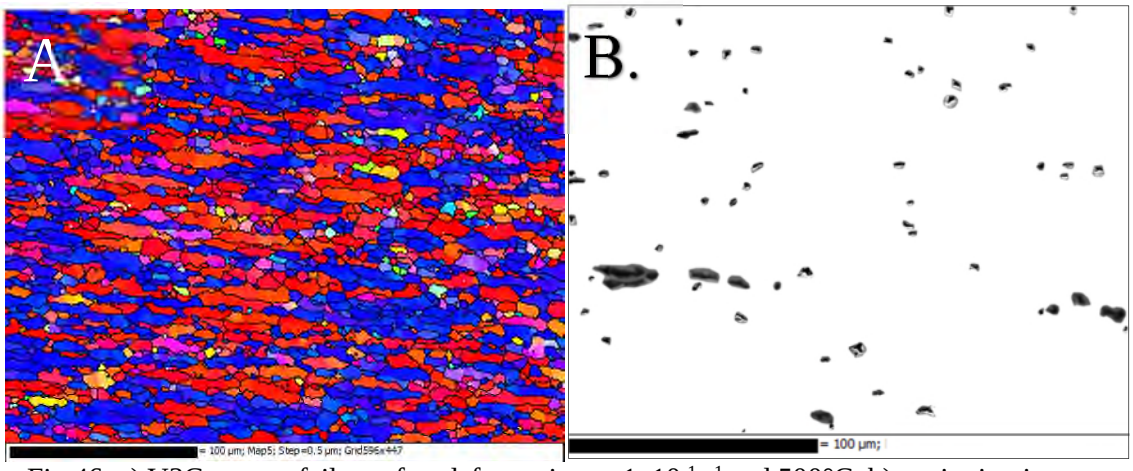

Fig.46. a) V3C near to failure after deformation at $1x10^{-1}s^{-1}$ and 500°C, b) cavitation in same region.

As with the two previous alloys, the V3CN was imaged in the as received condition, then at the shoulder after forming where no deformation has occurred shown in fig.47.a and b. The alloy after forming near to the point of failure, and the areas of cavitation within this region are shown in fig.48.a and b.

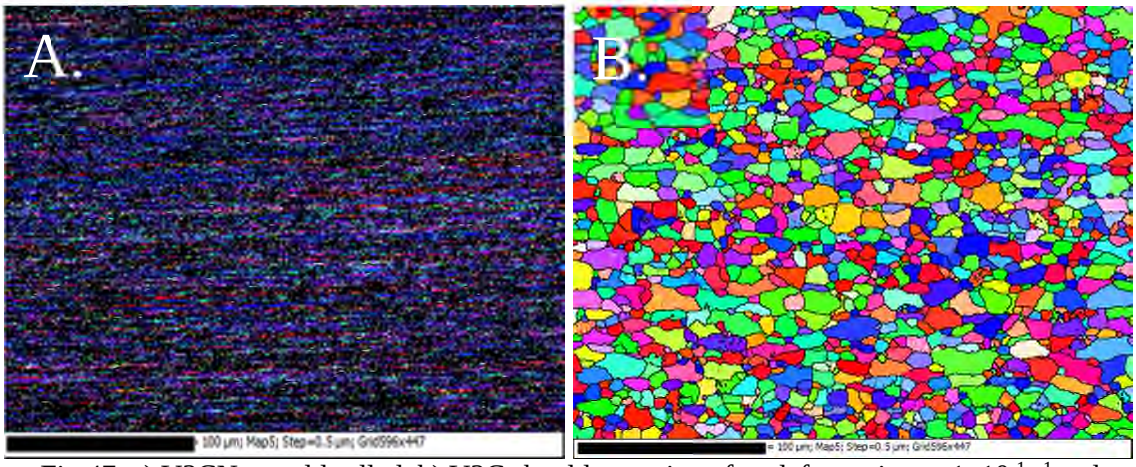


Fig.47. a) V3CN as cold rolled, b) V3C shoulder section after deformation at $1x10^{-1}s^{-1}$ and 500°C.

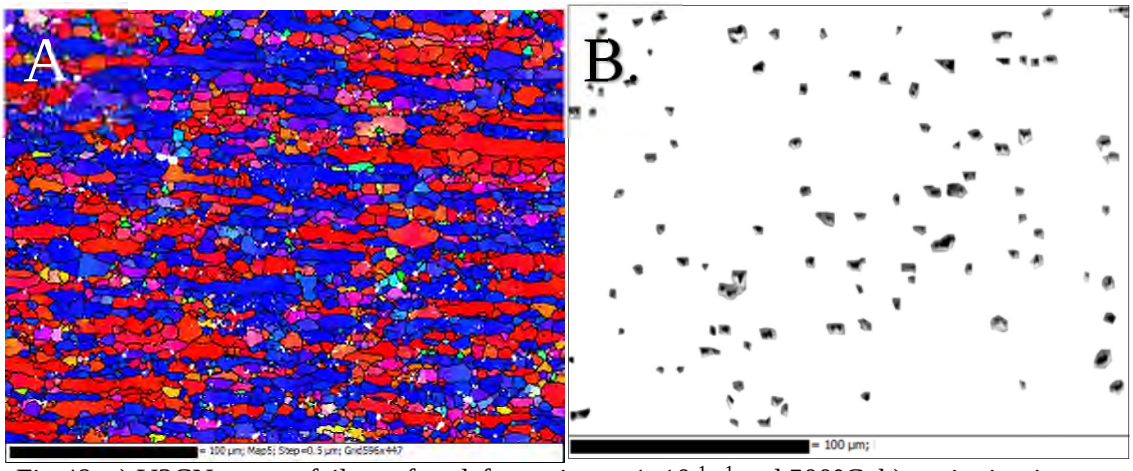


Fig.48. a) V3CN near to failure after deformation at $1x10^{-1}s^{-1}$ and 500°C, b) cavitation in same region.

Work in portfolio submission five showed the difference in $Al_3Ni$ particle size and distribution within the V3C and V3CN alloys using BSE imaging. Coarser particles were observed within the V3CN alloy, the chemical composition of these particles being confirmed by EDX. The main difference between the two alloys being the difference in solidification rates due to the difference in cast sizes, and to a lesser extent the difference in homogenisation treatments. Average grain sizes and levels of cavitation within failed areas are listed in table 15.

Table.15. Average grain size and levels of cavitation in all alloys after forming at $1x10^{-1}s^{-1}$ and 500°C .

| | Average Grain Size | | |
|---|---|---|---|
| **Alloy** | **Shoulder (µm)** | **Gauge (µm)** | **Cavitation (%)** |
| **7020** | 11 | 12 | 1.5 |
| **V3C** | 6 | 9 | 3.6 |
| **V3CN** | 8 | 10 | 8.5 |

To better understand the differences between the V3C and V3CN materials cast samples of V3CN were subjected to the two stage 520°C for 24 hours + 550°C for 2 hours homogenisation treatment as used with the V3C as well as the single stage 550°C for 24 hours used with the V3CN. EBSD scans of the V3CN in these conditions were conducted and shown in fig.49. a and b to illustrate the difference in grain size depending upon homogenisation treatment.

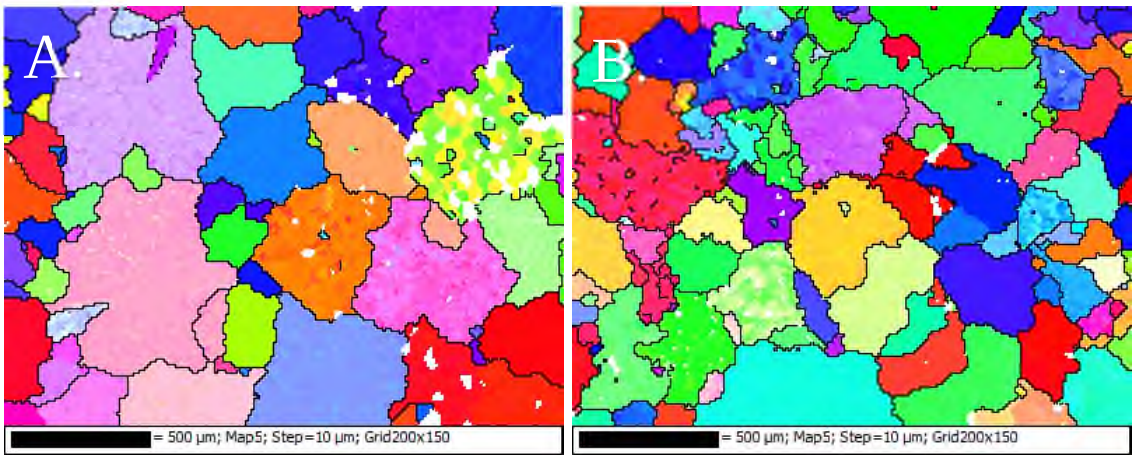


Fig.49. EBSD scans of V3CN after a) 550°C for 24 hours and b) 520°C for 24hours + 550°C for 2hours.

With grain size established by EBSD imaging SE imaging and EDX were employed to image the surface topography and to confirm the chemical composition. The SE images are shown in fig.50. a and b and the EDX scans of nickel containing areas shown in fig.51. a and b.

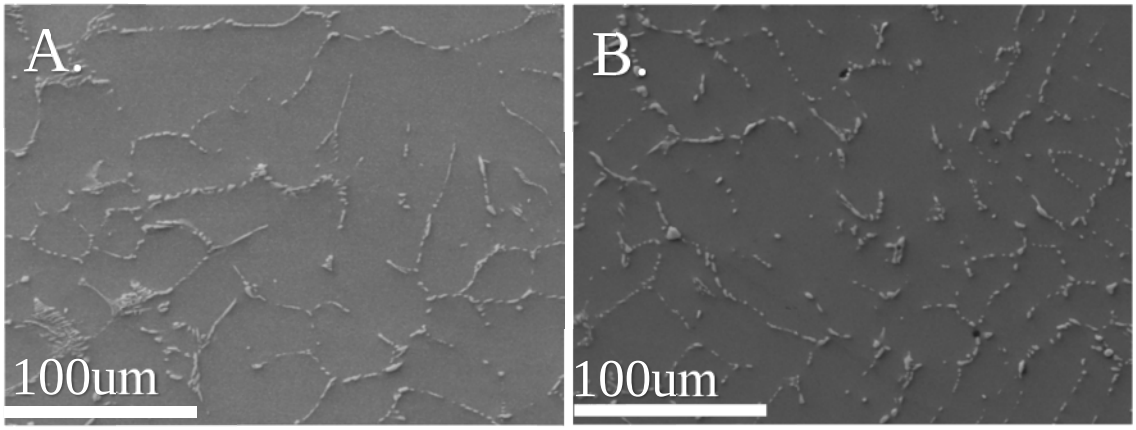


Fig.50. SE imaging of V3CN after homogenisation treatment of a) 550°C for 24 hours and b) 520°C for 24hours + 550°C for 2hours.

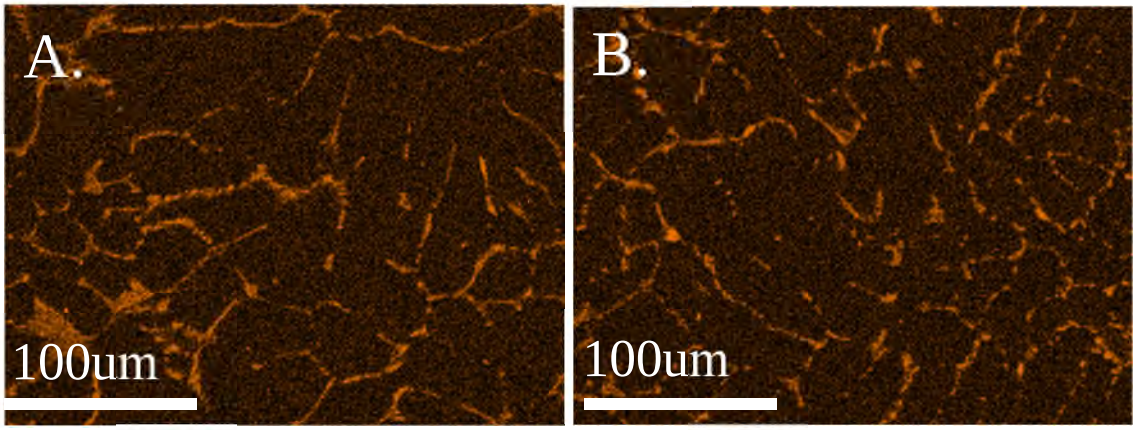


Fig.51. EDX of V3CN after homogenisation treatment of a) 550°C for 24 hours and b) 520°C for 24hours + 550°C for 2hours.

BSE imaging was used to produce high contrast images to identify nickel containing particles within the V3C and V3CN and quantify the difference in size and distribution of these particles. EDX analysis was used to confirm the chemistry of said particles, BSE images and particle size distribution of V3C are shown in fig.52 and corresponding images of V3CN in fig.53. $MgZn_2$ particles are also present within the alloy and shown within the BSE images, to effectively remove these particles from the size analysis EDX analysis and the exclusion any partciles sub 1.4 μm were used as filters, studies have reported the size of MgZn2 particles within AA7020 not exceeding this size [77].

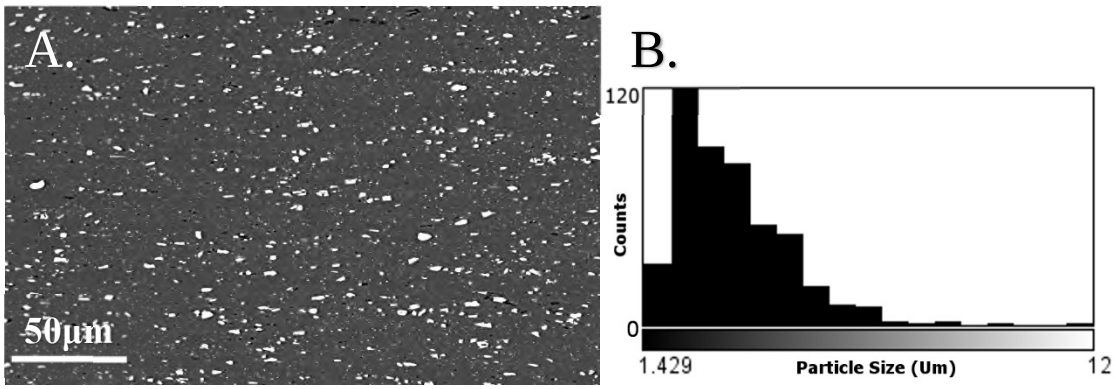

Fig.52. a) BSE image of as rolled V3C b) particle size distribution.

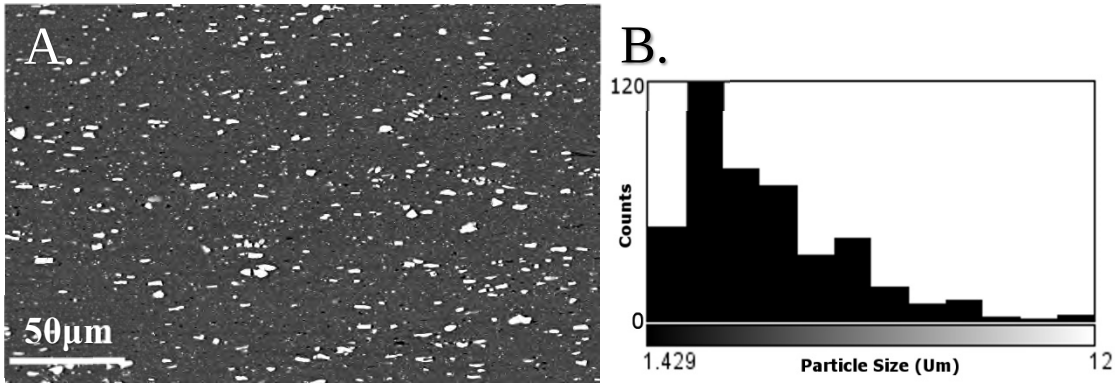

Fig.53. a) BSE image of as rolled V3CN, b) particle size distribution.

### *3.6.3. Discussion*

As seen within previous submissions, imaging of the materials in the as rolled condition is extremely difficult due to the highly deformed and unrecovered nature of the samples. The 'bands' of grains however are much clearer within the AA7020 alloy than the V3C or V3CN, these alloys having more intermetallic particles ($Al_3Ni$) due to the nickel content which will cause zero indexing during EBSD. These $Al_3Ni$ particles are much harder than the surrounding matrix and as such sit proud of the surface after polishing, causing zero indexing. The presence of the particles also causes some distortion in the surrounding matrix leading to poorer indexing in these areas.

As before the shoulder sections where no deformation has taken place of all three materials show a fully recrystallized grain structure after forming, with little to no evidence left of rolling direction and random IPF shading of grains indicating random

grain orientation. The AA7020 again has the coarsest grain structure with average size around 11µm, the V3C the finest average grain size around 6µm and then V3CN with a coarser 8µm grain size. All grain sizes are listed in table 15.

Looking at the deformed sections of the alloys, there are clear differences between the AA7020 alloy and the two nickel containing alloys V3C and V3CN. Firstly the orientation of the AA7020 is heavily orientated in the 001 plane as shown by the red and orange colouring, showing orientation in the direction of forming. This does not mean that all grains are in the exact same orientation merely that they have moved or rotated towards a similar orientation during the forming. The two nickel alloys both have large numbers of grains orientated in this direction, but the majority are coloured blue, corresponding to 111 orientation, this suggests that the nickel content within the alloys is causing rotation of grains with preferred orientation in this plane.

BSE images of V3C and V3CN shown in fig. 52 and 53 respectively show the difference in particles shown in white between the two alloys. Particle size analysis gave an average particle size of 3.52 µm within the V3C and 4.02 µm in the V3CN, confirming the coarser particles in V3CN. The size distribution of the particles was observed to be shifted towards the larger particle size.

There are some limitations to this analysis, and as such the finest particles could not be accurately sized. Due to the faster solidification rate of the V3C there are greater amounts of finer particles present, whereas the slower solidification rate of the V3CN allowed for agglomeration of these finer particles into the coarser particles present. This lack of finer particles would help to explain for the differences in formability of the two alloys. Further investigation by means of TEM would be required to accurately quantify both the size and amount of these finer particles present.

The other noticeable difference is that the V3C and V3CN alloys show evidence of forming with elongated grains in the direction of forming visible. This suggests that the alloys were fully recrystallized before forming took place and that no dynamic recrystallization of the alloys took place during forming. The AA7020 shows little evidence of forming direction with none elongated grains, this suggests that dynamic recrystallization is taking place during forming allowing the grains to maintain their original undeformed shape. This was hypothesised as the reason behind the AA7020s better formability during cone testing at SUSA reported previously.

Areas of cavitation were extracted using GIMP software which showed that the original AA7020 had around 1.5% cavitation, the V3C had around 3.5% and the V3CN had around 8%. This increase in cavitation again indicates that the processing route of the V3CN compared to the V3C has had a negative impact on formability due to the differences in $Al_3Ni$ particles which in the V3CN act as further areas for cavitation to occur, causing decreased formability. Due to the analysis required human judgement on what constitutes an area of cavitation within the alloys these values are not exact and presented as for comparison to each other, to establish a more accurate value further analysis would be required.

With the single stage homogenisation treatment applied to the V3CN in fig.49.a the average grain size was 231µm and with the two stage in fig.49.b the average grain size was 145µm. The images are representative of the structure over the whole surface, suggesting that the two stage treatment yields a finer structure at this point of the processing. Which may help to explain the difference in size and distribution of $Al_3Ni$ particles between the V3C and V3CN.

SE imaging shown in fig.50.a and b and corresponding EDX analysis shown in fig.51.a and b of the V3CN after the different homogenisation treatment show that the distribution of the nickel over the sample surfaces was fairly similar. The only differences being some areas of nickel conglomeration seen in the bottom left corner of fig.50.a and fig.51.a which were representative of areas across the larger surface of the material. These areas of conglomeration were only seen with the single stage homogenisation treatment and not with the two stage treatment that was used with the original V3C.

This again indicates that the two stage homogenisation used within the V3CN was in part responsible for the difference in $Al_3Ni$ size and distribution from the V3C alloy which has in turn been responsible for the decrease in formability and increased cavitation within the alloy. The greater influence on $Al_3Ni$ size was the difference in solidification rates but due to lack of cast samples of the V3C this difference could not be quantified.

### *3.6.4. Conclusion*

The 1.6wt% nickel addition to the V3C alloy has led to a finer microstructure after recrystallization than the AA7020 alloy. This is due to the $Al_3Ni$ particles present offering a further mechanism for static recrystallization not present in the AA7020.

The different processing route, in particular the difference in solidification rate in combination with the different homogenisation treatments of the V3CN to the V3C has led to a coarser microstructure. This is due to the difference in size and distribution of the $Al_3Ni$ particles within the two alloys.

There is some limited evidence to suggest dynamic recrystallization within the AA7020 due to the applied strain during forming. This mechanism within the V3C and V3CN is

different with the $Al_3Ni$ particles accelerating static recrystallization by PSN before the application of eternal load.

The AA7020 alloy suffers from less cavitation than the V3C and V3CN, indicating failure by necking. The $Al_3Ni$ particles in the V3C and V3CN alloys initiate cavitation within the alloys which subsequently fail by coalescence of these cavities.

### *3.7. In-Situ EBSD & FSD Analysis (Submission 4)*

#### *3.7.1. Methodology*

In-situ heated testing was conducted on the AA7020, V3C and V3CN alloys in the as received condition to observe in real time the effect of heating on the materials grain structure and its evolution over time as well as to establish the recrystallization temperature of the alloys. Samples were prepared in the same manner as for standard EBSD analysis, however after polishing samples were then removed from the resin.

Polished samples of the material were then mounted using conductive graphite paint onto Gatan sample holders and then loaded on a Gatan Murano heated stage which was fixed at an angle of 70°. Test temperature was controlled using Gatan software, temperature profiles are detailed for each test within the results chapter. All tests were conducted using a 240µm aperture and 20 keV accelerating voltage, step sizes were varied depending on level of magnification and the desired resolution of images. Samples were held at 200°C for five minutes to allow for degassing to avoid any contamination of the microscope, scans were conducted after this stage to ensure no recrystallization of the materials had occurred and that the original structure was unchanged.

FSD analysis was used for all samples to identify recrystallization across the sample surface. FSD yields a greyscale image that depending on the detectors active gives a

chemical contrast based on the atomic number, a topographical contrast, or for this project particularly interesting contrast based on crystallographic orientation of each grain that is similar to EBSD Band Contrast images. More details about this method can be found in Oxford Instruments FSD product page [78]. This method was used due to the quicker scan rate than EBSD meaning microstructural changes could be better captured. EBSD was used to analyse the microstructure in detail after the end of the heated stage test.

Oxford Tango software was used to post process samples and establish the recrystallization fraction of the alloys after heating by local average misorienation. This averages the orientation of pixels relative to each other within separate grains, any grains with an average misoriention below 1° are taken to be recrystallized.

### *3.7.2. Results*

Fig.54.a-g show FSD images of AA7020 with temperature and time at temperature detailed, samples were brought up to 320°C from degassing temperature in 1 minute, and from 320°C to 327°C in five seconds. This heating rate was used to mimic that which would be seen within an industrial forming process to look at the microstructure during the preheat stage of the process.

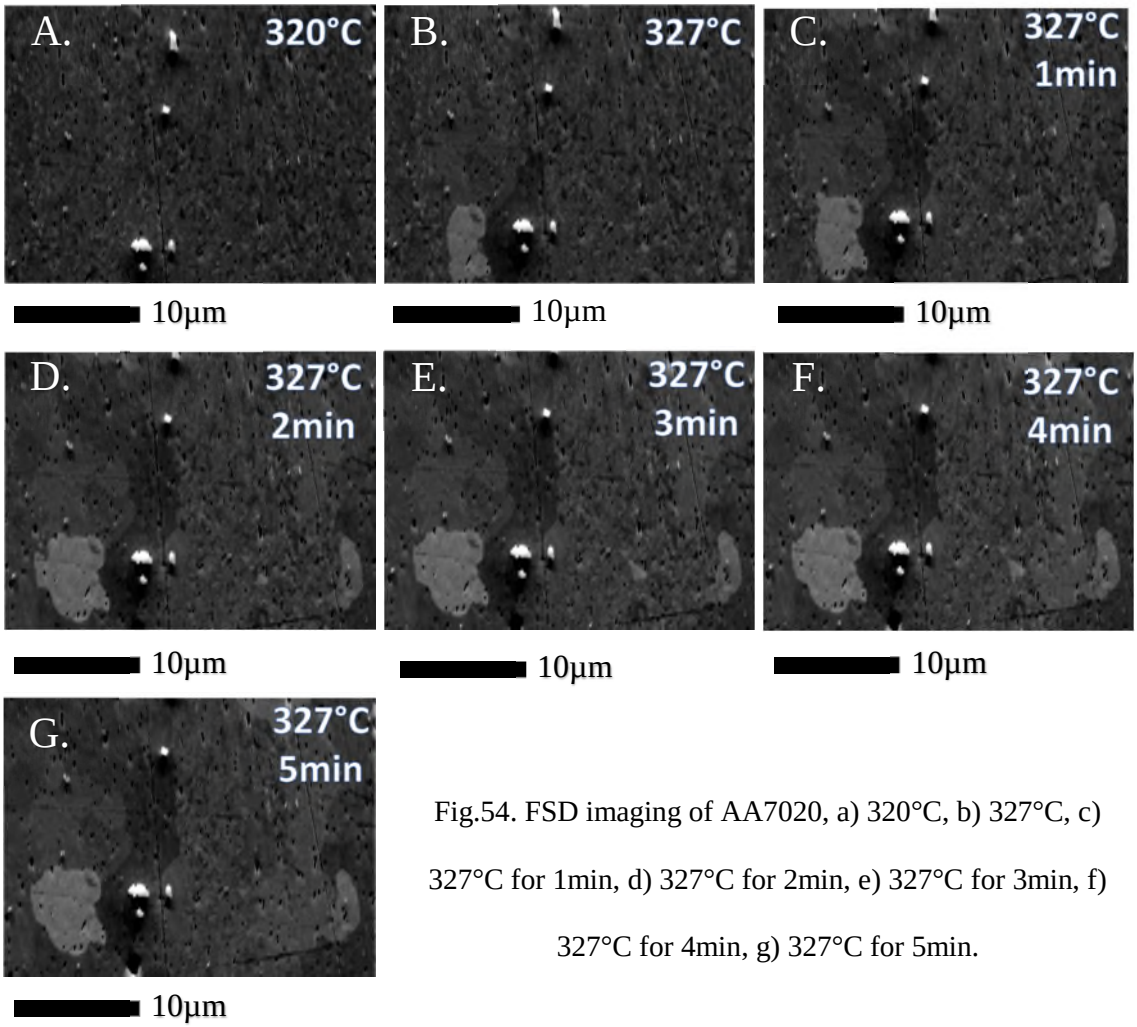


Fig.54. FSD imaging of AA7020, a) 320°C, b) 327°C, c) 327°C for 1min, d) 327°C for 2min, e) 327°C for 3min, f) 327°C for 4min, g) 327°C for 5min.

To analyse potential grain growth within the alloy, a sample was heated to 500°C over a 30 second period from 200°C degassing temperature. FSD scans were taken after 10 seconds and 15 minutes to compare the microstructure as shown in fig.55.a and b.

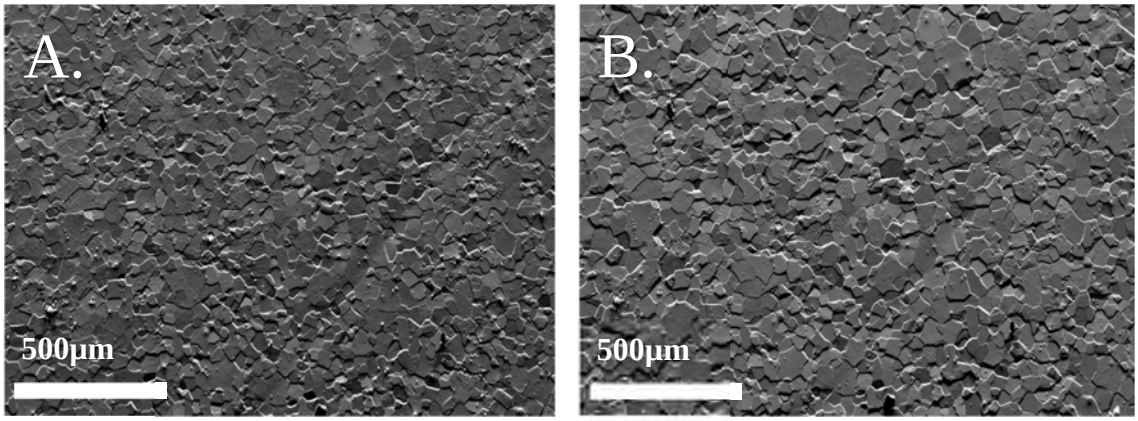


Fig.55. AA7020 FSD images after a) 10 seconds, b) 15minutes at 500°C

The alloy was then subjected to a very fast heating rate of 150°C/s up to 310°C, FSD imaging was taken of the alloy in this condition shown in fig.55 a . The alloy was then returned to room temperature to freeze the structure and an EBSD scan carried out, from which the recrystallized fraction was determined the images of which are shown in fig.56 b and c.

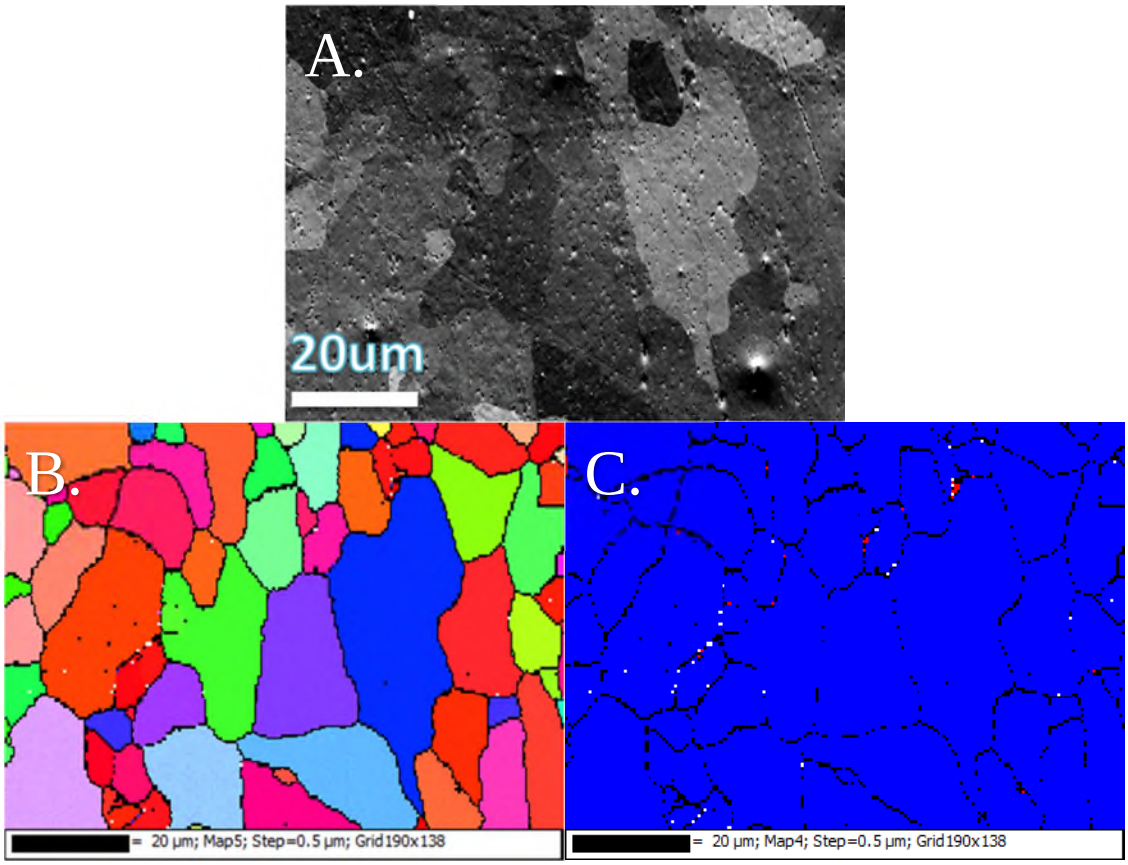

Fig.56. AA7020 images after heating a) FSD scan, b) EBSD scan. c) Recrystallized fraction.

Scans were carried out to establish the temperature at which the V3C showed evidence of recrystallization (277°C), with this established a series of scans were conducted at this temperature to compare to the AA7020 images. These are shown in fig.57.a-g as with the AA7020 the V3C temperature was raised from degassing temperature over one minute.

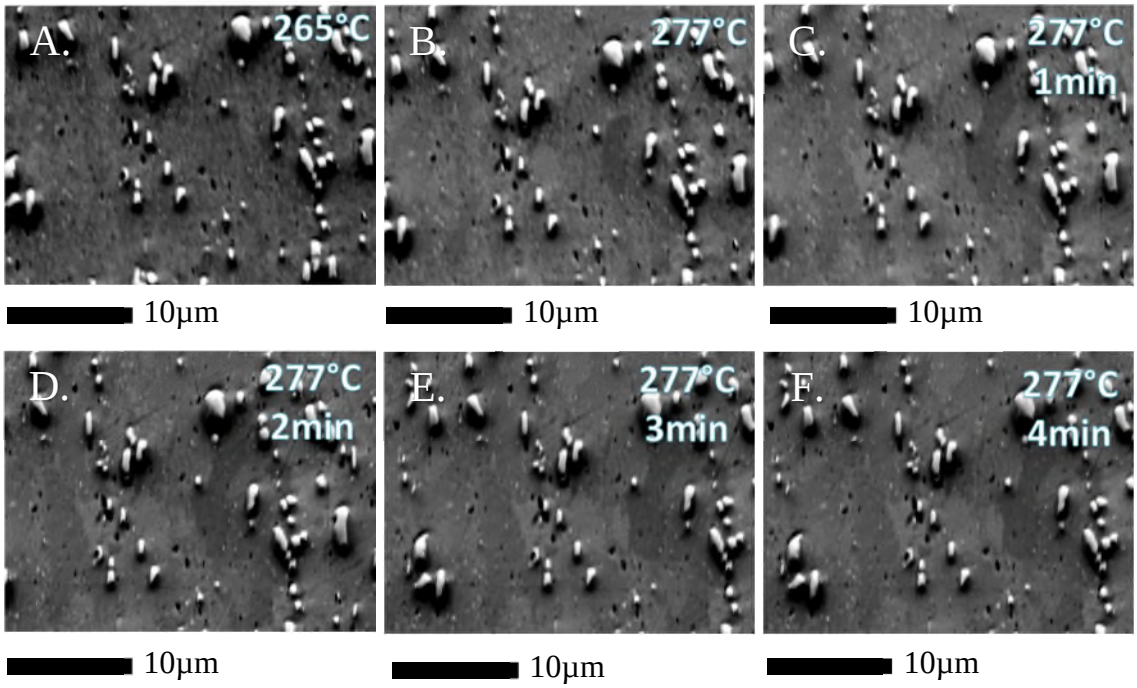


Fig.57. FSD imaging of V3C, a) 265°C, b) 277°C, c) 277°C for 1min, d) 277°C for 2min, e) 277°C for 3min, f) 277°C for 4min, g) 277°C for 5min.

As with the AA7020, the V3C was also subjected to 500°C after heating from 200°C over a 30 second period. FSD scans were taken after 10 seconds and then after 15 minutes to compare the microstructure to look for evidence of grain growth shown in fig.58a and b.

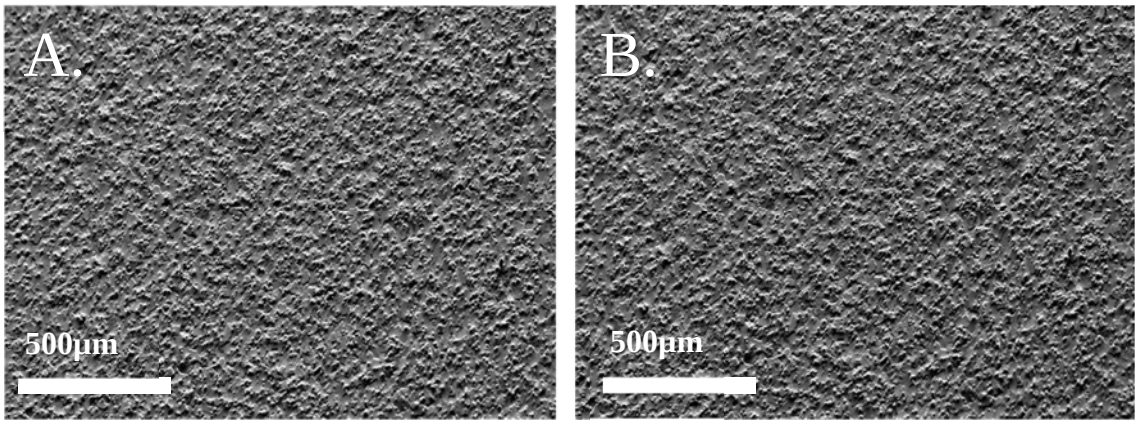


Fig.58. V3C FSD images after a) 10 seconds, b) 15minutes at 500°C.

As with the AA7020 the alloy was then subjected to a very fast heating rate of 150°C/s up to 310°C, the FSD image of this is shown in fig.58 a. The alloy was then returned to room temperature and an EBSD scan carried out for a direct comparison to the AA7020 structure and recrystallized fraction, shown in fig.59.b and c.

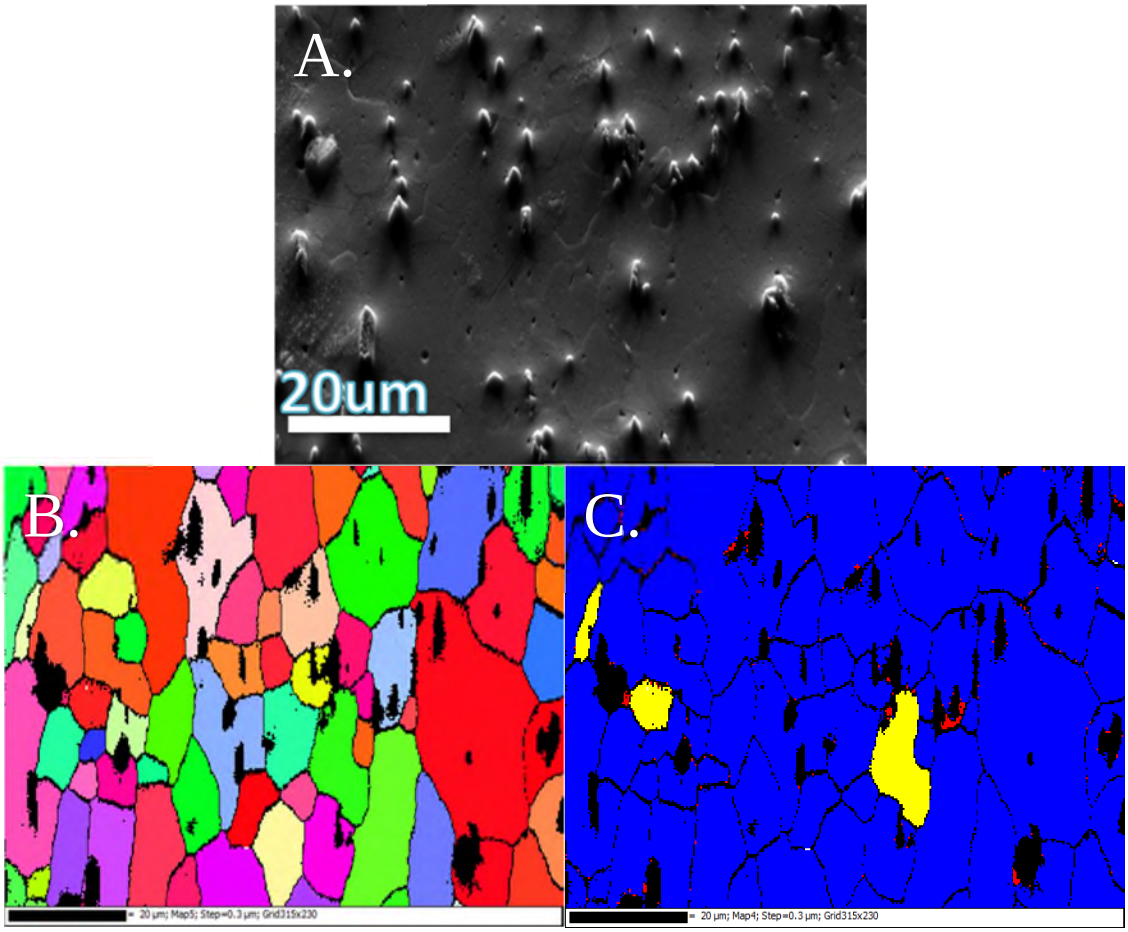


Fig.59. V3C images after fast heating a) FSD scan, b) EBSD scan. c) Recrystallized fraction.

The temperature at which recrystallization was evident within the V3CN alloy was established as 285°C a series of scans were conducted at this temperature to compare to the AA7020 and V3C images. These are shown in fig.60.a-g as with the other alloys the V3CN temperature was raised from degassing temperature over one minute.

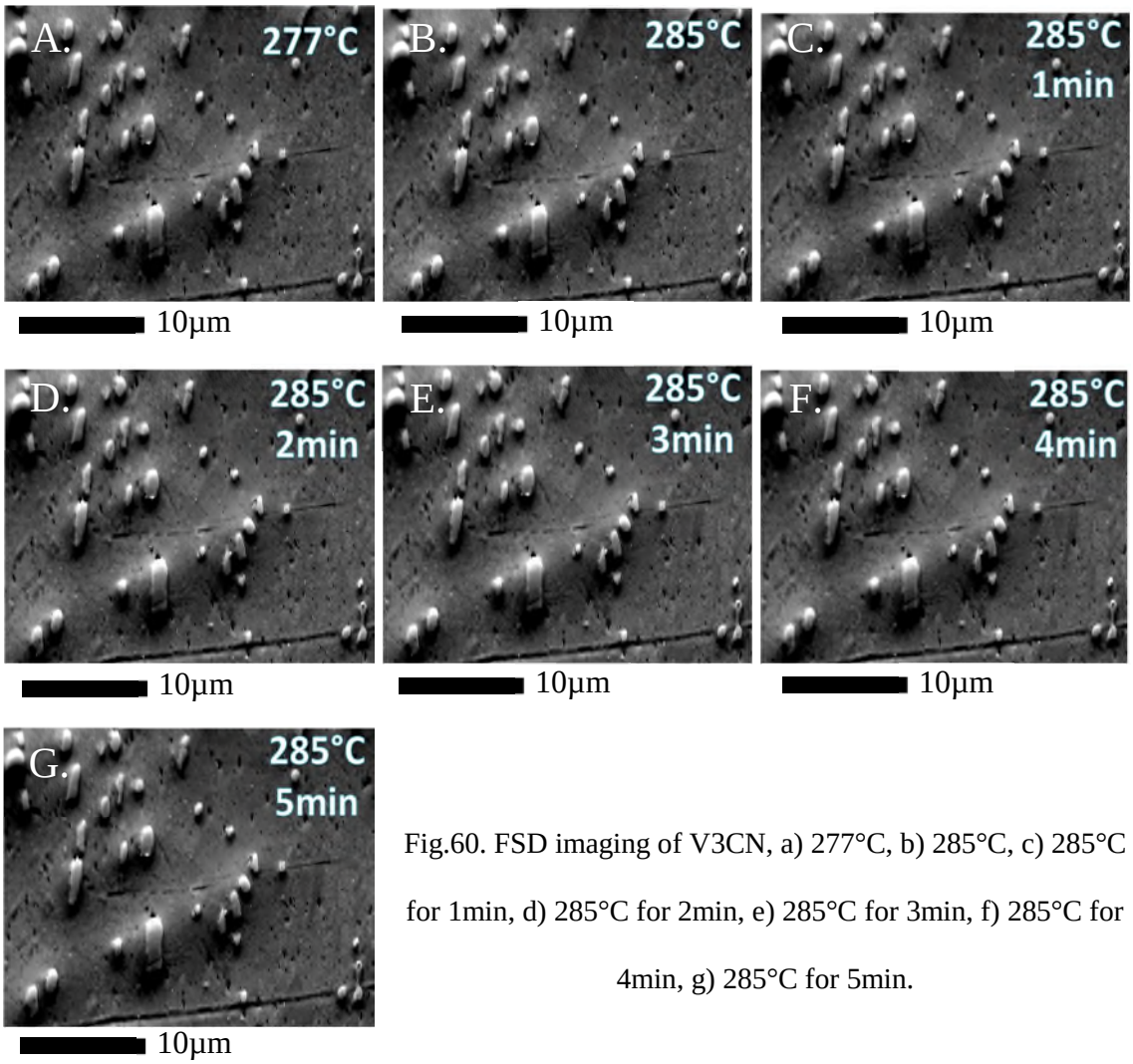


Fig.60. FSD imaging of V3CN, a) 277°C, b) 285°C, c) 285°C for 1min, d) 285°C for 2min, e) 285°C for 3min, f) 285°C for 4min, g) 285°C for 5min.

The V3CN was also subjected to 500°C after heating from 200°C over a 30 second period. FSD scans were taken after 10 seconds and then after 15 minutes to compare the microstructure to look for evidence of grain growth shown in fig.61a and b.

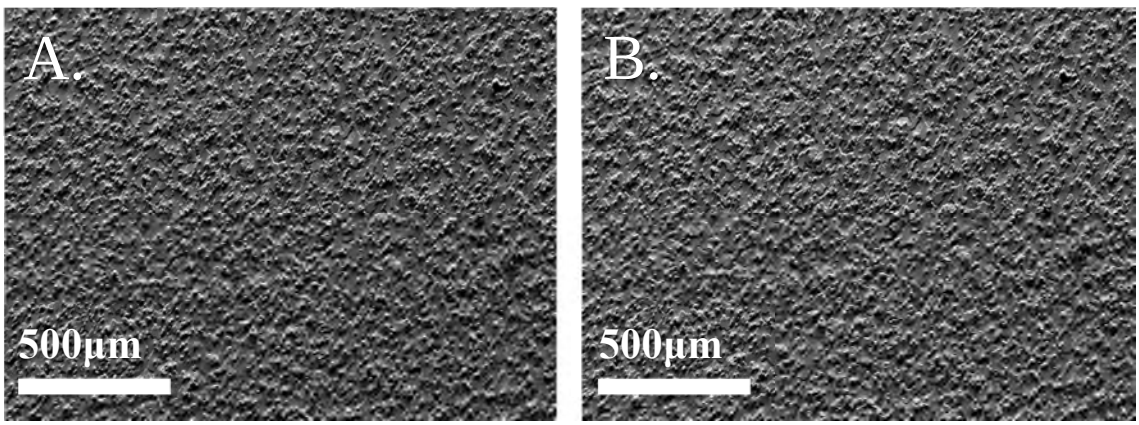


Fig.61. V3CN FSD images after a) 10 seconds, b) 15minutes at 500°C.

The VCN alloy was also subjected to a very fast heating rate of 150°C/s up to 310°C, the FSD image of this is shown in fig.62a. EBSD carried out at room temperature and recrystallization fraction for comparison to both other alloys are shown in fig.62.b and c.

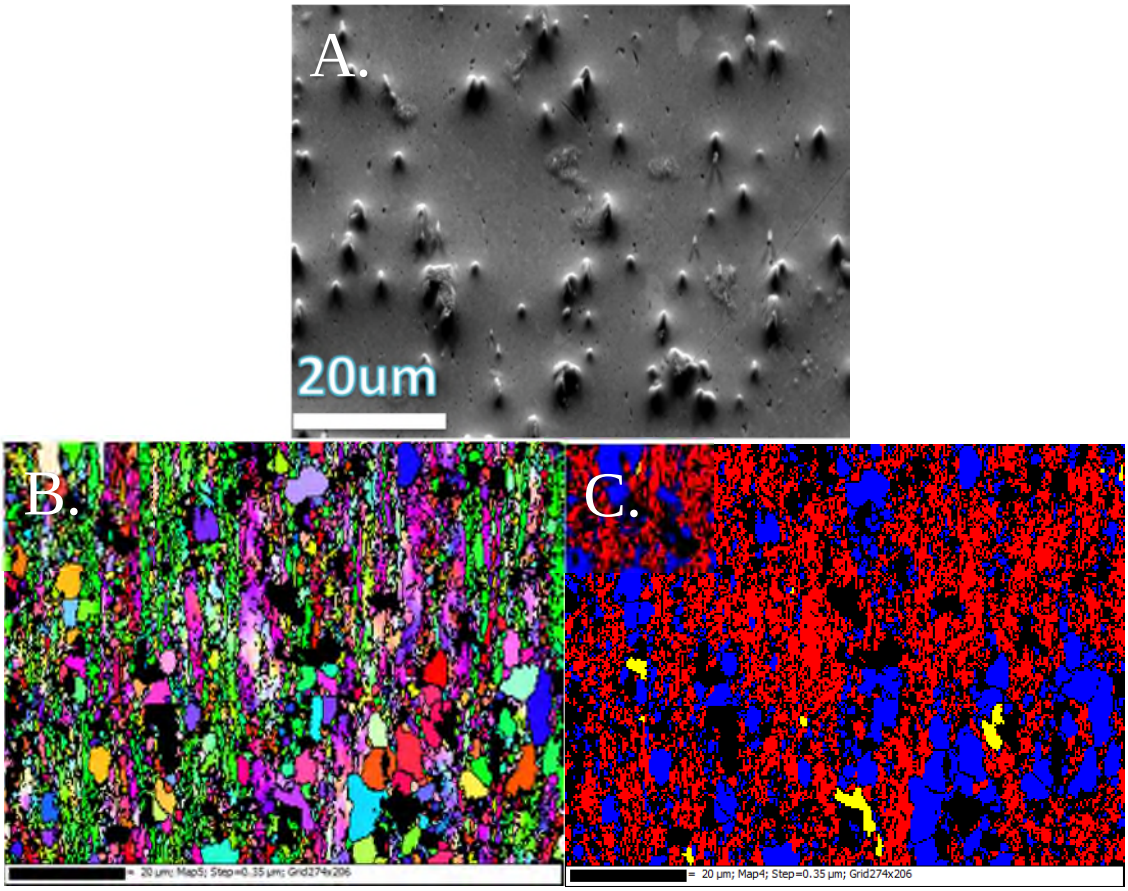


Fig.62. V3C images after fast heating a) FSD scan, b) EBSD scan. C) Recrystallized fraction.

### *3.7.3. Discussion*

Evidence of recrystallization becomes apparent in FSD imaging of AA7020 at 327°C as shown in fig.54.a with new grains clearly evident in the bottom left and right corners of the image, these grains were seen to coarsen as duration at temperature increased. In the lower left corner of the image, there is some evidence of Zener pinning of the grains by the finer $MgZn_2$ intermetallic, with the large pale grains growth halted by a smaller particle at its boundary. After five minutes little evidence of grain growth or surface

changes were visible suggesting the material was stable at this point and recrystallization had completed.

Imaging at the higher temperature of 500°C shown in fig.55 a and b show a fully recrystallized structure after 30 seconds, with no grain growth evident after 15 minutes held at temperature. This shows that the kinetics of the recrystallization is greater at the higher temperature due to the increased driving force due to rapid heating, causing the material to recrystallize far quicker. This is also shown by the relief of the grains, where the slow heating rate yielded grains all in the same plane, the fast rate shows grains that are at different "levels" and "heights" to each other. It also demonstrates the material is very stable, not undergoing any grain growth after recrystallization, due in part to the pinning effect of the intermetallics within the alloy.

The effect of a very fast ramp rate to temperature as shown in fig.56.a,b and c show that the material is fully recrystallized after a very short time at temperature, confirmed by the recrystallization fraction image which shows recrystallized grains in blue. The kinetics of recrystallization therefore appear to be dependent upon both time to achieve temperature as well as the temperature itself. The grain structure is near identical to that of bulk EBSD imaging in section 3.6.2 of this report showing that this technique is valid for the bulk material and not just surface effects.

The V3C material showed evidence of recrystallization at 277°C shown in fig.56.b, as with the AA7020 material grain coarsening was then observed, but after 5 minutes this coarsening appeared to stop. The presence of nickel containing $Al_3Ni$ particles halting grain growth earlier, leaving a finer grain structure than the AA7020 which has been seen previously within this study.

The effect of the fast heating rate shown in fig.58 a and b again shows a fine fully recrystallized structure after 30 seconds, and after 15 minutes shows no sign of grain growth or grain coarsening. As with the AA7020 the V3C exhibits a stable structure after recrystallization, again due to the presence of large numbers of secondary particles inhibiting grain growth. There is also evidence of raised grains suggesting much faster recrystallization kinetics.

The recrystallization fraction of the material shown in fig.59.c shows a nearly fully recrystallized structure with 97% recrystallized 3% recovered grains. Unlike the AA7020 the V3C is not completely recrystallized but does have a finer grain structure which is preferential for SPF forming. As with AA7020 the observed grain structure of the sample is seen to be the same as in the bulk material.

The V3CN as shown in fig.60.b started to show evidence of recrystallization at the higher temperature of 285°C, the surface effect was more subtle than within the other alloys, suggesting that the process was taking place more slowly. These slower kinetics making it harder to observe the recrystallization.

As with both other alloys V3CN is fully recrystallized after 30 seconds at 500°C and shows no sign of grain growth, the structure after 15 minutes dwell at temperate being the same as 30 seconds, shown in fig.61. a and b. When heated at the faster rate of 150°C/s the V3CN was seen to be in a quite heavily deformed state when compared to the other alloys, with only 35% recrystallized fraction and 4% recovered. This is significantly lower than the V3C and the AA7020 both of which were seen to be fully or nearly fully recrystallized in this condition.

This suppression of recrystallization within the V3CN is likely due to the nickel containing $Al_3Ni$ particles within the alloy, the size and distribution of which are different

to the V3C alloy. Within the V3C they seem to offer faster recrystallization by means of PSN and the smaller sized particles then limiting grain growth by pinning grains. The distribution and size of particles within the V3CN seem to lessen the PSN effect of the particles or at least slows the recrystallization, they do however still help to pin grains, resulting a slighter coarser structure than the V3C but still significantly finer than in the AA7020.

### *3.7.4. Conclusion*

All materials will be fully recrystallized, with a microstructure showing no signs of grain coarsening during the preheating stage of a typical forming process. The AA7020 having an average grain size around 10µm, V3C around 6µm and V3CN around 8µm.

The finer average grain size observed within the V3C compared to the AA7020 is attributed to the presence of $Al_3Ni$ particles which aid faster recrystallization by means of PSN and help to pin grains halting grain growth.

The difference in processing of the V3CN compared to the V3C has led to a coarser grain structure and a slower recrystallization rate than seen in the V3C. This is attributed to the difference in size and distribution of $Al_3Ni$ particles between the two alloys mainly due to the difference in solidification rates due to different cast sizes and also due to the difference in homogenisation treatments.

# 4. Discussion

## *4.1. Literature Review*

A review of the literature showed that hybrid superplastic forming processes have been investigated and are currently employed in various areas of industry. This has been approached in various ways, using mechanical preforming or by use of higher strain rates, material flow into the tool was only present during the mechanical preforming and not during the gas bulge stage [58-63]. It also highlighted the use of coarse grained materials within super plastic forming processes, as well as the addition of nickel to 7XXX alloys to achieve a finer grain structure for super plastic forming [52-54].

The review showed a gap where a combination of these factors, using a mechanical preforming stage and then gas bulge at higher strain rates in combination with a reduced clamping force to allow material flow could be employed. It also demonstrated the possibility of using nickel additions to AA7020 to allow for a material that could recrystallize during the forming process allowing for the use of a cheaper alloy industrially.

## *4.2. Effect of Scale up on Materials*

V3C was shown to offer significant improvements in formability and strength when compared to AA7020, as such it was cast in a larger scale termed V3CN. V3CN showed decreased formability compared to the V3C in tensile and gas bulge tests. This was attributed to the differences in $Al_3Ni$ particle size and distribution between the two alloys. These differences arose from the different solidification rates of the alloys due to the difference in cast size, the difference in homogenisation treatments also likely had a slight influence on the particle sizes. Lack of cast V3C material meant that the influence of

solidification rate and homogenisation treatment could not be fully quantified, these effects would need to be investigated on new batches of material.

### *4.3. Experimental Work*

Initial testing showed the promise of AA7020 within and SPF forming process, with good levels of linear elongation within the target five minutes cycle time. The addition of 1.6wt% nickel to the alloy V3C showed significant improvements in ductility up to 204% linear elongation and an improvement in strength suggesting this would be an even more promising alloy.

Owing to this improved formability scale up of production of the V3C alloy in the form of V3CN was conducted. The effect of this scale up was a further increase in material strength to 342 MPa, but a decrease in formability due to differences in the size distribution of $Al_3Ni$ particles within the alloy. Primarily differences in the solidification rate of the two materials and to a lesser extent the difference in homogenisation treatments led to this difference between the two alloys.

Testing at SUSA using truncated cone tools with sharp male radius geometries showed the ability of AA7020 to form parts with in excess of 400% equivalent strain, the material requiring a minimum of 100% equivalent strain before contacting a male radius to form successfully. In the same geometries the V3CN was seen to have an upper limit of 100% equivalent strain, but being able to form parts successfully with lower strains where the AA7020 failed. This was attributed to greater static recrystallization by PSN due to the $Al_3Ni$ particles present in the V3CN compared to the AA7020, the AA7020 then possibly undergoing dynamic recrystallization during the forming, hence requiring the minimum of 100% equivalent strain before contact with the tool.

PSN is likely occurring at a lower level in AA7020 compared to V3C and V3CN due to the $MgZn_2$ particles present, the larger amount of $Al_3Ni$ particles in the V3C and V3CN leading to greater levels of recrystallization due to this mechanism. The higher strain rates employed during testing mean that dislocation creep rather than GBS is responsible for material elongations. All alloys likely undergo PSN, dislocation creep and possibly some limited amounts of dynamic recrystallization, but due to the different chemistries these mechanisms act at different amounts at different stages of the process. To properly identify and quantify this difference in-situ techniques such as heated tensile stage confocal microscopy or EBSD will be required.

Testing using custom made tooling which combines a slight mechanical preforming in combination with gas bulge testing at higher strain rates whilst allowing for material flow reinforced testing at SUSA. This testing showed the ability of the V3CN to form parts again with an upper limit of around 100% equivalent strain. Whilst the AA7020 showed the need for at least 100% equivalent strain before contact. The testing also confirmed the need for a mixture of graphite and a lower lubricity lubricant in areas of contact with male radii.

Heated stage EBSD and FSD analysis of the three alloys established the recrystallization temperatures of the three alloys with AA7020 showing recrystallization occurring at 327°C. V3C was seen to recrystallize at 277°C and V3CN at 285°C, the $Al_3Ni$ particles leading to earlier recrystallization due to greater levels of PSN. The coarser particles in V3CN compared to the V3C slightly retarding this added mechanism. This negative impact of the coarser particles within the V3CN was confirmed with a fast ramp to 300°C and fast cooling to room temperature which lead to a nearly fully recrystallized structure for the V3C but only 33% recrystallization within V3CN. The AA7020 under the same conditions was shown to be 100% recrystallized, this suggests that the same mechanisms

for recrystallization are acting within all three alloys however at varying levels at different points within the preheat and subsequent forming stages.

Bulk EBSD highlighted differences in grain size of the alloys with AA7020 having the coarsest structure with an average 11μm grain size, the V3C 6μm and V3CN 8μm. This showed the influence of the $Al_3Ni$ particles on recrystallization, the added PSN from these particles leading to a finer microstructure in comparison to AA7020. The AA7020 showed less grain growth after forming than V3C and V3CN and also a lack of grain elongation which was observed in both V3C and V3CN. This suggests that there was some limited dynamic recrystallization within AA7020 with none in either V3C or V3CN, or that the same mechanisms were present in all three alloys but due to the $Al_3Ni$ particles they acted at different levels at different stages of the process.

Failures within both V3C and V3CN were observed to be "tearing" type failures, compared to more localised necking and thinning within the AA7020. This again is due to the $Al_3Ni$ particles which act as areas of nucleation of cavitation as they are not affected by the temperature of the forming process and remain present within the matrix as coarse intermetallics throughout. This was strengthened by the levels of cavitation observed within the three alloys after failure, 1.5% in AA7020, 3.5% in V3C and 8.5% in V3CN.

### *4.4 Process Routes Comparison*

In this study an innovative method to produce high strength parts for use in niche vehicle manufacture, by means of a modified SPF forming process used in conjunction with a typically non SPF alloy AA7020 was developed. This section of work details the process route of AA7020 from casting through to final part production using the new modified forming process. A comparison to the nickel containing V3C and V3CN alloys

investigated within this study is also proposed, which were produced on an experimental scale using processes based around the 7020 commercial production route.

The material production stage which comprises casting, homogenisation and rolling regimes were either well established commercial practices for AA7020 or developed separately by partners within the project for V3C/N. Optimization of the material production stage was therefore not the aim of the work within this project. The area where the major innovation has been achieved is within the part production stage which comprises the forming process and post forming treatments, as such these two stages will be described separately. In this section a comparison to parts formed in AA5083 is proposed to better highlight the new process route and differences to current industrial practices.

### *4.4.1. Material Production*

AA7020 was produced commercially by Hydro aluminium by a well-established commercial process route, the alloy was DC (direct chill) cast, homogenised and rolled to a final gauge thickness of 1.6mm sheet. The sheet was supplied hard rolled, having undergone no further heat treatments after cold rolling to final gauge. Nickel containing alloys V3C and V3CN were produced on smaller scales but the processing route was the same as that of the AA7020, being cast, homogenised, hot rolled, annealed and then finally cold rolled to 1.6 mm. The material production stage of the nickel containing alloys have not yet been optimised to achieve a homogenous distribution of fine $Al_3Ni$ particles. Issues with coarsening of $Al_3Ni$ particles which negatively impacted on

formability were observed within this study, as such they would require significant further research to achieve a commercially viable alloy.

## Casting

AA7020 and nickel containing variants were cast between 750°C and 800°C with preference to casting at the higher temperature due to the presence of 0.1 wt% zirconium. The zirconium is added to the alloy to assist heterogeneous nucleation of new grains by increasing nucleation sites due to the presence of $ZrAl_3$ particles which precipitate before solidification of the alloy. Fig.63. shows the aluminium rich end of aluminium zirconium equilibrium phase diagram, with the level of zirconium present in AA7020 highlighted showing the solidus temperature of $ZrAl_3$. The same particles later during the forming process act to restrict grain growth by means of Zener pinning [47].

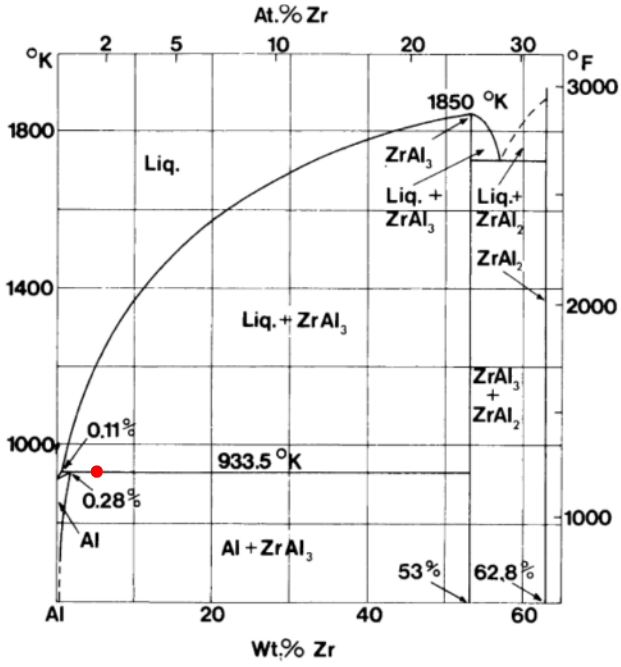


Fig.63. Aluminium rich end of aluminium zirconium equilibrium phase diagram with 0.1wt% Zr highlighted [79].

Magnesium and zinc additions cause the formation of various secondary particles within Al-Zn-Mg alloys, the particles formed being dependant on temperature and by the ratio of Mg:Zn. In the case of AA7020 this is 1.6:4.5 which lies between the 2:5 and 1:7 region where $MgZn_2$ is the main secondary particle formed within the alloy [79]. The liquidus and solidus projections for the Al-Zn-Mg system are shown in fig.64 and fig.65. Fig.66 shows how the solid state phase fields change with temperature for the Al rich corner of the Al-Zn-Mg system. From these diagrams it is possible to estimate the liquidus, solidus and solvus temperatures for AA7020 as 650°C, 615°C, and 260°C respectively.

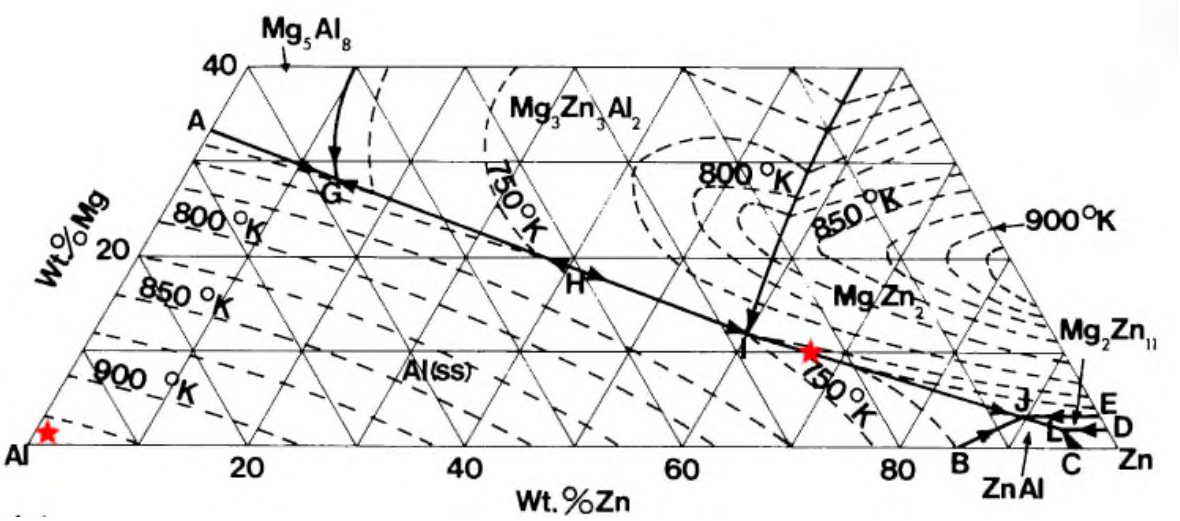


Fig.64. Liquidus projection for Al-Zn-Mg system with liquidus and eutectic points highlighted [79].

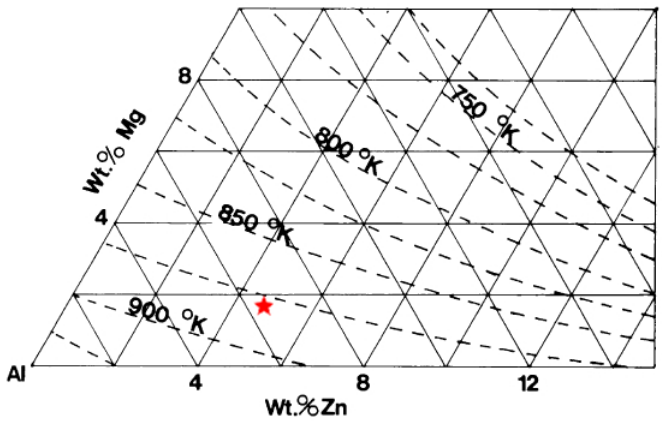


Fig.65. Solidus projection for Al-Zn-Mg system with solidus point highlighted [79].

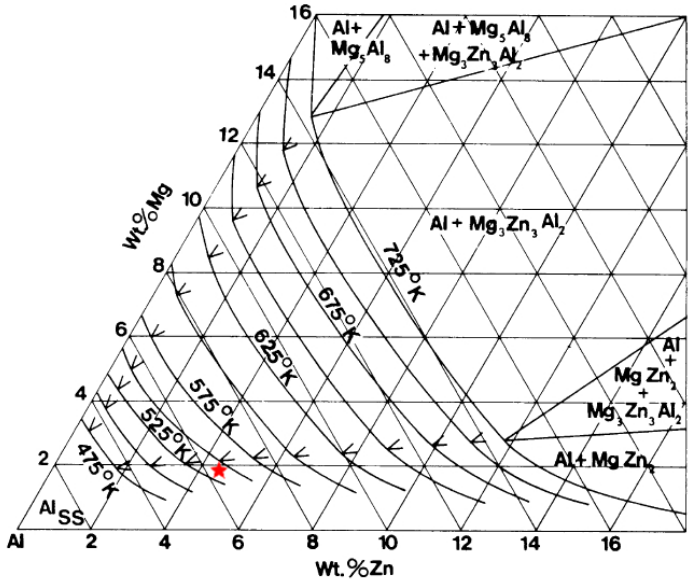


Fig.66. Aluminium rich corner of Al-Mg-Zn phase diagram with solvus temperature highlighted [79].

Solid state diffusion of alloying elements during cooling will be significantly lower than the liquid during solidification and given the relatively quick cooling rates during DC casting non-equilibrium solidification of the alloy will occur. This non equilibrium solidification leads to solute poor α solidifying first which as solidification progress leads

to a solute enriched liquid. Under equilibrium condition solidification would be expected to start when the temperature reached 650°C and complete at 615°C. However due to the non-equilibrium conditions the solidus will be depressed and the last liquid to solidify will be enriched to the eutectic composition, that solidification being completed at the eutectic temperature of ~500°C. This leads to a 'cored' structure in the primary α with increasing concentrations of solute magnesium and zinc towards the grain boundaries [80] where the eutectic $MgZn_2$ will be present.

Various studies have shown the addition of nickel to 7000 series alloys can have a positive effect on formability and strength [51-53]. Following on from this work additions of 1 wt% and 1.6 wt% were selected by Hydro Aluminium and investigated within this thesis. The aluminium nickel phase diagram is shown in fig.67 and as can be seen the maximum solid solubility of nickel in aluminium is 0.04 wt%. During non-equilibrium solidification some primary $Al_3Ni$ will be formed it is also possible that some nickel will be retained in solid solution which will form secondary $Al_3Ni$ particles during cooling and subsequent homogenisation. The amount of secondary $Al_3Ni$ will be strongly dependent on cooling rate with higher cooling rates leading to higher amounts of secondary $Al_3Ni$. Secondary $Al_3Ni$ will be significantly finer than primary $Al_3Ni$ and will lead to improved material performance [81].

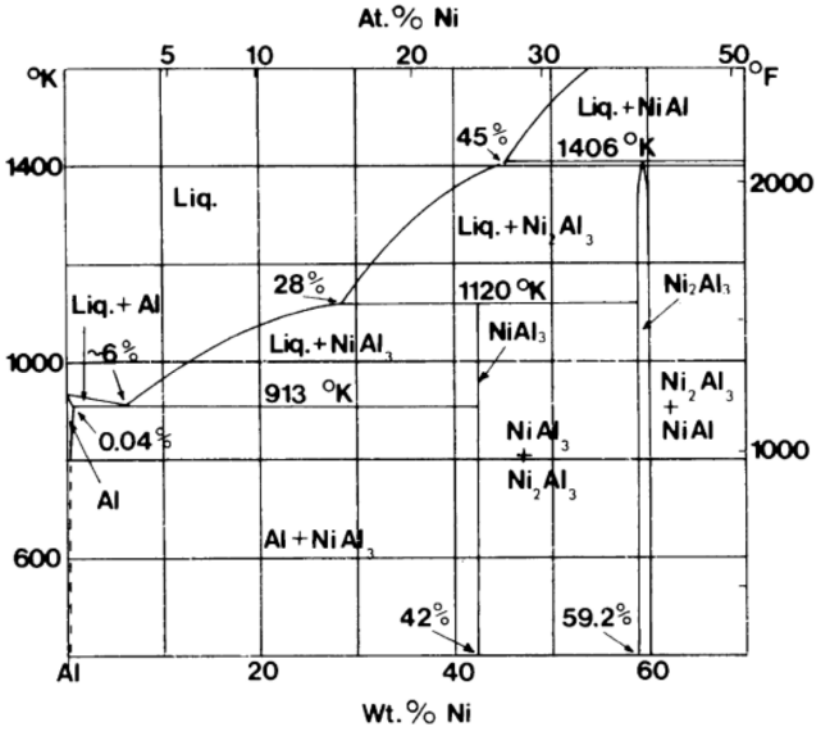


Fig.67. Aluminium rich end of aluminium nickel equilibrium phase diagram [79].

As with AA7020 there are issues with non-equilibrium cooling of the V3C/N alloys after casting and again secondary phases are last to solidify and agglomerate at grain boundaries. In both V3C and V3CN $Al_3Ni$ particles precipitate out of solution as primary particles due to the low solubility of nickel in aluminium and the eutectic temperature of 640°C being greater than the solidus temperature of AA7020. These particles also agglomerate at grain boundaries of the alloys as shown in fig.68 which shows an EDS nickel map of as cast V3CN material with nickel shaded orange.

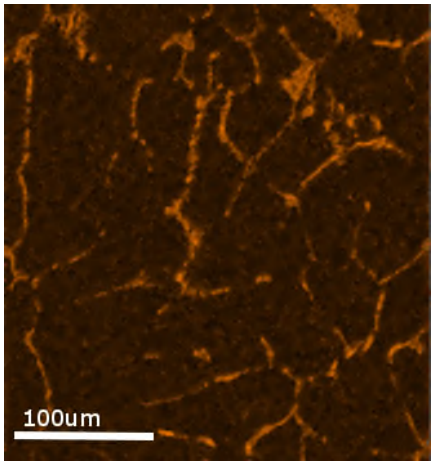


Fig.68. EDS map illustrating agglomeration of nickel rich particles at grain boundaries.

As mentioned earlier the rate at which to the alloy is cooled from casting temperature will control the level of primary $Al_3Ni$ formed in the alloy. Here the first difference between V3C and V3CN is seen, with the alloys being cast in 10kg and 60kg sizes respectively, the difference in the casting sizes would have led to a difference in cooling rates with the larger V3CN cast cooling slower than the smaller V3C. This difference in cooling rates would lead to an increase in primary $Al_3Ni$ particles present within the alloy as well as coarsening of these particles, this is thought to be the main reason for the decrease in formability of the V3CN in comparison to the V3C.

Further studies are required to establish the optimum casting parameters for the nickel containing alloy to help control primary particle size and distribution. It is clear that the formation of coarse primary $Al_3Ni$ means that it would be difficult to commercialise these alloys using DC casting as the size of ingot required would result in a low cooling rate and hence significant primary $Al_3Ni$. One possibility would be to use twin roll casting where cast material is directly hot rolled as the process helps to control materials microstructure [82] due to its high characteristic cooling rate.

**Homogenisation**

Following solidification secondary particles are agglomerated ($MgZn_2$ and $Al_3Ni$) at grain boundaries and the α grains are 'cored'. A homogenisation treatment is required to dissolve the $MgZn_2$ and to equilibrate the solute concentrations across the α. Given the low solubility of Ni in Al primary $Al_3Ni$ phase will remain and if anything coarsen during any high temperature heat treatment. In order to achieve this in a relatively short period of time it is essential that the alloy is heated to a temperature to as high a temperature as possible below the solidus. Given the presence of relatively coarse $MgZn_2$ at the grain boundary if the alloy was heated rapidly melting would occur at the eutectic temperature (~500°C). For this reason is normal to use a slow heating rate during homogenisation to ensure that the $MgZn_2$ is dissolved before the eutectic temperature is reached. Alternatively the alloy can be subjected to a two stage heat treatment where an initial hold at a temperature below solvus is applied (to dissolve the $MgZn_2$) prior to heating to the final homogenisation temperature.

The homogenisation treatment for AA7020 has been optimised at Hydro, this homogenisation treatment was the basis for the treatment applied to the V3C alloy, due to an error at the cast house a different homogenisation treatment was applied to the V3CN. Both AA7020 and V3C were subjected to two stage homogenisation treatments 480°C 24hrs + 550°C 2hrs and 520°C 24hrs + 550°C 2hrs respectively. The V3CN was subjected to a single stage treatment of 550°C for 24 hours. Any nickel retained in solid solution during solidification will precipitate out during homogenisation. A two stage treatment will yield a more beneficial distribution of secondary $Al_3Ni$ as a low

temperature hold will promote nucleation over growth of $Al_3Ni$ and hence a finer final distribution of this phase. For this reason the accidental single stage treatment of V3CN was unfortunate and may help to explain the reduction in formability compared to V3C.

**Hot Rolling**

No exact data was available on the hot rolling regimes of the materials from Hydro, but as with all other stages of processing the AA7020 was processed using a well-established industrial regime. Both V3C and V3CN were subjected to hot rolling regimes based around that for AA7020 and as such this was not optimised for the alloy and would require further study to establish the optimal hot rolling regime. During hot rolling the alloy will have started above the solvus temperature, with the temperature being decreased in steps following each pass decreasing the material thickness. It is likely that the final pass will be conducted below the solvus temperature. A typical process would take an ingot produced by DC casting from around 600 mm thickness down to around 20 mm thickness [83].

**Annealing & Cold Rolling**

Annealing of all alloys was conducted at 350°C for two hours to recrystallize the strip and to soften the alloy prior to cold rolling to final gauge. This temperature is above the solvus temperature of the alloy and so had no influence on the distribution of the secondary particles. Again this is an optimised regime for the AA7020 but the influence of different annealing regimes on V3C/N would need to be investigated. The final stage

of the process is cold rolling of the alloys which reduced the material to a final gauge of 1.6 mm for the purpose of this study, the microstructure is not effected thermally at this stage but the grains are heavily deformed by the rolling process leaving a structure with elongated grains in the direction of rolling.

### *4.4.2. Part Production*

**Forming**

The main interest in this project was to develop a method of forming AA7020 using a modified SPF forming process to achieve parts with a strength of at least 300 MPa with reduced cycle times around five minutes. A traditional SPF process at Superform using AA5083 has a minimum cycle time of 10 minutes with most forming processes taking around 20 minutes. In fig.69 comparison is made to the shortest current forming process and details the pressure and temperature cycle for a typical AA5083 alloy compared to that of the AA7020/V3C. The forming pressures are the same for both materials and the forming temperature is typically the same with forming taking place at 500°C.

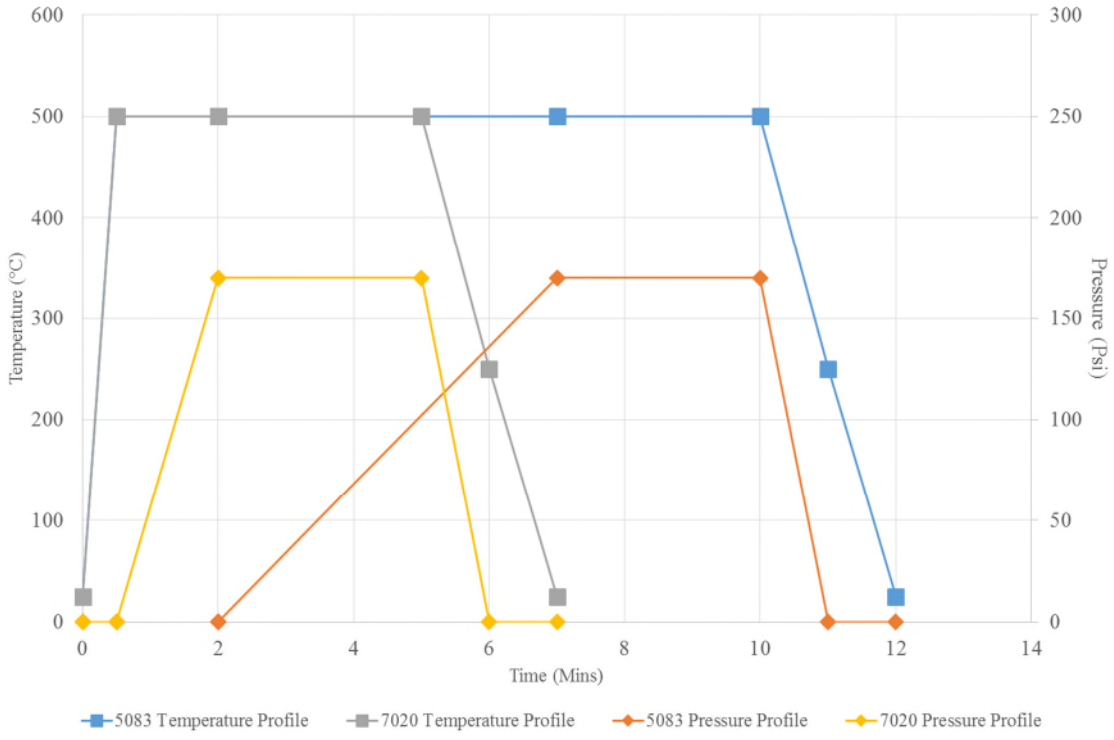


Fig.69. Forming pressure and temperature profiles for AA5083 and AA7020.

The main difference in both cycles is the significant reduction in overall time from ten minutes for AA5083 to five minutes for AA7020 and V3C/N, this reduction in time comes from the AA7020 and V3C/N materials ability to form at higher strain rates but also from the materials ability to begin forming during the early stages of recrystallization. This allows for the pressure to be ramped up faster than with AA5083 and also allows for the removal of the preheat stage which is required with AA5083 to ensure full recrystallization before the application of forming pressure. The implication being that 7020 and V3C/N undergo dynamic recrystallization at this stage of the forming process. A forming cycle for AA5083 follows clamp > preheat > forming including pressure ramp > dwell at pressure > release of pressure, removal and cooling by forced air. AA7020 and V3C/N follow clamp > forming including pressure ramp > dwell at pressure > release of pressure, removal and cooling by forced air.

The heating to the forming temperature simultaneously acts as the solution treatment for both the AA7020 and V3C/N, and due to the materials low quench rate sensitivity (which was established in portfolio submission 5) air quenching with industrial fans for improved air flow leaves the material in a super saturated solid solution with sufficient precipitation potential for precipitation strengthening during aging. The $Al_3Ni$ particles are not affected during the solution heat treatment which takes place below the solvus temperature of the particles. At this point both the AA7020 and V3C are ready for post forming aging treatments to achieve a high strength T5 temper after peak aging. The forming cycle represents optimum parameters for forming temperature, time and pressure which have all established by experiments throughout this study and at Superform.

The primary and secondary particles present in the alloy will have an important effect on the recrystallization and grain growth that takes place during forming. The larger primary particles will act as potential nucleation sites through particle stimulated nucleation promoting grain growth. Whereas the finer secondary particles will retard nucleation and grain growth through Zener pinning. For this reason V3C with the lower fraction of primary and higher fraction of secondary particles has a finer post forming grain structure than V3CN.

**Post forming**

AA5083 is a work hardenable alloy and as such it is not possible to improve the mechanical properties post forming by means of heat treatments. Following forming the

parts are trimmed cleaned and shipped in the “O” temper which is fully annealed with a yield strength of around 145 MPa.

AA7020 was chosen for this study as it is an age hardenable alloy which has a solution treatment temperature comparable to that of the forming process. Forming the material above the alloys solvus temperature produces a super saturated solid solution, due to the thin 1.6 mm material combined the materials low quench rate sensitivity air quenching is sufficient to leave the maintain this condition.

An optimum aging treatment of 90°C for 8 hours and 130°C for 18 hours was experimentally established by testing both at Superform Hydro and within this study. A two stage treatment was selected to improve the corrosion resistance of the material which has been investigated previously [84]. The two stage treatment is used as the lower temperature leads to uniform nucleation across the microstructure preventing significant grain boundary precipitation and the formation of precipitate free zones both of which would be detrimental from a corrosion perspective. This aging treatment was seen to be the optimum treatment for both the AA7020 and the V3C/N alloys leaving them in a T5 temper peak aged to over 300MPa yield strength.

### *4.5. Economic Comparison of Developed Process*

A comparison of the economics of the new alloy and forming process compared to more traditional alloys and processes employed industrially are presented. The alloy and forming process within this study were developed for use within new applications and as such there is no direct comparison so a comparison to the closest current forming and most typical alloy is offered. A typical industrial forming employs AA5083, this will be

taken as the baseline for cost, comparisons are then made to AA7020 as used throughout this project and hypothetically to V3C should it become commercially viable as the material is currently experimental.

Costings are split into two sections, material supply and part manufacture which are detailed in table 16 material supply encompasses the cost of casting, homogenising, rolling and blanking the material. Part manufacture compares the cost of forming, trimming, cleaning, heat treatment and the effect of down gauging due to use of higher strength material. Due to IP agreements, actual values cannot be given but relative costs were established through conversations with the material supplier and Superform [85].

Table.16. Relative cost comparisons between AA5083 AA7020 and V3C.

| | **Relative Cost** | | |
|---|---|---|---|
| | **Material** | | |
| | **5083** | **7020** | **V3C** |
| **Material Supply** | | | |
| Casting | 1 | 1.6 | 1.7 |
| Homogenisation | 1 | 1 | 1 |
| Hot rolling | 1 | 1 | 1 |
| Cold Rolling | 1 | 0.9 | 1.3 |
| Blanking | 1 | 1 | 1 |
| **Total** | 1 | 1.44 | 2.21 |
| | | | |
| **Part Manufacture** | | | |
| Material Gauge | 1 | 0.7 | 0.65 |
| Forming | 1 | 0.5 | 0.5 |
| Trimming | 1 | 1 | 1 |
| Cleaning | 1 | 1 | 1 |
| Heat Treatment | 1 | 2 | 2 |
| **Total** | 1 | 0.7 | 0.65 |
| | | | |
| **Overall Comparison** | **1** | **1.01** | **1.44** |

From table 16 we can see that at the material supply stage AA7020 is more expensive alloy than AA5083 with the base alloy itself being more expensive, but processing costs slightly reduced due to the work hardening of AA5083 making it more difficult to cold roll [85]. Should a suitable processing route become established to achieve acceptable performance with V3C material it is predicted that there would be a further increase in base alloy cost due to the added alloying elements and to control particle size, it is also predicted that cold rolling of the material would be more expensive due to nickel containing particles within the alloy.

During part manufacture the higher strength of the AA7020 compared to AA5083 allows for down gauging of the material leading to a cost reduction, due to the higher strength in testing of V3C greater savings are assumed due to further down gauging. This study has looked at developing a new hybrid forming process which has led to a significant reduction in forming time from 20 minutes or longer per part in AA5083 to around 5 minutes per part in AA7020, the same forming cycle would be suitable for V3C as for AA7020 leading to a 50% cost saving at this stage. All secondary materials and process costs associated with the forming process are considered to be identical to current costs. Manual handling of parts, lubrication, part cleaning and final trimming are common to the new material and process as well as existing processes at Superform.

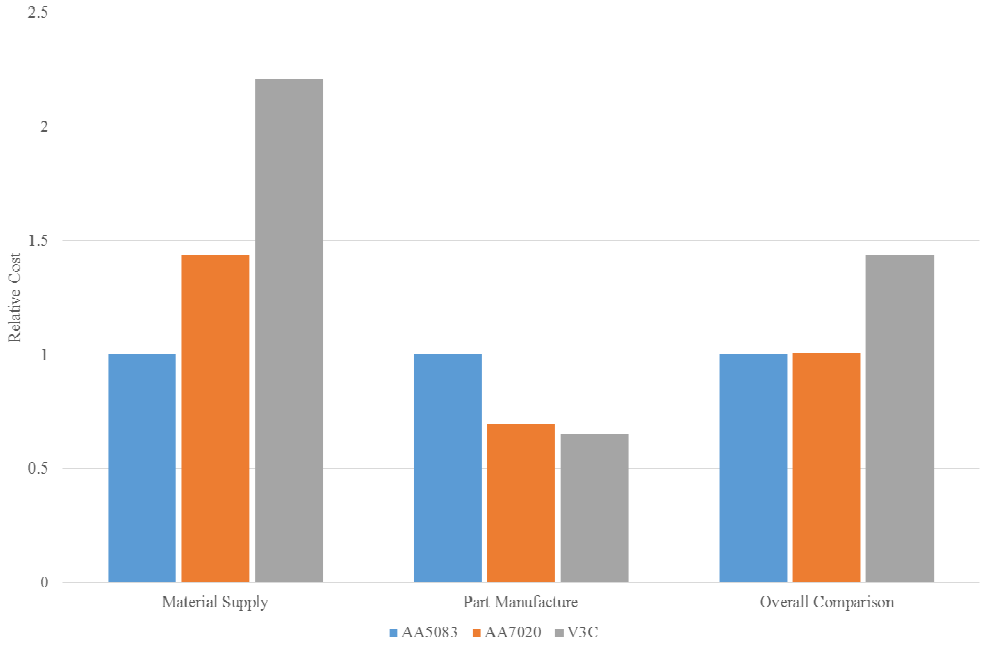


Fig.70. Relative costs of parts formed in AA5083 AA7020 and V3C materials.

Both AA7020 and V3C require secondary heat treatment after forming to achieve the higher strength T5 condition which allows for down gauging compared to AA508 which is produced in O temper and as such has no further heat treatment after forming. Overall parts made from AA7020 are more costly than those made from AA5083 due to the higher cost of the original alloy, savings are made in the production of parts due to the reduced cycle times of the process developed within this study as illustrated in fig.70.

Further savings could be made in the post forming heat treatment of the AA7020 by supplying parts to customers in an under-aged condition and using the customer paint bake cycle to achieve the final high strength condition as investigated in section 3.5.1 of this study. These savings would bring the cost of parts formed in AA7020 even closer to that of AA5083, due to the alternative applications of the two alloys there was not a need to achieve cost parity between the alloys as part of this study.

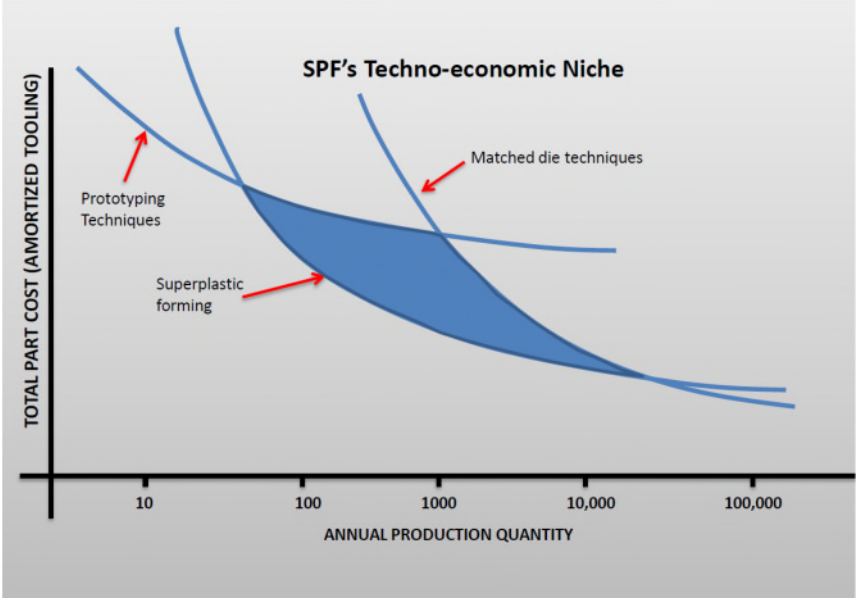


Fig.71. Part cost vs annual production quantity showing techno-economic niche of SPF [86].

Due to the reduction in cycle times and the use of low cost non matched dies which are more typical of an SPF forming process the newly developed process would look to be competitive with QPF producing similar part volumes (tens of 1000s per annum) [85]. Standard SPFs techno-economic niche where it is most competitive is illustrated in fig.71, the developed process within this study would be competitive at greater quantities than SPF but less than those of matched die techniques. The combination of AA7020 and developed process achieve this increased competitiveness by producing more complex parts than matched die techniques and stronger (300 MPa vs 150 MPa) parts at higher volumes than SPF forming using AA5083.

# 5. Conclusions

## *5.1. Industrial Impact of the Research*

The aim of the project was to deliver a material with acceptable levels of formability which could be formed within a five minute cycle and with a final yield strength of a minimum 300 MPa. This was achieved by using AA7020 in a modified SPF forming process with some mechanical preforming, higher strain rates. The alloy was seen to achieve equivalent strains in excess of 200% in a free formed bulge test, and in excess of 400% in closed tool tests providing the alloy has seen 100% strain before contact with the tool.

The project also delivered a second alloy V3CN based on the AA7020 with a 1.6wt% nickel addition, this alloy offered less formability than the AA7020 however with a higher yield strength of 342 MPa. The alloy proved less formable in free formed bulge and closed tool tests with a maximum limit of 100% equivalent strain, but with no minimum requirement for strain. This makes the alloy a suitable alternative for higher strength less complex applications where the AA7020 would be unsuitable due to low levels of strain present.

The project established a two stage aging treatment of 90°C for 8 hours and 130°C for 18 hours which achieved peak strength for both alloys and was deemed to be acceptable for use industrially. The project also demonstrated the need for targeted lubrication when forming around male radii's to stop any "slip" of material which would lead to localised necking and premature failure of parts.

The development of this alloy showed the promise of nickel additions to significantly improve both formability and post forming properties of AA7020, shown by the first

batch of V3C. It also showed the issues faced in increasing production of this alloy to a larger scale, slower solidification rates in larger batches of the alloy lead to greater amounts of coarser $Al_3Ni$ particles which negatively impact formability. Optimization of solidification rates allowing for a better distribution of finer particles would lead to an alloy with greater formability and strength that AA7020.

The AA7020 alloy within a hybrid SPF process has been proven to be formable in industrial applications. Several different part geometries of high end niche automotive vehicles have been formed as demonstrator pieces in cycle times equal to or lesser than AA5083 two examples of this are show in fig.72 a and b. The material and process have also achieved commercial success, the material having passed through the prototyping and testing phases and parts scheduled to go into production in January 2017 for use within door crash structures of a high end niche vehicle manufacturer.

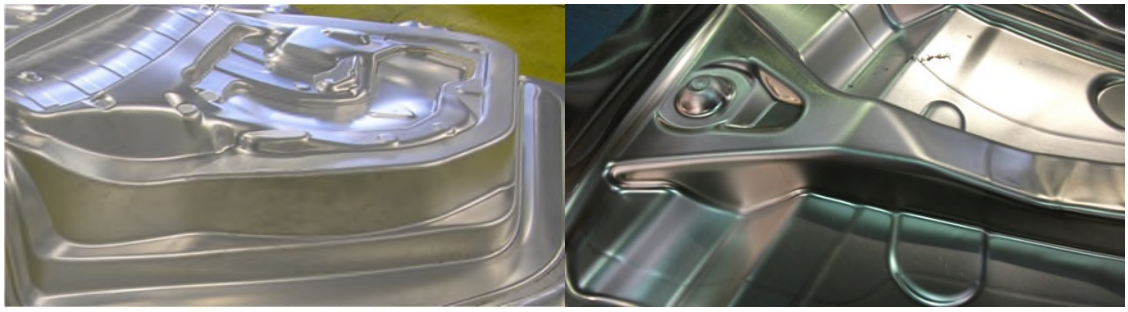

Fig.72. a) Boot panel formed in AA7020, b) B pillar formed in AA7020.

### *5.2. Academic Achievements*

The work from this project has been disseminated by means of oral presentation at the EUROSPF 2014 conference in Liechtenstein, and also the EUROSPF 2016 conference in Toulouse. A poster presentation of magnesium formability was also presented at the

ICSAM 2015 conference in Tokyo, this was a side project comparing the formability of magnesium alloys in an SPF process using gas bulge test tooling on the Interlaken press.

At the time of publication, one paper has been published, “In-Situ Heated Stage SEM Analysis & Characterisation of Recrystallization Behaviour of a 7000 Series Alloy with Nickel Additions” in Material Science and Engineering Technology. The paper focussed on work conducted on the new heated EBSD stage at WMG and was cleared for publication by Superform on the basis that only the nickel containing alloys were included. A second paper “Comparison of Superplastic Forming Abilities of As-cast AZ91 Mg Alloy Prepared by Twin Roll Casting and WE43 Alloy” has been accepted for publication in early 2018 in Materialwissenchaft und Werkstofftechnik.

## 6. Future Work Arising From the Research

This section highlights the limitations of the research undertaken during this project and suggests further work arising from the research. Academically to improve the understanding of the materials formability, strength development and underlying mechanisms and microstructural changes responsible. Industrially a “road map” is presented to offer a route towards industrialisation of nickel containing alloys.

### *6.1. Recrystallization Mechanisms and Microstructural Evolution*

A working hypothesis for the formability exhibited by the AA7020 alloy is that of dynamic recrystallization during forming compared to greater levels of static recrystallization due to increased PSN in V3C and V3CN. The current work investigated this hypothesis by means of fast quenching of alloys after deformation in an attempt to “freeze” the microstructure at this point and observe any microstructural evolution.

Samples were quenched as fast as possible with the current experimental set up, taking around five seconds to go from the testing temperature of 500°C to room temperature. Testing conducted on the SEM using an in situ heated stage showed that exposure to temperatures of this magnitude for very short times ~2 seconds caused the material to recrystallize. This could have caused further recrystallization which has obscured the evolution occurring purely during the forming cycle.

To fully test the hypothesis, and to accurately establish the mechanisms responsible for recrystallization and deformation as well as the difference between the AA7020 and nickel containing variants a differed method is required. In situ heated tensile stage testing within the SEM which would allow for the microstructural evolution within the material to be observed in real time, would be the best method for this. This technique

would allow any grain refinement with applied strain to be observed as well as identify any differences in the microstructural evolution of the various alloys. This was intended to be part of this research project but the in-situ heated tensile stage was not available before completion.

Investigations into materials recovery and recrystallization were conducted by means of in situ heated staged EBSD and FSD to observe microstructural changes as the occurred in real time rather than ex post facto. This overcomes issues with “freezing” the microstructure at certain points during heating and forming; the quench could not be rapid enough to halt microstructural stages, and there is the possibility of missing the event you desire to observe.

The limitations of this method are that observations are conducted purely on the surface of the material, this can add to greater relief due to higher amounts of high angle grain boundaries and less grains/sub grains for pinning. These factors lead to a slightly finer structure than would be expected within the bulk material, bulk samples were used for comparison but as mentioned previously these are ex post facto samples and the microstructure may have changed during quenching.

To fully evaluate the surface effects, new dual beam SEM and FIB equipped SEM arriving at WMG would be used which allow for the material to be milled away in situ and allow for observations of the bulk material to be made simultaneously with the surface. TEM analysis of fine NiAl particles which are below the detection limit of the SEM, should be conducted to fully understand the role of nano-scale sized particles within the alloy.

### *6.2. Road Map of Industrialisation of Nickel Containing Alloys*

This work demonstrated the ability of nickel additions to AA7020 to improve both material formability and post forming properties. The work also highlighted issues in scaling up this process from a laboratory to a larger scale, to achieve fine $Al_3Ni$ particles within the alloy a fast solidification rate is required which is more difficult to achieve with larger scale casting.

To produce a commercial alloy firstly the solidification rate of the cast alloy would need to be established and carefully controlled to achieve the desired size of particles. Possible casting by twin roll, continuous or belt casting should be investigated to establish if these processing routes are suitable. Following casting, the effects of homogenisation treatment and subsequent rolling regime would be investigated to quantify what influence, if any, these processing stages have on the particle size and distribution. This would require significant industrial cooperation and investment as it would call for large scale casting as well as further processing and rolling to suitable gauge sheet.

Following the production of material on a larger scale, formability and post forming properties should be tested by established methodologies. The tooling designed for the Interlaken press being modular would be used to test the materials suitability within an industrial process before full scale testing in factory, which could be driven purely for research or for a customer requirement. The tooling would also be used to help improve accuracy of simulations at Superform which are already carried out using data collected during this study, helping to validate levels of thinning in different areas of formed parts. The effect of lubrication on forming would also be further investigated using the tooling to look at the limits of forming over sharp radii.

Finally with an established forming regime for the material  drop tower and VHS strain rate testing should be employed to establish the materials crash worthiness, the tooling for the Interlaken press was designed with this testing in mind, as such the sample geometry after forming allows for three VHS testing coupons to be machined. Corrosion resistance of the material would be evaluated using an environmental chamber to mimic the service conditions the material will experience, the influence of joining method (SPR, adhesives, spot welding) on corrosion properties should also be investigated for their influence on the crashworthiness and corrosion resistance of the material.

## 7. References

[1] MacKenzie, D., Zoepf, S., Heywood, J., Determinants of US passenger car weight, International Journal of Vehicle Design, 2014; 65: 73-93.

[2] Brooke L., Evans H., Lighten Up!, Automotive Engineering International, March 2009; 16-13.

[3] Schultz R.A., Abraham K., Metallic Material Trends for North American Light Vehicles, Ducker Worldwide, 2009.

[4] Alson, J., Hula, A., Bunker, A., Light Duty Automotive Technology and Fuel Economy Trends: 1975 through 2008, U.S. Environmental Protection Agency, 2009.

[5] Bandivadekar, A., Bodek, K., Cheah, L., Evans, C., Groode, T., Heywood, J., Kasseris, E., Kromer, M., Weiss, M., On the Road in 2035: Reducing Transportation's Petroleum Consumption and GHG Emissions Laboratory for Energy and the Environment, Report No. LFEE 2008-05 RP, Massachusetts Institute of Technology, July, 2008.

[6] Zoepf, S.M., Automotive Features: Mass Impact and Deployment Characterization, Massachusetts Institute of Technology, Master's Thesis, 2011.

[7] Yi, J., Wooldridge, S., et al. Development and Optimization of the Ford 3.5L V6 EcoBoost Combustion System, SAE International Journal of Engines, 2009; 2: 1388-1407.

[8] Zhou, Z., Wang, M., Hao, H., Johnson, L., Wang, H., Plug-in Electric Vehicle Market Penetration and Incentives: a Global Review, Mitigation and Adaptation Strategies for Global Change, 2015; 20: 777-795.

[9] Steinparzer, F., Brüner, T., Schwarz, C., Rülicke, M.,The New BMW Three- and Four-Cylinder Gasoline Engines, MTZ Worldwide Development Gasoline Engines, 2014; 75: 14-21.

[10] Walliser, F.S., 918 Spyder Concept of a Super Sports Car for the Future, Automobil und Motorentechnik, Internationales Stuttgarter Symposium,2010: 14; 833-845.

[11] Lipscy, P. Y., Schipper, L., Energy Efficiency in the Japanese Transport Sector, Energy Policy, 2013; 56: 248-258.

[12] An, F., Gordon, D., He, H., Kodjak, D., Rutherford, D., Passenger Vehicle Greenhouse Gas and Fuel Economy Standards: A Global Update, ICCT, 2007.

[13] Kodjak, D., Policies to Reduce Fuel Consumption, Air Pollution, and Carbon Emissions from Vehicles in G20 Nations, ICCT, 2015.

[14] Austin, D., Dinan, T., Clearing the Air: The Costs and Consequences of Higher CAFE Standards and Increased Gasoline Taxes, Journal of Environmental Economics and Management, 2005; 50: 562-582.

[15] An. F., Sauer, A., Comparison of Passenger Vehicle Fuel Economy and Grenhouse Gas Emission Standards Around the World, Pew Centre on Global Climate Change, 2004.

[16] Ashby, M.F., Materials Selection in Mechanical Design, Oxford, Butterworth-Heinemann, 2005, pp.45-78.

[17] Hurless, B.E., Froes, F.H., Lowering the Cost of Titanium, AMPTIAC Newsletter, 2002; 6: 3-23.

[18] Hoeschl, M., Wagener, W., and Wolf, J., BMW's Magnesium-Aluminium Composite Crankcase: State of the Art Metal Casting and Manufacturing, SAE International, SAE Technical Paper, 2006.

[19] Suk, G.H., The Korea Herald English Edition, POSCO to supply metal for Porsche 911, http://www.koreaherald.com/view.php?ud=20150311001019. Published online 2015.

[20] Keeler. S., Kimchi, M., Advanced High-Strength Steels Application Guidelines, World Auto Steel Publication, 2014.

[21] Copeland, D., Pfestorf, M., The BIW of the New BMW 5 Series Gran Turismo, BMW, 2010.

[22] http://www.thesupercars.org/ferrari/ferrari-enzo/ Accessed on 25.04.16.

[23] Jacob, A., BMW Counts on carbon Fibre for its Megacity Vehicle, Reinforced Plastics, 2010; 54: 38-41.

[24] Jacob, A .,Boeing and BMW Group Team up on Carbon Fibre Recycling, Reinforced Plastics, 2013; 57: 39-42.

[25] Aluminium in Cars Unlocking the Light-Weighting Potential, European Aluminium Association, 2010.

[26] Hirsch, J., Automotive Trends in Aluminium – The European Perspective, Materials Forum, 2004; 28: 15-25.

[27] Kim, N.J., Designing With Aluminium Alloys, in Totten, G.E., Handbook of Mechanical Design, New York, 2004, pp 3-27.

[28] Srivatsan, T.S., The Science, Technology, and Applications of Aluminum and Aluminum Alloys, in Soboyejo, W., and Srivatsan, T.S., Advanced Structural Materials, CRC Press, 2006, pp4-23.

[29] Polmear, I., Light Alloys, Fourth Edition: From Traditional Alloys to Nanocrystals, Butterworth-Heinemann, 2005, pp 97-204.

[30] Ridley, N., Metals for superplastic forming, *Giuliano*, G., Superplastic Forming of Advanced Metallic Materials, Woodhead, 2011, pp3-33.

[31] Wadsworth, J., Ruano, O.A., Sherby, O.D., Deformation by Grain Boundary Sliding and Slip Creep Versus Diffusional Creep, TMS Annual Meeting, 1999, pp 425-439.

[32] Bernhart, G., Processing and Equipment for Superplastic Forming of Metals, in Giuliano, G., Superplastic Forming of Advanced Metallic Materials, Woodhead, 2011, pp 49-71

[33] Ashby, M.F., Verrall, R.A., Diffusion Accommodated Flow and Superplasticity, Acta Metallurgica, 1973, 21, 149-163.

[34] Backofen, W.A., Turner, I.R., and Avery, D.H., Trans. American Society Metals, Vol.57 (1964) pp.980–985.

[35] Langdon, T.G., Seventy-five years of superplasticity: Historic developments and new opportunities, Journal of Material Science, 2009; 44: 5998-6010.

[36] Nieh, T.G., Wadsworth, J., Sherby, O.D., Superplasticity in Metals and Ceramics, Cambridge, 1997, pp 5-22.

[37] Avtakratova, E., Mukhametdinova, O., Sitdikov, O., Markushev, M., High Strain Rate Superplasticity of Commercial 1570c Aluminium Alloy after ECAP and Rolling, Conference presentation, EuroSPF conference, Liechtenstein, 2014.

[38] Kawasaki, M., Figueiredo, R.B., Langdon,T.G., The Requirements for Superplasticity with an Emphasis on Magnesium Alloys, Advanced Engineering Materials, 2015; 1: 127-131.

[39] Gottstein, G., Shvindlerman, L.S., Grain Boundary Migration in Metals, CRC Press, 2009.

[40] Siegert, K., Werle, T., Process Technologies, TALAT Lecture 3803, European Aluminium Association, 1994.

[41] Mulyukov, R.R., Nazarov, A.A., Imayev, R.M., Current Status of Research and Development on Superplasticity at the Institute for Metals Superplasticity Problems, Material Science Forum, 2013; 735: 403-408.

[42] Boissiere, R., Terzi, S., Blandin, J.J., Quick- Plastic Forming: Similarities and Differences with Super-Plastic Forming, EuroSPF Conference Paper, France, 2008.

[43] Ridley, N., Superplastic Forming, in Totten, G.E., and Mackenzie, D.S., Handbook of Aluminium Vol. 1: Physical Metallurgy and Processes, CRC Press, 2003.

[44] Grimes, R., Superplastic forming of aluminium alloys, in Giuliano, G., Superplastic Forming of Advanced Metallic Materials, Woodhead, 2011, pp.247-271.

[45] Watts, M., Stowell, M.J., Baikie, B.L., Owen, D.G.E., Superplasticity in Al–Cu–Zr Alloys. Part 1: Material Preparation and Properties B., Metal Science Journal ,1976; 10: 189-197.

[46] Doherty, R.H., Hughes, D.A., Humphreys, F.J., Current Issues in Recrystallization: a Review, Materials Science and Engineering: A, 1997; 238: 219-274.

[47] Humphreys, F.J., Hatherley, M., Recrystallization and Related Annealing Phenomena, Oxford, 2004.

[48] http://aluminium.matter.org.uk/content/html/eng/default.asp?catid=68&pageid=803396170, Accessed 06.04.14.

[49] Kaibyshev, R., Goloborodko, A., Musin, F., Nikulin, I., Sakai, T., The Role of Grain Boundary Sliding in Microstructural Evolution during Superplastic Deformation of a 7055 Aluminium Alloy, Materials Transactions, 2002; 44: 2408-2414.

[50] Humphreys, F.J., The Nucleation of Recrystallisation at Second Phase Particles in *Aluminum*, Acta Metallurgica, 1977; 25: 1323-1344.

[51] Mikhaylovskaya, A.V., Portnoy, V.K., Superplasticity of the aluminium alloys containing the Al3Ni eutectic particles, Materialwissenschaft und Werkstofftechnik, 2012; 43: 772-775.

[52] Kotov, A.D., Mikhailovskaya, A.V., Superplasticity of Alloy Al – 11% Zn – 3% Mg – 0.8% Cu – 0.3% Zr with Fe and Ni Additives, Metal Science and Heat Treatment, 2013; 55: 22-25.

[53] Mikhaylovskaya, A.V., Kotov, A.D., Pozdniakov, A.V., Portnoy, V.K., A high-strength aluminium-based alloy with advanced superplasticity, Journal of Alloys and Compounds, 2014; 599: 139-144.

[54] Mosleh, A.O., Mahmoud, F.H., Mahmoud, T.S., Khalifa, T.A., Microstructure and Static Immersion Corrosion Behaviour of AA7020-O Al Plates Joined by Friction Stir Welding, Material Design and Applications, 2015; 1-11.

[55] Lee, S., Utsunomiya, A., Akamatsu, H., Neishi, K., Furukawa, M., Horita, Z., Langdon, T.G., Influence of Scandium and Zirconium on Grain Stability and Superplastic Ductilities in Ultrafine-grained Al–Mg alloys, Acta Materiala, 2002; 50: 553-564.

[56] Musin, F., Kaibyshev, R., Motohashi, Y., Sakuma, T., Itoh, G., High Strain Rate Superplasticity in an Al–Li–Mg Alloy Subjected to Equal-Channel Angular Extrusion, Materials Transactions, 2002; 43: 2370-2377.

[57] http://mineralprices.com/default.aspx#rar. Accessed 31.07.2016.

[58] Krajewski, P.E., Schroth, J.G., Overview of Quick Plastic Forming Technology, Materials Science Forum, 2007; 551: 3-12.

[59] Krajewski, P.E., Quick Plastic Forming of Aluminium Alloys, in *Giuliano*, G., Superplastic Forming of Advanced Metallic Materials, Woodhead, 2011, pp.272-302.

[60] Liu, J., Superplastic-like Forming of Lightweight Alloys, PhD. Thesis Nanyang Technological University, 2012.

[61] Luo, Y., Luckey, S.G., Copple, W.B., Friedman, P.A., Comparison of Advanced SPF Die Technologies in the Forming of a Production Panel, Journal of Materials Engineering and Performance, 2007; 17: 142-152.

[62] Luo, Y., Luckey, S.G., Friedman, P.A., Peng, Y., Development of an Advanced Superplastic Forming Process Utilizing a Mechanical Pre-forming Operation, Journal of Machine Tools & Manufacture, 2008; 48: 1509-1518.

[63] Liu, J., Tan, M., Aue-u-lan, Y., Catagne, S., Superplastic-like Forming of Non-superplastic AA5083 Combined with Mechanical Pre-forming, Journal of Advanced Manufacturing Technology, 2011; 52: 123-129.

[64] Ghosh, K.A., Hamilton, C.H., Influences of Material Parameters and Microstructure on Superplastic Forming, Metallurgical Transactions A, 1984; 13A: 733-743.

[65] Shojaeefard, M.H., Khalkhali, A., Miandoabchi, E., Effects of Process Parameters on Superplastic Forming of a License Plate Pocket Panel, Advanced Design and Manufacturing Technology, 2014; 7: 25-33.

[66] Hwang, Y.M., Yang, J.S., Chen, T.R., Huang, J.C., Analysis of Superplastic Sheet Metal Forming in a Circular Closed Die, JOM Processing Technology, 1997; 65: 215-227.

[67] Verma, R., Hector, L.G., Krajewski, P.E., Taleff, E.M., The Finite Element Simulation of High-temperature Magnesium AZ31 Sheet Forming, Journal of Materials, 2006; 61: 29-37.

[68] Krajewski, P.E., Lubrication System for Hot Forming, GM Motors, US Patent 5,819,572, 1998.

[69] Taleff, E.M., Hector, L.G., Bradley, J.R., Verma, R., Krajewski, P.E., Local Thinning at Die Entry Radius During Gas Pressure Forming of AA5083, JOM Science and Engineering, 2010; 132: 1-7.

[70] Hector, L., Taleff, E.M., Krajewski, P.E., Carter, J., High-Temperature Forming of a Vehicle Closure Component in Fine-Grained Aluminum Alloy AA5083: Finite Element Simulations and Experiments, Key Engineering Materials, 2010; 433: 197-209.

[71] Krajewski, P.E., Morales, A.T., Tribological Issues During Quick Plastic Forming, JOM Engineering and Performance, 2004; 13: 700-709.

[72] Eivani, A.R., Zhou, J., Duszczyk, J., Grain Boundary Versus Particle Stimulated Nucleation in Hot Deformed Al-4.5Zn-1Mg Alloy, Materials Science and Technology, 2013; 29: 517-528.

[73] Jupp, S., Personal communication, Hydro Aluminium, Nov 2013.

[74] BS EN ISO 6892-1:2009 Metallic materials. Tensile testing. Method of test at ambient temperature. Test standard, 2009.

[75] https://www.gimp.org/

[76] https://imagej.nih.gov/ij/

[77] Lech-Grega, M., Ckiewicz, S.H., Richert, M., Szymanski, W., Structural Parameters of 7020 Alloy After Heat Treatment, Materials Characterization, 2001; 46: 251 – 257.

[78] https://www.oxford-instruments.com/products/microanalysis/ebsd

[79] Mondolfo, L.F., Aluminum Alloys: Structure and Properties, Oxford, Butterworth-Heinemann, 1976, pp.338-578.

[80] Eivani, A.R., Ahmed, H., Zhou, J., Duszczyk, Evolution of Grain Boundary Phases during the Homogenization of AA7020 Aluminum Alloy, Metallurgical and Materials Transactions A, 2009; 40: 717-728.

[81] Kotov, A.D., Mikhaylovskaya, A.V., Kishchik, M.S., Tsarkov, A.A., Aksenov, S.A., Portnoy, V.K., Superplasticity of High-Strength Al-Based Alloys Produced by Thermomechanical Treatment, Journal of Alloys and Compounds, 2015; 688: 336-344.

[82] Yun, M., Lokyer S., Hunt, J.D., Twin Roll Casting of Aluminium Alloys, Materials Science and Engineering: A, 2000; 280: 116-123.

[83] Driver, H.J., Design of Aluminum Rolling Processes for Foil, Sheet, and Plate, *Xie, L.*, Handbook of Metallurgical Process Design, CRC Press, 2004, pp69-114.

[84] Kumar, S., Namboodhiri, T.K.G., Precipitation Hardening and Hydrogen Embrittlement of Aluminum Alloy AA7020, Bulletin of Material Science, 20ll; 34: 311-321.

[85] Jupp, S., Personal communication, Superform, June 2017.

[86] Edwards, D., Presentation, Achieving Complex Geometry with High Strength Aluminium Alloys, Global Automotive Lightweight Materials, 2016.